2016 年度

博士学位論文

中部大学

CHUBU UNIVERSITY
AICHI
JAPAN

GROWTH AND CHARACTERIZATION OF ZINC-BASED NITRIDE THIN FILMS AS VERSATILE SEMICONDUCTORS
多目的半導体としての亜鉛系窒化物薄膜の成長と評価

XIANG CAO

DEPARTMENT OF APPLIED CHEMISTRY
CHUBU UNIVERSITY
JAPAN MARCH 2017

CHUBU UNIVERSITY

A Dissertation entitled

GROWTH AND CHARACTERIZATION OF ZINC-BASED NITRIDE THIN FILMS AS VERSATILE SEMICONDUCTORS

by

Xiang CAO

Under the supervision of

Prof. Yoshihiko NINOMIYA & Prof. Naoomi YAMADA

Submitted to the College of Engineering, Chubu University,
in Partial Fulfillment of the Requirements for
the Degree of Doctor of Philosophy in Chemistry

Chubu University

1200 Matsumoto-cho, Kasugai, Aichi 487-8501, JAPAN

AICHI JAPAN March 2017

Preface

Zinc is a heavy post-transition metal with an electron configuration of $[Ar]3d^{10}4s^2$ and ranks top twenty as one of the most abundant metal elements in Earth's crust; tin is anther "Earth-abundant" metal element, both having economic-efficiency interests.

In materials science, transparent conducting oxides (TCOs) have achieved and will achieve more remarkable researches regarding theories and applications.

Nitrides, a novel class of semiconductors, appeal to us. To widen diversity of materials, we investigated the nitrides, hoping attractive findings and excellent performance.

Covering fabrication process, exploration and investigation on structural, electrical and optical properties of zinc-based nitrides, this dissertation provides more details and perspectives on understanding zinc nitride (Zn_3N_2) and zinc tin nitride ($ZnSnN_2$) materials.

Not only Zn_3N_2 but $ZnSnN_2$, some issues like bandgap are somewhat hotly debated among different groups. This work presents one speculation over this main issue.

Impurities like oxygen can not be absolutely eliminated form the film-growth chamber when reactive radio-frequency (RF) magnetron sputtering technique was employed.

To study the effect of oxygen impurity on the properties of Zn_3N_2 material, intentional oxygen doping was performed to prepare the polycrystalline (poly.) Zn_3N_2 thin films.

Reports on the electron transport of Zn_3N_2 haven't surfaced since its powder was first synthesized in 1940. Detailed discussions on electron transport mechanisms were carried out, illustrating one reason for high mobilities obtained even in poly. Zn_3N_2 films.

In terms of the effective masses of Zn_3N_2 and $ZnSnN_2$ materials, scarce literature exists. This dissertation focuses on estimation of the effective mass concern.

Discoveries made for zinc-based nitrides in this work, we hope, can stimulate more dramatic researches on nitrides to promote the developments of materials science.

Effort to prevent unintentional oxygen doping into films has been devoted, qua oxygen impurity concentrations, this work needs more efficient approaches to be exploited.

Such significant and meaningful findings achieved in this dissertation contribute towards making zinc-based nitride semiconductors promising versatile materials for electronic, optoelectronic, photovoltaic solar cell and sensor applications.

Abstract

Transparent conducting nitrides (TCNs, *e.g.*, InN, AlN, GaN, and their alloys) have been proven to be, beyond the possibility of doubt, revolutionary breakthroughs in materials science. With the ever-advancing information and energy technologies and the mounting demands for materials applications, novel materials possessing unique properties need to be progressively exploited. As a member of the so-called "earth-abundant" metal elements, zinc (Zn), can originate directly from reclamation sources. Consequently, the dissertation presented here, is motivated by the need of exploring attractive zinc-based nitride transparent conductors and thus expanding the diversities of materials, not only from the viewpoint of economic efficiency but from an environment-friendly perspective.

Proposed here are the investigations of zinc-based binary/ternary nitride thin films: zinc nitride (Zn_3N_2) and zinc tin nitride ($ZnSnN_2$). Reactive radio-frequency magnetron sputtering technique was employed to grow films on non-alkali glass and yttria-stabilized zirconia ($Y_{0.13}Zr_{0.87}O_2$; YSZ) substrates under optimized deposition conditions. The thorough characterizations of representative films were conducted from viewpoints of structural, electrical and optical properties.

The densely and uniformly packed grains consist of phase-pure anti-bixbyite structural Zn_3N_2 films with relatively smooth surfaces. A certain amount of oxygen detected in each as-deposited film contributed to the degenerate *n*-type doping. Tuning *x* values can affect modification of electrical and optical properties in $Zn_3N_{2-x}O_x$ films. A minimal resistivity of 6.2×10^{-4} Ω cm, together with a maximal Hall electron mobility of 85 $cm^2V^{-1}s^{-1}$ was achieved in an as-deposited O_2-doped polycrystalline $Zn_3N_{1.71}O_{0.29}$ film. The very spotlight, high mobility observed even in polycrystalline Zn_3N_2 films, makes them competitive with conventional transparent conducting oxides and group III-nitrides. In-depth discussions on electron transport mechanisms of Zn_3N_2 films dedicated to understanding the reasons for

observed high mobility are given. Notably, we firstly derived the electron effective mass at the bottom of the conduction band to be as small as $(0.08 \pm 0.03)m_0$ (m_0 denotes the free electron mass), which is comparable to those of InN and GaAs semiconductors. Such small electron effective mass can also result in high electron mobility of Zn_3N_2 material.

In this work for Zn_3N_2, low visible transmittances (usually below 60%) and accessible bandgaps ranging from 2.4 to 2.9 eV were obtained. From a defect-to-band transition standpoint, this work put forth a comprehensive explanation to such issues. Low visible transmittance was attributable to optical absorption by electron transitions between the interstitial half-filled N 2p in-gap states and the band states. Differential in-gap states densities led to different defect-to-band transition absorption and accordingly affected the somewhat hotly debated bandgaps. If reduction in such defect density was achieved, zinc nitride would be considered as a transparent semiconductor. Given the high mobility and potential optical transparency, Zn_3N_2 turns out to be attractive for applications in large-area polycrystalline semiconductor devices, such as thin-film transistors and solar cells.

Another significant achievement of this work is preparation and preliminary characteristics of $ZnSnN_2$. The structural analyses inferred $ZnSnN_2$ probably has a random-wurtzite type disordered structure. Being similar with the case of Zn_3N_2, oxygen defects in $ZnSnN_2$ films were responsible for unintentional degenerate *n*-type doping. Cu served as an effective electron killer compensating further *n*-type doping to a certain extent in $ZnSnN_2$ thin film. The estimated "scattered" bandgaps in the range 2.0–2.5 eV were due in part to high degenerate electron density and disorder degree in the cation sublattice. Electron effective mass of $ZnSnN_2$ material is derived to be $(0.37 \pm 0.05)m_0$ from double Tauc-Lorentz Drude model fitting. The discoveries made suggest that high-quality (nearly intrinsic, optimal-cation disorder) $ZnSnN_2$, comprised of earth-abundant elements, can be an alternative to InGaAlN materials system and has the potential to be applied to photovoltaics and solid-state lighting both from economic and environmental perspectives.

Keywords: zinc-based semiconductors, nitrides materials, TCNs, Earth-abundant elements, reactive radio-frequency magnetron sputtering technology, zinc nitride (Zn_3N_2), zinc tin nitride ($ZnSnN_2$), high electron mobility, low resistivity, electron effective mass, oxygen-doping, electron transport mechanisms, bandgap evaluation, potential transparent semiconductors, versatile applications.

To my beloved fiancée, elder sister, and parents on both sides,

None of this would be possible without company of you all.

I once heard the echo, from mother's heart and mine
It's a mirable tune pulses with life rhythm
Even though a drop in the ocean
I was born with life pursuits
Gratitude, Grace, Freedom, Faith, Love, Happiness

I once heard the echo, from truelove's heart and mine
It's a dulcet melody rings from spring to winter
Since the one destines to be like a blue moon in the sky
What I have been learning is to be of great
Struggle, Mutual Respect, Tolerance, Love, Responsibility

I once heard the echo, from material's heart and mine
It's a marvelous song composed by mysteries
Like a nightingale vocal solo to birds singing
zinc-based nitrides to materials research
Sing along with the musical notes of
Interest, Aspiration, Thinking, Exploration, Love, Action

— Xiang CAO
(@ Chubu University)

Acknowledgements

A work such as this would not have been possible without considerable help form near and far. First and foremost, please allow me to extend my heartful gratitude to ***Prof. Yoshihiko Ninomiya***, ***Prof. Naoomi Yamada*** in Chubu University and ***Prof. Hanxu Li*** in Anhui University of Science and Technology. Here, I would like to take this opportunity to thank ***Prof. Yoshihiko Ninomiya*** and ***Prof. Hanxu Li*** to offer me a chance to perform this work in Chubu University and introduce me to ***Prof. Naoomi Yamada*** who has been my direct supervisor. The greatest power source originates from my academical and spiritual mentor, ***Prof. Naoomi Yamada***, who provided me such a challenging and exciting research theme, tries his best to guide me the road approaching solid state chemistry field with his wisdom, diligent teaching, and encouragement, for which I am deeply grateful in mind. Besides, he also helps and cares for my living in Japan, and teaches me to strengthen self-ability via learning wider and deeper to make dreams fulfilled, which is my life-long spirit wealth.

High tribute should be paid to ***Prof. Yuzo Shigesato*** from College of Science and Engineering in Aoyama Gakuin University, ***Prof. Kenichi Imaeda*** and ***Prof. Makoto Sakurai***, from my mother university: Chubu University, ***Prof. Taro Hitosugi*** from School of Materials and Chemical Technology in Tokyo Institute of Technology, ***Dr. Fumio Kawamura*** from National Institute for Materials Science (NIMS), and ***Shoichiro Nakao*** from Kanagawa Academy of Science and Technology (KAST), for their good professional suggestions and advice regarding my research plans, methods and contents.

Experimental apparatus operation is absolutely necessary for the sample characterizations. I am greatly indebted to the staff from the Analysis Center in Chubu University, ***Masunori Kawamura*** for his patient directions in XRD and XPS techniques; laboratory students: ***Takahiro Yamaguchi***, ***Kohei Maruya***, ***Yuuki Yamaguchi*** for sputtering device usage instructions, ***Kouki Watarai***, ***Ryuichiro Ino***, ***Ryota Seko***, ***Mitsuru Kasuga***, ***Mizuki Kato***,

Hiroyuki Shirai for relevant characterizations; special appreciations to my fellow students ***Koji Umezome*** and ***Yui Sugiyama*** for their explorations of related research topics. And of course, my appreciations are also extended to the other students and friends in and out of Prof. Yamada's laboratory who gave me a wonderful experience of studying in Japan and/or built lasting friendships by virtue of their kindness and enthusiasm.

As my research carriers, the Ministry of Education, Culture, Sports, Science and Technology of Japan (***MEXT***) offers me a chance to start my research, the ***Chubu University***, embraces me and allows me to have my research been accomplished throughout the very fascinated and meaningful journey. I would like to acknowledge the financial supports from the Chubu University Grants A (No. 26IS15A), D (No. 26IIS01DII) and D (No. 28IS02D), as well as the ***NAGAI Foundation for Science & Technology*** and ***Marubun Research Promotion Foundation*** for research communications.

At last but not least, the sacrifice and support from ***my whole family*** earn my sincere gratefulness from the bottom of my heart. I utterly realize and understand that without their never-wavering comprehension and encouragement, I would not go this far. Oh, darling, my deer fiancée, ***Xu Meng***, only I can say to you is Thank you & Love you. It is your inner love and support surrounding that I have been growing up to be a better and more mature me. Please accept my earnest supplication and keep it in mind that YOU, I LOVE.

Xiang CAO

Kasugai, Japan

November 2016

Contents

List of Figures

List of Tables

List of Abbreviations

2, 3D	Two, Three Dimensional
arb. units	arbitrary units
AFM	Atomic Force Microscopy
ALD	Atomic Layer Deposition
AlGaInN	Aluminum Gallium Indium Nitride
AlN	Aluminum Nitride
AMLCDs	Active-Matrix Liquid-Crystal Displays
Ar	Argon
BE	Binding Energy
BHD	Brooks-Herring-Dingle theory
ca.	circa (=about)
CaF_2	Calcium Fluoride
CB	Conduction Band
CdO	Cadmium Oxide
Cd_2SnO_4	Cadmium Stannate
$CuAlO_2$	Copper(I) Aluminate
$CuInGaSe_2$	Copper Indium Gallium Diselenide (CIGS)
cf.	confer
concn.	Concentration
CVD	Chemical Vapor Deposition
Cu_3N	Copper Nitride
$CuInSe_2$ (CIS)	Copper Indium Selenide
DC	Direct Current
DFT	Density Functional Theory
DOC	Density of States
Epi.	Epitaxial
e.g.	exempli gratia
et al.	et alia
etc.	et cetera
FCC	Face-Centered Cubic
FTIR	Fourier Transform Infrared
FTO	Fluorine-Doped Tin Oxide (SnO_2:F)
FWHM	Full Width at Half Maximum
f.u.	formular unit

GaAs	Gallium Arsenide
GaN	Gallium Nitride
GIXRD	Grazing Incidence X-Ray Diffraction
ICDD	the International Centre for Diffraction Data
IGZO	Indium Gallium Zinc Oxide
InN	Indium Nitride
ITO	Tin-Doped Indium Oxides (In_2O_3:Sn)
i.e.	id est
KE	Kinetic Energy
LCDs	Liquid-Crystal Displays
LEDs	Light-Emitting Diodes
LEEBI	Low-Energy Electron Beam Irradiation
MBE	Molecular Beam Epitaxy
MFC	Mass Flow Controller
MNs	Metal Nitrides
MOCVD	Metal Organic Chemical Vapor Deposition
N_2	Nitrogen
NH_3	Ammonia
O_2	Oxygen
OLEDs	Organic Light-Emitting Diodes
PAMBE	Plasma Assisted Molecular Beam Epitaxy
PL	Photoluminescence
PLD	Pulsed Laser Deposition
PLE	Photoluminescence Excitation
Poly.	Polycrystalline
PV	Photovoltaic
RBS	Rutherford Backscattering
Ref(s).	Reference(s)
ReO_3	Rhenium Trioxide
RF	Radio Frequency
RF-MBE	Radio Frequency Molecular Beam Epitaxy
RF-PAPLD	Radio Frequency Plasma Assisted Pulsed Laser Deposition
RSF	Root Mean Square
RSF	Relative Sensitivity Factor
RT	Room Temperature
Sc_2O_3	Scandium Oxide
SEM	Scanning Electron Microscopy
SnO_2	Tin Oxide
SSL	Solid-State Lighting
TCs	Transparent Conductors
TCOs	Transparent Conducting Oxides
TCMs	Transparent Conducting Materials
TCNs	Transparent Conducting Nitrides

TFTs	Thin Film Transistors
TiN	Titanium Nitride
UV-Vis	Ultraviolet-Visible
VB	Valance Band
XPS	X-Ray Photoelectron Spectroscopy
XRD	X-Ray Diffraction
XRR	X-Ray Reflectivity
YSZ	Yttria-Stabilized Zirconia
Zn_3N_2	Zinc Nitride
$ZnGeN_2$	Zinc Germanium Nitride
ZnO	Zinc Oxide
ZnON	Zinc Oxynitride
Zn_3P_2	Zinc Phosphide
ZnSe	Zinc Selenide
$ZnSiN_2$	Zinc Silicon Nitride
$ZnSnN_2$	Zinc Tin Nitride

Glossary of Symbols

a	a-axis length of crystal lattice (lattice parameter)
α	Absorption coefficient
A	Scattering cross section factor
A_D	Amplitude of Drude term
A_{TL}	Oscillator strength (amplitude) of Tauc−Lorentz term
Å	Angstrom
Al	Aluminum
Ar	Argon
cm	Centimeter
C	Nonparabolic parameter
C_γ	Broadening parameter of Tauc−Lorentz term
Γ_D	Broadening parameter of Drude term
℃	Celsius temperature
Cu	Copper
d	Thin film thickness
e	Elementary electric charge
eV	Electron voltage
E_0	Transition energy of the Lorentz component in the Tauc−Lorentz model
E_g^{opt}	Optical bandgap
f	Gas proportion (gas flow ratio)
$g(\zeta)$	Screening function
h	Planck constant
$\hbar$	Reduced Planck constant (= $h/2\pi$)
k	Wave vector of the electron
k_B	Boltzmann constant
K	Degree Kelvin
l_e	Mean free path
m_0	Free electron mass
m_d^*	Density of states effective mass
m_e^*	Electron effective mass
$m^*(n_e)$	n_e dependence of electron effective mass
min	Minute
n_e	Electron density
n_I	Density of ionized impurity scattering center
nm	Nanometer
N	Nitrogen

NH_3	Ammonia
N_N	Lattice nitrogen
N_I	Self-interstitial nitrogen
O	Oxygen
$O_N^{\bullet}$	Substitutional oxygen on nitrogen site
P	Gas Partial Pressure
Pa	Pascal
ρ	Resistivity
r	Scattering constant
R_H	Hall coefficient
s	Second
S	Seebeck coefficient
S/cm	Siemens per centimeter
T	Tesla
T	Temperature
T_s	Substrate temperature
v_F	Fermi velocity
V	Voltage
$V_N^{\bullet\bullet\bullet}$	Nitrogen vacancy
W	Watt
ω_P	Plasma frequency
Z	Charge on the impurity in units of e
Zn	Zinc
θ	Bragg angle
ε_0	Static dielectric constant of free space (permittivity of vacuum)
ε_r	Relative dielectric constant of material
$\varepsilon(\omega)$	Frequency-dependent dielectric function
ε_∞	High-frequency permittivity
μ_H	Hall mobility
μ_I	Mobility due to ionized impurity scattering
μ_N	Mobility due to neutral impurity scattering
μ_{opt}	Optical mobility (intra-grain mobility)
τ	Scattering time (relaxation time)
Ω	Ohm
χ	Electronegativity
Φ	Diameter
λ	Wavelength

人間には待機の時代と断行の時代とがあります。
潜伏の時代と飛躍の時代とがあります。
じっと好機の到来を待つ間も大事ですが、
ひとたび好機到来となれば機敏に
チャンスをつかまえる気力がなくてはなりません。

Ningenni wa taikinojidaito dannkounojidaito ga arimasu.
Sennpukunojidaito hiyakunojidaito ga arimasu.
Jitto koukinotourai wo matusma mo daiji desu ga,
Hitotabi koukitouraito nareba kibinn ni
Channsu wo tsukamaeru kiryoku ga nakute wa narimasen.

A human being has a life process of continuous development
With four periods of waiting, implementation, dormant, and leap.
Although it is of great significance of biding his time,
Once the opportunity goes by,
Promptness and competencies can not be absent to grasp it.

本多光太郎（物理学者）
Kotaro HONDA (Physicist)

Chapter 1

Introduction

Nothing in life is to be feared.

It is only to be understood.

—Mdm. Marie Curie

In materials science, when mentioned the conception "Transparent Conducting Materials (TCMs)", what will flash across one's mind?

Probably the notion of "Transparent Conducting Oxides (TCOs)" will ring a bell. Or even if we narrow down the scope of that puzzle to "Transparent Conducting Nitrides (TCNs)", presumably the idea of "Group III-Nitrides" will come to mind, "Gallium Nitride (GaN)" likely concretizes in his mind.

Admittedly speaking, as an important academic branch in materials science, TCOs, some TCNs and other TCMs are ubiquitous and have found far-reaching influences on human life, and certainly Nature, due in part to the fact that they have been penetrating into our normal life with widespread applications in information (computers products, smart facilities, storage devices, *etc.*) and energy (photoelectrochemical devices, energy-efficient windows, photovoltaic cells, *etc.*) technologies. Such technologies have been changing and creating our generations through their infinite power, just as the Nobel Prize in Physics 2014 went to Isamu Akasaki, Hiroshi Amano and Shuji Nakamura "for the invention of efficient blue light-emitting diodes which has enabled bright and energy-saving white light sources" [1].

1.1 Motivation

Particular and Intensive attention has been placing on the quick and steady improvement in TCMs field since the first TCO material, tin-doped indium oxide (In_2O_3:Sn, abbreviated ITO) was reported by Rupperecht [2] in 1954. Soon hereafter, other TCMs such as tin oxide (SnO_2), zinc oxide (ZnO), and GaN (single crystal thin film) thrived due in large measure to their unique electronic and optoelectronic properties. A renovation to the conception "TCMs" was fulfilled by the fact that a new frontier of TCOs was opened since the first *p*-type TCO, $CuAlO_2$, was discovered by Hosono group in 1997 [3]. This breakthrough has filled the gap of the absence of *p*-type "Transparent Oxide Semiconductors (TOSs)". Such a splendid discovery enables TCMs active electronic, optoelectronic and photovoltaics (PV) devices with *p*-*n* junctions.

Afterwards, apart from the prototypical elemental semiconductors (Si and Ge), more and more transparent semiconductors are being developed, under the circumstances where the discovery of novel semiconducting materials is a scientifically and technologically significant issue. Of the diverse transparent conducting materials, TCOs, III-V type semiconductors, and group III-N (in particular GaN with its related alloys) have garnered extensive interest. Noted recent years witnessed an unprecedented growth of interest in semiconducting nitrides due to the fact that they consisted of Earth-abundant elements, environmentally-friendly, and possess favorable unique properties for electronic, optoelectronic and photovoltaic applications. However, even the currently commercialized GaN and its based $Al_xGa_{1-x-y}In_yN$ alloys with tunable bandgaps have their own holdbacks: bio-toxic In; Earth-nonabundant constituents (In and Ga); and conspicuously volatile price/supply of In and Ga. Therefore, restudying the existing materials and exploiting new alternatives will be of great importance and necessity to rebuild the materials conception.

Melioration of current materials and discovery of novel materials can be breakthroughs in material-to-human history in the sense of the progressive evolution of human society. The

abovementioned situation simulates worldwide research group [4-7] to find, rediscover, or exploit novel nitrides, which also intrigues us. As technology develop and human demands are being increasingly required, devices with not only higher performance but elemental abundance/green materials, versatility of materials, long term stability, mass production, and lower cost are desperately in need for both fundamental and applied research.

In our work, our group have directed our attention to the burgeoning zinc-based nitride semiconductors, to be specific, zinc nitride (Zn_3N_2) and zinc tin nitride ($ZnSnN_2$) cases in which all the constituents are entire Earth-abundant elements, environmental benign, and economy-efficiency along with the fact that both are relatively "young" nitride-based semiconductors. There is no possibility of denying that quite a few research obstacles and challenges of which are awaiting to be surmounted.

1.2 Why Nitrides?

Nitride-based semiconductors are becoming progressively attractive since the everlasting advances in technologies and nitrides materials enjoy their own merits like environmentally benign nitrogen constituent and the rich composition space of nitrides. What's more, they are promising candidates for a wide variety of technological applications, such as high mobility thin film transistors (TFTs), solid-state lighting (SSL), bio and environmental sensors, saving devices, and especially in photovoltaics system.

Why nitride-based semiconductors exhibit striking character in optoelectronic applications? It is a facet that these nitrides usually show intermediate bonding behavior that results in their structure types so far exhibiting an intriguing mix of covalent (carbide-like), ionic (oxide-like) and unique motifs. From the chemical bonding property perspective, as depicted in Figure 1.1, compared to the more ionic oxides and the more covalent pnictides, nitrides tend to have intermediate energy of the valence band, due to the fact that nitrogen atom has a moderate electronegativity χ of 3.0 (whereas $\chi_O = 3.4$ and $\chi_{pnicogen} = 2.0–2.2$ [8]).

In this respect, the moderate electrical structure of nitrides can bear more crystallographic defects [9] compared to other pnictides, have better charge transport properties and make valence band position higher (enables less difficulty in doping *p*-type [10-11]) when compared to oxides. In the sense of expanding diversity from TCOs to TCNs, nitrides materials are interesting and desirable at present and also in the future work.

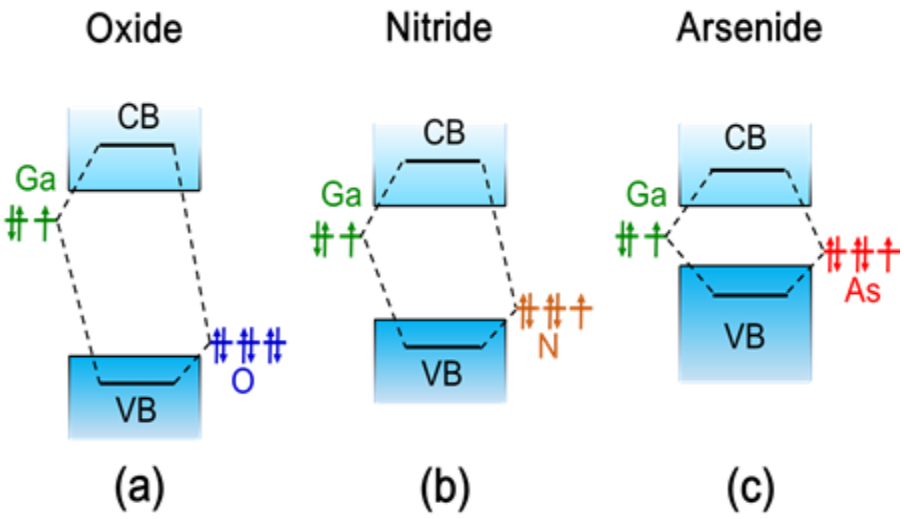

Figure 1.1. Schematic description of chemical bonding configurations in Ga-based semiconducting (a) oxides, (b) nitrides and (c) arsenides. (Adapted from A. Zakutayev, in Ref. [12])

1.2.1 Why Zinc Nitrides?

What's interesting, as a relatively "young" nitride materials, the history of zinc nitride, in fact, can be dated back to almost eighty years ago. In 1940, Juza and Hahn [13] were the first to successfully synthesize the black powder Zn_3N_2 with unrefined anti-bixbyite (anti-scandium oxide; anti-Sc_2O_3) structure.

Despite this early basic research on this material, Zn_3N_2 seemed to somewhat be at a standstill for almost half a century. Zn_3N_2 enjoyed great development only after the report of polycrystalline Zn_3N_2 film prepared through direct reaction between high-purity zinc

metal and ammonia (NH_3) by Kuriyama *et al.* in 1993 [14]. They also derived its optical bandgap energy lies in the neighborhood of 3.2 eV (see Figure 1.2(a)) and discussed the origin of this large bandgap of Zn_3N_2 material. At fifth year thereafter, an interesting character of that polycrystalline Zn_3N_2 films in N_2-rich atmosphere showing high electron mobility *ca.* 100 $cm^2V^{-1}s^{-1}$ at room temperature, was found by Futsuhara *et al.* [15] in 1998, as shown in Figure 1.2(b). These highlighting findings have intrigued a resurgence of research interest of this material as a transparent high-mobility semiconductor.

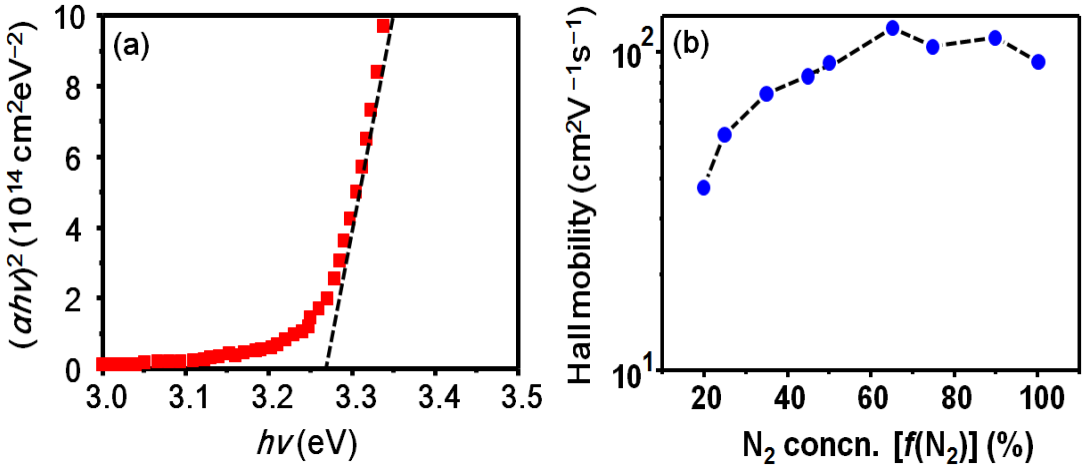

Figure 1.2. (a) $h\nu$ versus $(\alpha h\nu)^2$ plot for zinc nitride film from Kuriyama's team work. (b) Hall mobility as a function of N_2 concentration in sputtering gas for work of Futsuhara's group. The dashed lines are a guide for the eyes.

1.2.2 Why Zinc Tin Nitrides?

Another truly "young" nitride material, zinc tin nitride, has turned into be a hot topic worldwide within very recent years. Historically, the first synthesis report on $ZnSnN_2$ thin film prepared by Plasma-assisted Molecular Beam Epitaxy (PAMBE) technique [16] was surfaced in 2012. As an analogue to and a candidate substitute for the well-known AlGaInN (III-N) system, $ZnSiN_2$, which consists solely of Earth-abundant elements, is expected to exhibit properties similar, if not superior, to their counterpart III-N compounds. Like the close cousin family materials of ZnSe and $CuInSe_2$ (CIS; I-III-VI system) [17],

ZnSe can mutate into ternary $CuInSe_2$ in virtue of replacing two Zn atoms in ZnSe by one Cu and one In atom. Analogically, $ZnSnN_2$ (II-IV-V system) can be "created" by replacing the wurtzite group III sublattice of the III-nitrides by a combination of Zn (group II) and Sn (group IV) sublattices, with each nitrogen atom bound to two Zn and two Sn atoms, thus preserving nitrogen's octet rule [18].

More and more reports have shown that the ternary or quaternary compounds of Zn-IV-N_2 (where IV = Si, Ge, Sn) could be good candidate alternatives to current AlGaInN alloy materials. The latter have attracted consideration research attention and commercial prominence in the past three decades. Previous studies proved that the bandgaps of $In_xGa_{1-x}N$ semiconductors can be tuned across the whole visible spectrum by controlling the ratio of In to Ga, *i.e.*, *x* values in $In_xGa_{1-x}N$ alloys [19]. Recent results indicated that the mixed system of composition-controlled $ZnSn_xGe_{1-x}N_2$ [20] with tunable bandgaps over a wide range of 1.4 [21] to 3.4 eV [22] can be promising alternatives to $In_xGa_{1-x}N$ alloys.

Compared to the relatively new $ZnSnN_2$ material, while $ZnGeN_2$ and $ZnSiN_2$ materials have been studied since their successful growths were reported in 1970 [23] and 1992 [24], respectively. The difficulty in synthesis of electronic quality samples along with as-yet-unrevealed properties somehow hinders the progress of II-IV-N_2 materials to a large extent [25-26]. Nevertheless, with the prevalence of $ZnSnN_2$ and its related alloys and succeeding in synthesizing its bulk by our group in 2016 [27], we are deeply triggered by this situation where in-depth investigations should be filled in the gap of $ZnSnN_2$ material with our limited contributions.

1.3 Summary

This Introduction part outlines the importance and role of transparent semiconductor materials in human life and Nature starting with a puzzle, presents motivations of us group

for investigating zinc-based nitride semiconductors not only from the viewpoint of fundamental research but also from the appliance perspective.

1.4 Bibliography

[1] *The Nobel Prize in Physics 2014*, Retrieved from https://www.nobelprize.org/nobel_prizes/physics/laureates/2014/

[2] G. Rupprecht, Untersuchungen der elektrischen und lichtelektrischen Leitfähigkeit dü nner Indiumoxydschichten, Z. *Physik.* **139** p. 504 (1954).

[3] H. Kawazoe, M. Yasukawa, H. Hyodo, M. Kurita, H. Yanagi, and H. Hosono, *p*-Type electrical conduction in transparent thin films of $CuAlO_2$, *Nature* **389**, p. 939 (1997).

[4] Prof. Fumiyasu Oba's group, @ Tokyo Institute of Technology, Retrieved from http://www.titech.ac.jp/english/news/2016/035536.html or Y. Hinuma, T. Hatakeyama, Y. Kumagai, L. A. Burton, H. Sato, Y. Muraba, S. Iimura, H. Hiramatsu, I. Tanaka, H. Hosono, and F. Oba, Discovery of earth-abundant nitride semiconductors by computational screening and high-pressure synthesis, *Nat. Commun.* **7**, p. 11962 (2016).

[5] Prof. Walter R. L. Lambrecht's group, @ Case Western Reserve University, Retrieved from http://physics.case.edu/faculty/walter-lambrecht/ or J. H. Richter, B. J. Ruck, M. Simpson, F. Natali, N. O. V. Plank, M. Azeem, H. J. Trodahl, A. R. H. Preston, B. Chen, J. McNulty, K. E. Smith, A. Tadich, B. Cowie, A. Svane, M. van Schilfgaarde, and W. R. L. Lambrecht, Electronic structure of EuN: Growth, spectroscopy, and theory, *Phys. Rev. B* **84**, p. 235120 (2011).

[6] Team led by Prof. Andrew I. Cooper and Dr. Michael J. Bojdys @ University of Liverpool, Retrieved from http://phys.org/news/2014-06-triazine-based-graphitic-carbon-nitride-two-dimensional.html or G. Algara-Siller, N. Severin, S. Y. Chong, T. Björ -kman, R. G. Palgrave, A. Laybourn, M. Antonietti, Y. Z. Khimyak, A. V. Krasheni -nnikov, J. P. Rabe, U. Kaiser, A. I. Cooper, A. Thomas, and M. J. Bojdys, Triazine-Based, Graphitic Carbon Nitride: a Two-Dimensional Semiconductor, *Angew. Chem. Int. Ed.* **53**, p. 7450 (2014).

[7] Dr. Andriy Zakutayev's group, @ National Renewable Energy Laboratory (NREL), Retrieved from http://www.nrel.gov/materials-science/technology-readiness-levels.html or A. Zakutayev, A. J. Allen, X. Zhang, J. Vidal, Z. Cui, S. Lany, M. Yang, F. J. DiSalvo, D. S. Ginley, Experimental synthesis and properties of metastable $CuNbN_2$ and theoretical extension to other ternary copper nitrides, *Chem. Mater.* **26**, p. 4970 (2014).

[8] Electronegativity Table of the Elements, Retrieved from: http://www.tutor-homework.com/Chemistry_Help/electronegativity_table/electronegativity.html

[9] A. Zakutayev, C. M. Caskey, A. N. Fioretti, D. S. Ginley, J. Vidal, V. Stevanovic, E. Tea, and S. Lany, Defect tolerant semiconductors for solar energy conversion. *J. Phys. Chem. Lett.* **5**, p. 1117 (2014).

[10] J. Robertson and S. J. Clark, Limits to doping in oxides, *Phys. Rev. B* **83**, p. 075205 (2011).

[11] W. Walukiewicz, Intrinsic limitations to the doping of wide-gap semiconductors, *Phys. B* **302–303**, p 123 (2001).

[12] A. Zakutayev, Design of nitride semiconductors for solar energy conversion, *J. Mater. Chem. A* **4**, p. 6742 (2016).

[13] R. Juza and H. Hahn, Über die Kristallstrukturen von Zn_3N_2, Cd_3N_2 und Ge_3N_4. Metallamide und Metallnitride. IX. Mitteilung. (Eng: On the crystal structures of Zn_3N_2, Cd_3N_2 and Ge_3N_4 -Metal amides and metal nitrides IX. Announcement.), *Z. Anorg. Allg. Chem.* **224**, p. 125 (1940).

[14] K. Kuriyama, Y. Takahashi, and F. Sunohara, Optical band gap of Zn_3N_2 films, *Phys Rev B* **48**, p. 2781 (1993).

[15] M. Futsuhara, K. Yoshiokab, and O. Takaia, Structural, electrical and optical properties of zinc nitride thin films prepared by reactive rf magnetron sputtering, *Thin Solid Films* **322**, p. 274 (1998).

[16] N. Feldberg, B. Keen, J. D. Aldous, D. Scanlon, P. A. Stampe, R. Kennedy, R. Reeves, T. D. Veal, and S. Durbin, $ZnSnN_2$: A new earth-abundant element semiconductor for solar cells, in *Proceedings of the 38th IEEE Photovoltaic Specialists Conference (PVSC),* Austin, Texas, p. 2524 (2012).

[17] S. B. Zhang, S. H. Wei, A. Zunger, and H. Katayama-Yoshida, Defect physics of the $CuInSe_2$ chalcopyrite semiconductor, *Phys. Rev. B* **57**, p. 9642 (1998).

[18] A. Punya, W. R. L. Lambrecht, and M. van Schilfgaarde, Quasiparticle band structure of Zn-IV-N_2 compounds. *Phys. Rev. B* **84**, p. 165204 (2011).

[19] T. D. Veal, C. F. McConville, W. J. Schaff, *Indium Nitride and Related Alloys*, CRC press, Florida, 2010.

[20] P. Narang, S. Y. Chen, N. C. Coronel, S. Gul, J. Yano, L. W. Wang, N. S. Lewis, and H. A. Atwater, Bandgap tunability in Zn(Sn,Ge)N_2 semiconductor alloys, *Adv. Mater.* **26**, p. 1235 (2014).

[21] A. M. Shing, N. C. Coronel, N. S. Lewis, and H. A. Atwater, Semiconducting $ZnSn_xGe_{1-x}N_2$ alloys prepared by reactive radio-frequency sputtering, *APL Mater.* **3**, p. 076104 (2015).

[22] K. Du, C. Bekele, C. C. Hayman, J. C. Angus, P. Pirouz, and K. Kash, Synthesis and characterization of $ZnGeN_2$ grown from elemental Zn and Ge sources, *J. Crystal Growth* **310**, p. 1057 (2008).

[23] M. Maunaye and J. Lang, Préparation et Proprietés de $ZnGeN_2$, *Mater. Res. Bull.* **5**, p. 793, (1970).

[24] T. Endo, Y. Sato, H. Takizawa, and M. Shimada, High Pressure Synthesis of new compounds, $ZnSiN_2$ and $ZnGeN_2$ with distorted wurtzite structure, *J. Mater. Sci. Lett.* **11**, p. 424 (1992).

[25] J. Muth, A. Cai, A. Osinsky, H. Everitt, B. Cook, and I. Avrutsky, Optical properties of II-IV-N_2 semiconductors. *Mater. Res. Soc. Symp. Proc.* **831**, p. 745 (2005).

[26] J. E. Van Nostrand, J. D. Albrecht, R. Cortez, K. D. Leedy, B. Johnson, and M. J. O'keefe, Growth of II-IV-V_2 chalcopyrite nitrides by molecular beam epitaxy, *J. Electron. Mater*. **34** p. 1349 (2005).

[27] F. Kawamura, N. Yamada, M . Imai, and T. Taniguchi, Synthesis of $ZnSnN_2$ crystals via a high-pressure metathesis reaction, *Cryst. Res. Technol.* **51**, p. 220 (2016).

Chapter 2

Backgrounds and Historical Review

Strive not to be a success, but rather to be of value.

—Albert Einstein

2.1 Brief Overview of Transparent Conductors (TCs)

When speaking of the TCs, the very transparent conducting oxides (TCOs), which have been creating glorious generations, will pop up in one's mind who expertizes in material science. Conceptually, TCOs are a unique system of both optically transparent (more than 80%) and electrically conductive (about 10^3 S/cm or higher) oxide-based materials. These two characters are, in fact, a trade-off. The first TCO material (CdO thin film) reported by Bädeker can be traced back in 1907 [1], a century ago.

2.1.1 Transparent Conducting Oxides

Little practical development of TCOs was "seen" after the discovery of CdO until mid-20^{th} century. During the past three decades, a progressively accelerating signs of dramatic achievements in TCOs have been witnessed in our virtually everyday life. Nevertheless, even though a high level of technological ability has already been reached, conventional TCOs (ZnO [2-4], tin-doped indium oxide (In_2O_3:Sn, abbreviated ITO) [5-7], tin oxide together with fluorine-doped tin oxide (SnO_2:F, abbreviated FTO) [8-10], cadmium

stannate (Cd_2SnO_4) [11-12], and so forth) each have challenging drawbacks that dimmed their application prospects, such as controlling the unintentional *n*-type conductivity and thus achieving acceptor doping for ZnO; high cost of indium metal for ITO; and toxicity concern with cadmium for Cd_2SnO_4.

2.1.2 Transparent Conductive Nitrides

In both fundamental and applied science, it is notable that conventional TCOs do not exclusively compose TCs, other transparent, electrically conductive materials include thin metal films (such as gold and silver, in Refs. [13-15]), carbon nano-composites [16-18], and the recently "rediscovered" graphene [19-21], *etc.* are also members of TCs. However, it should be noted that for layer thickness of these materials higher than a few nanometers or even monolayers can dramatically reduce their transmittance, limiting the optoelectronic device output when these materials are used. In comparison to these materials, for which broad, comparative property data exist, very little appears in the literature regarding the TCNs. Of the diverse selection of possible TCNs available, only group III-nitrides (the so-called III-nitrides; *e.g.*, AlN [22-23], GaN [24-27], and InN [28-29] and their binary/ternary alloy compounds (*i.e.*, the AlGaInN materials system [30-31]) have been attracting tremendous interest for modern electronic and optoelectronic applications.

By contrast, metal nitrides (abbreviated MNs) other than the well-studied group III-nitride materials have scarcely been exploited as TCs. Starting recently, binary MN Sn(II/IV)-N compound (SnN), has just remained in the basic researches of synthesis and the attempts of structural identification [32].

Another binary MN, copper(I) nitride (Cu_3N; cubic anti-ReO_3 structure) exhibits a remarkable structure feature: the Cu(I) ions form collinear bonds with two nearest neighbor nitrogen anions [33], which forms a relatively "open", namely empty body center, structure. Hence, Yamada *et al*. have successfully obtained *n*-type lithium-inserted Cu_3N (Li_xCu_3N)

films through *p*-type Cu_3N films, thus causing a *p*- to *n*-type conversion and nonmetal−metal transition [34]. Besides, they synthesized truly transparent *p*-type *γ*-CuI films via a chemical reaction between Cu_3N thin films and solid-phase iodine. Furthermore, semiconductor Cu_3N has been reported to exhibit defect tolerance, namely a tendency to retain its properties despite the presence of crystallographic defects [35-36], which makes it possible to achieve bipolar doping behavior (N (donor-type defect) vacancies and Cu (acceptor-type defect)). The bipolar dopability is a sharp contrast with the GaN case [37].

Another case of MNs is ternary metal nitrides. Very recently, some intriguing phenomena have appeared for the Zn-IV-N_2 system where IV represents Ge, Si, Sn. Not only from theoretical calculations but also from experimental results, such a ternary MN can be considered as a pseudo III-nitride [38-42]. $ZnSn_xGe_{1-x}N_2$ semiconductor alloys have similar crystal structure and electronic structure to those of $In_xGa_{1-x}N$ system [42]. Apart from this, the bandgap in the $ZnSn_xGe_{1-x}N_2$ system can be tuned from 1.4 eV [43] (elsewhere reported 1.5 [41] or 2 eV [42]) for $ZnSnN_2$ to 3.4 eV [44] (elsewhere reported 3.3 [45] or 3.1 eV [42]) for $ZnGeN_2$. The bandgap tunability makes it potential alternatives for use in high-efficiency solar energy-conversion systems.

Except the conventional TCOs, well-studied thin metal films and group III-nitrides (together with their alloy series), even the “rediscovered” graphene, other MNs are full of uncertainty and challenge awaiting further research.

2.2 Overview and Research Status of Zinc-Based Nitrides

The descriptions above in Part 2.1 imply that other intriguing and less-explored semiconductor materials with unique properties and performance can be found or resurged, which is critical to advances in both science and industry, thus motivating me to start my work as a newcomer in semiconductor field and focus on certain “relatively new” materials to fill in some gaps of these materials.

2.2.1 Review of Zn_3N_2 Material on Current Status and Future Prospects

2.2.1.1 Refined Structure of Zn_3N_2

Four years after Kuriyama *et al.* reported Zn_3N_2 films, Partin *et al*. [46], in 1997, fully refined the structure of Zn_3N_2 from neutron time-of-flight powder diffraction data. For anti-bixbyite structural Zn_3N_2, unit cell lattice parameter of 0.9769 nm, Zn atoms are in tetrahedral sites of an approximately cubic close packed array of N atoms. N atoms occupying two differential positions, *i.e*., N(1) and N(2), constitute a face-centered cubic (FCC) structure with Zn atoms occupying 3/4 of the tetrahedral sites. If we refer to CaF_2 structure, N atoms and Zn atoms occupy the Ca positions and 3/4 of the F positions, respectively. The residual 1/4 unoccupied tetrahedral sites bring about Zn atoms a slight distortion of the formed FCC structure (see Figure 2.1). Owing to this distortion, the four Zn–N bond lengths are not all equal, a Zn atom in the tetrahedral site thus has three differential bond lengths with its nearest-neighbor N(2) atoms (see Table 2.1). The refined structure parameters of Zn_3N_2 and a computer simulation model of cell structure with 80 atoms for pure Zn_3N_2 are shown, respectively, in Table 2.1 and Figure 2.1 thereunder.

Table 2.1. Atomic position and bond lengths in units of Å for Zn_3N_2 material with space group $Ia\bar{3}$ (space group number 206), from Partin's work [46].

	Wyckoff Positions	***x***	***y***	***z***		**Bond Lengths**
Zn	48e	0.3975(1)	0.1498(2)	0.3759(1)	Zn–N(1)	2.133(2)
					Zn–N(2)	1.996(1)
N(1)	8b	1/4	1/4	1/4		
					Zn–N(2)	2.068(1)
N(2)	24d	0.9784(1)	0	1/4		
					Zn–N(2)	2.262(1)

Note: The letters (*i.e.*, e, b, d) stand for Wyckoff letters, which are simply labels and have no physical meaning.

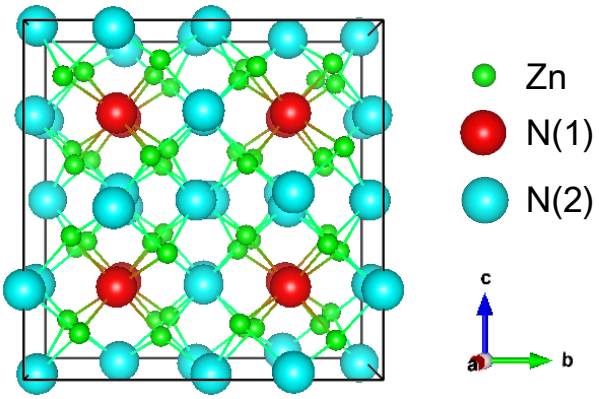

Figure 2.1. Perspective view of simulated structure model of Zn_3N_2 by a three-dimensional (3D) visualization program for structural models, namely VESTA. The structure model was simulated by ionic radius. The unit cell is outlined with black solid lines.

2.2.1.2 Promising Applications of Zn_3N_2

With the determination of structure of Zn_3N_2 in 1997, since the late 1990s, there has been a marked increase in the occurrence of Zn_3N_2 research. Due to its special structure, reported high-mobility and good transparency, reports concerning the promising applications of zinc nitride as a multifunctional material has emerged with an exhilarating speed.

A) ***Thin Film Transistors (TFTs)*** TFT technology is a well-known electrical technology due to its wide commercial applications, such as integrated circuits, sensors, detectors, especially active-matrix liquid-crystal displays (AMLCDs) and organic light-emitting diode (OLED) displays. TFT LCDs are becoming the mainstream display appliance but their manufacturing challenges reside with process yield and economy. Besides, the largest issues of the famous hydrogenated amorphous silicon TFTs reside with low mobility around 1 $cm^2\ V^{-1}\ s^{-1}$ and instability [47]. Hence, alternative material needs to be found and studied. Zn_3N_2 this inorganic compound can be reckoned as a potential candidate thanks to its high mobility 156 $cm^2\ V^{-1}\ s^{-1}$ [48], low resistivity [49] and low-cost fabrication process, and feasible high breakdown voltage [50]. Zinc nitride as channel layer in TFT exhibited promising transistor characteristics after nitrogen annealing in [51]. Núñez and coworkers

[52] used Zn_3N_2 films, with mobilities up to 100 $cm^2\ V^{-1}\ s^{-1}$ and bandgap in a range of 1.2–1.3 eV, as active layers in bottom- and top-gate TFTs. They found bottom-gate TFTs showed transistor characteristics without annealing process. Though performance is still below average Si-based TFTs, with development of zinc nitride material, high-mobility Zn_3N_2-based thin film will turn into a novel material platform for TFT system.

B) *p-type ZnO:N* For the famous oxide case of ZnO thin film, it shows naturally only *n*-type conductivity being that a large number of native defects, such as oxygen vacancies and zinc interstitials exist within film, which bring about difficulty in doping reproducible and reliable *p*-type ZnO. Although first-principles total-energy calculations suggests, for group-V elements like P and As elements, achieving shallow acceptor level is difficult, it is believed that N maybe the best elemental dopant source for *p*-type ZnO [53]. It has been reported that nitrogen doping ZnO *p*-type using N_2O, NH_3, and other sources [54-56] could be achieved. To date, there are some reports of zinc nitride being used to prepare *p*-type ZnO films. In 2002, Li's group succeeded in obtaining high-quality *p*-type thin films by thermal annealing Zn_3N_2 thin films in an oxygen ambient [57]. Afterwards, more and more groups from all over the world have been making great efforts to obtain N-doped *p*-type ZnO, *i.e.*, ZnO:N in virtue of Zn_3N_2 as a precursor material [58-60].

C) *Sensor* As a widely used in gas sensing material, ZnO exhibits sensitivity to many gases and satisfactory stability but with too high operating temperature [61]. As high-mobility material Zn_3N_2, when introduce Zn_3N_2 into ZnO, promoted electron mobility and promising enhanced gas-sensing properties of Zn_3N_2/ZnO (ZnNO) composites-based sensor can desirably achieved. Qu *et al*. [62] made this come into being by presenting hybrid ZnNO sensor which shows selectivity and high sensitivity toward acetone vapor.

D) *Solid-State Lighting (SSL)* With development of Zn_3N_2 material, recent ongoing research efforts [63-65] dedicated for fabricating Zn_3N_2-based (Zn_3N_2 nanowires, Zn_3N_2 crystals, Zn_3N_2 thin films, Zn_3N_2 hollow structures) optoelectronic devices have

demonstrated this material can be emitted in the ultraviolet, visible and near infrared (UV-Vis-IR) range.

2.2.1.3 Issue on Chemical Stability of Zn_3N_2

Zinc nitride crystal has a decomposition temperature of 700 °C, given in [66]. For zinc nitride powder prepared by nitridation reaction, it was found to be unstable when exposed to open air above 500 °C [67]. While the powder obtained by ammonolysis reaction is unstable in an oxygen atmosphere over 450 °C. [68]. The stability of zinc nitride in a reducing atmosphere is very low and can be easily reduced by hydrogen [69]. Therefore, for zinc nitride thin films (considered as "2D materials", ambiguously), the chemical stability issue will become a challenge and more unmanageable.

In almost every published papers regarding zinc nitride films, when exposed to ambient air, the tendency of nitride oxidation and hydrolysis turns out to be an inevitable knotty problem. Detailed reports have investigated the effect of air exposure on properties of zinc nitride films: Núñez *et al.* [70] found the oxidation rate of as-grown Zn_3N_2 film deposited at 200 °C is lower than at RT. X-Ray Photoelectron Spectroscopy (XPS) measurements were carried out to detect the surface chemical composition and indicated zinc nitride is easily hydrolyzed under the air exposure conditions [71].

In order to shed light on this difficulty, Bär *et al.* even suggested a degradation mechanisms according to the reaction of zinc nitride content with atmospheric humidity [72]. No literature has heretofore reported on achieving the oxidation/hydrolysis-proof zinc nitride thin films. Thus, preserving zinc nitride thin film in a vacuum chamber is an impermanent treatment. Note that the electrical properties of one day air-exposed film shows no significant difference when compared with other as-grown films, from the current−voltage characteristic curves obtained for different exposure times in air [73]. Note also that in an argon atmosphere, Zn_3N_2 powder is stable up to its decomposition point at around 700 °C

[68], which gives us an indication that preserving Zn_3N_2 with Ar may be a good way to prevent nitride oxidation/hydrolysis.

2.2.1.4 Issue on Oxygen Effect in Zn_3N_2

In the sight of chemical activity, oxygen is higher than that of nitrogen, making Zn preferentially combine with oxygen rather than with nitrogen when preparing Zn_3N_2 material. Not only the first principle's calculations carried out by Long *et al.*[74-76], but also from experimental results from distinct research groups using XPS measurements [71, 77], Energy Dispersive X-Ray (EDX) [78-79] or/and resonant Rutherford Backscattering (RBS) techniques [80], oxygen is proved to affect the structural, electrical and optical properties of Zn_3N_2 material. The oxygen sources maybe come from both during film-growth (*in-situ*; residual oxygen and/or H_2O); O_2 unintentionally introduced by mass flow controller (MFC) and air exposure after film-growth (*ex-situ*). The process of operating in an argon atmosphere [81], or vacuum system, like radio-frequency (RF) sputtering process [71, 73, 77], even in ultra high vacuum systems, like Plasma-assisted Molecular Beam Epitaxy [82], Radio Frequency Molecular Beam Epitaxy (RF-MBE) [48] or Pulsed Laser Deposition (PLD) [83], oxygen is detectable in all published paper, which means oxygen-free Zn_3N_2 material has been hitherto undiscovered yet. Although each published literature indicates that oxygen is inevitable when prepared Zn_3N_2 material, no detailed discussion has been carried out on the issue of oxygen effect in Zn_3N_2.

2.2.1.5 Issue on Electron Transport Mechanisms in Zn_3N_2

High-mobility in polycrystalline form film is rather a dramatic feature when earlier time Zn_3N_2 thin films was fabricated. A reported electron mobility as high as 156 $cm^2V^{-1}s^{-1}$ with electron density > 10^{19} cm^{-3} was obtained in an RF-MBE film [48]. This character is easily reproducible among different groups with various deposition methods [48, 71, 78]. Besides, low resistivity < 10^{-3} Ω cm (*i.e.*, conductivity > 10^3 S/cm) can also been attained in thus material [49]. However, the origins of electrical properties remains unclear, which infers that further investigations on electron transport mechanism need to be conducted.

2.2.1.6 Issue on Bandgap Energy Determination of Zn_3N_2

As a nitride material, zinc nitride is relatively less studied and poorly understood when compared with ZnO, InN, or GaN. It is possibly due to the fact that Zn_3N_2 tends to oxidize under ambient conditions. Such problem hinders the characterizations of electrical and optical for Zn_3N_2 material. Given that no reports have been demonstrated the pristine Zn_3N_2, the determination of its intrinsic bandgap energy has remained a controversial issue by now, which is to say fabrication of the nearly-intrinsic film is still inaccessible due in part to its small exothermic formation enthalpy (–22.6 kJ mol^{-1}) [84]. In fact, its heretofore reported bandgaps range from 1.01 [50] to 3.4 eV [85]. This current lack of bandgap issue understanding is absolutely a barrier to the further development of Zn_3N_2-based appliance.

2.2.2 Review of $ZnSnN_2$ Material on Current Status and Future Prospects

2.2.2.1 Promising Applications of $ZnSnN_2$

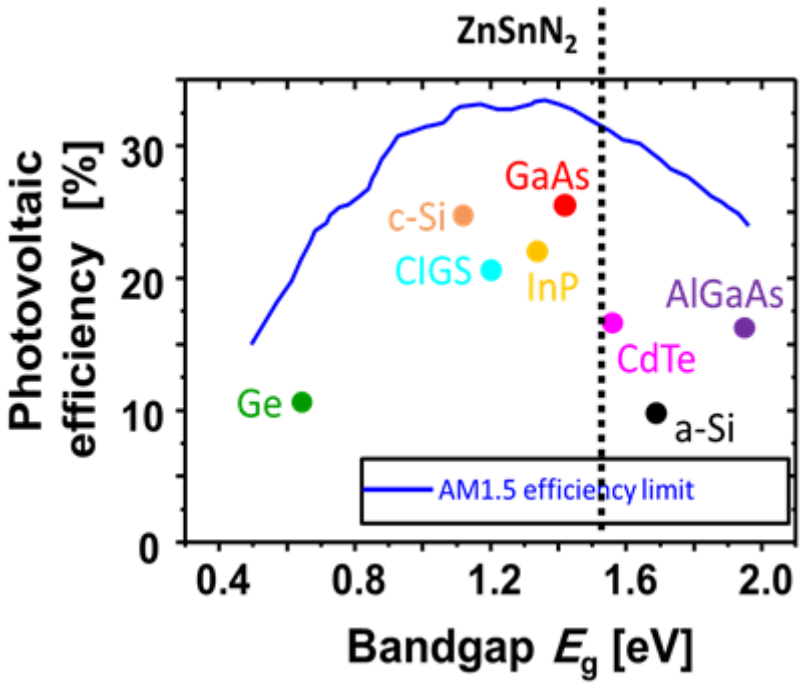

Figure 2.2. Graphical presentation of efficiency limit of solar cells for AM1.5 solar radiation spectra (solid line) with inserted points for representative conventional solar cells.

The electronic calculations carried out by Lahourcade's team [40] indicated $ZnSnN_2$ having a direct bandgap of 1.42 eV at zero Kelvin. From relation between PV efficiency and semiconductor bandgap calculated based on the famous Shockley–Queisser Efficiency Limit (detailed balance limit, Ref. [86]), as shown in Figure 2.2 above, the predicted bandgap of 1.42 eV is of high interest for a PV absorber. This dramatic feature makes $ZnSnN_2$ an excellent potential alternative to III-N system with the added benefit of being comprised of Earth-abundant, environmental-friendly and economy-efficiency elements.

On the other hand, the feasible tunability of bandgaps of $Zn(Si,Ge,Sn)N_2$ alloys makes them meet the requirements of electronic and optoelectronic applications including but not limited to PV systems (single *p–n* junction or tandem solar cell), such as SSL [87].

2.2.2.2 Issue on Structure Determination of $ZnSnN_2$

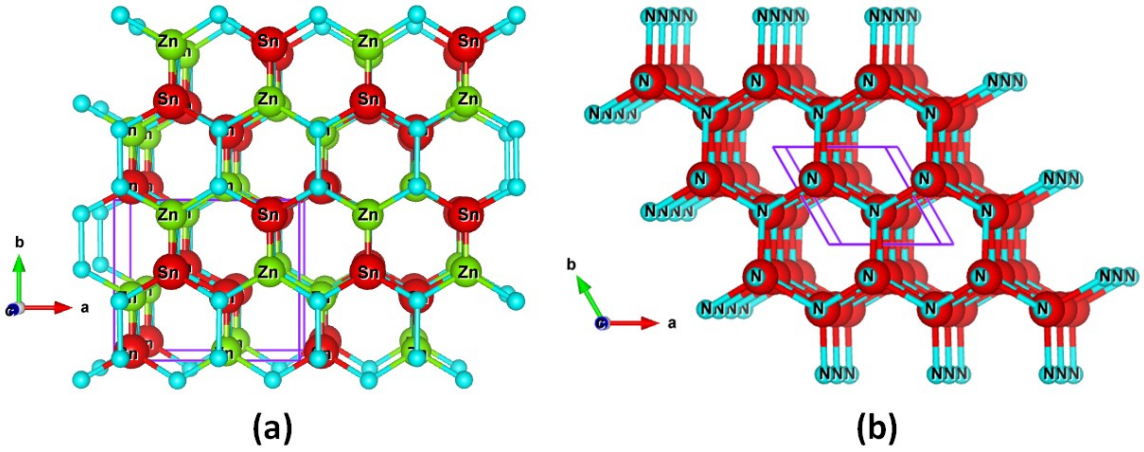

Figure 2.3. Schematic model of $ZnSnN_2$ by VESTA: (a) Orthorhombic structure (fully ordered cation sublattice; β-$NaFeO_2$ type) [calculated from data in Ref. 88]; Zn and Sn atoms arrange in a high-symmetry way and marked with labels while unmarked ones represent N atoms. (b) Monoclinic structure (disordered cation sublattice; wurtzite-like) [parametrized in Ref. 39]; Shown by the same color spheres, Zn and Sn atoms randomly arrange in cation sublattice, *i.e.*, random Zn/Sn ordering, and N atoms are marked with labels. The unit cell for each possible structure is outlined with purple solid lines.

As a relatively "young" material, the absolute structure of $ZnSnN_2$ remains unknown. As seen in Figure 2.3, there are currently two kinds of possible structures. The orthorhombic type consists of wurtzite-derived structures where Sn and Zn alternately displace the cations in the wurtzite structure, while in the random-wurtzite-like type, the cation sites are randomly occupied by Sn and Zn. As an analogue to III-nitride materials where the most stable structure usually assigned to the hexagonal wurtzite $P6_3mc$ structure [89], $ZnSnN_2$ has been theoretically predicted by Lahourcade, *et al.* [40] that its possible most stable structure belongs to wurtzite-derived orthorhombic $Pna2_1$ (Zn and Sn atoms are ordered in a way of orthorhombic symmetry instead of hexagonal). It should be mentioned here that, Lahourcade, *et al.* also found that, in the very same work, under certain growth conditions, wurtzite- and zinc-blende-derived orderings may coexist in $ZnSnN_2$ material due to small energetic difference between these two phases.

However, Feldberg *et al.* [39] indicated another experimental observation that a single crystal $ZnSnN_2$ film prepared by PAMBE technique inclined to exhibit a monoclinic structure. In fact, the similar situation occurred also in the earlier more-studied case of $ZnGeN_2$ material: the determination of its crystal structure underwent renovation during its development. Historically, when Maunaye and Lang [90] first synthesized $ZnGeN_2$ and reported it monoclinic structure; afterwards Wintenberger *et al*. [91] demonstrated that its actual structure is orthorhombic with space group $Pna2_1$. Hence, further research is strongly warranted with respect to the structure determination of $ZnSnN_2$ material.

2.2.2.3 Issue on Difficulty in Growing High-Quality $ZnSnN_2$

As discussed in Part 1.2.2, one possible obstacle factor that restricts the development of $ZnSnN_2$ material resides in difficulty in synthesizing the electronic quality samples, especially compared to the well-studied CIS material. Usually, the ideal syntheses of Zn-IV-N_2 compounds are under high-pressure and high-temperature conditions [92]. Noted that the world-first synthesis of $ZnSnN_2$ single crystal [93] also succeeded under these severe conditions. In fact, Narang and Chen's group [94, 41] had theoretically calculated

the formation energy for both $ZnGeN_2$ and $ZnSnN_2$ cases and found the formation energy of $ZnGeN_2$ is much larger than that of $ZnSnN_2$ ($\Delta H_f(ZnGeN_2)$ = –1.31 eV/f.u.; $\Delta H_f(ZnSnN_2)$ = –0.17 eV/f.u.), indicating that it is much more difficult to synthesize single-phase $ZnSnN_2$ than $ZnGeN_2$. This also explains the above-mentioned synthesis history of $ZnGeN_2$ 50 years earlier than $ZnSnN_2$ case. With increment of extra elements including but not limited to group-IV elements (*e.g.*, oxygen impurity like Zn_3N_2 case), controlling the material composition and obtaining the nearly ideal (*i.e.*, stoichiometrical single-phase) compounds turn out to be of great challenge.

2.2.2.4 Issue on Relatively High Electron Density in $ZnSnN_2$

For the grown $ZnSnN_2$ thin films, electron densities as high as ~10^{21} $cm^2V^{-1}s^{-1}$ (almost metallic) are typically perceptible in Refs. [40, 95-96]. Such high electron densities are consistent with heavy donor doping as illustrated in Refs. [39-40], which infers that the conduction band filling, *i.e.*, the well-known Burstein-Möss effect is responsible for the altering of fundamental bandgap energy of $ZnSnN_2$ (predicted value of 1.42 eV in Ref. [40], or another predicted value of 2.02 eV in [88]). This situation at present may be understood partly by the emerged literature reporting that the inevitable oxygen impurity can lead to unintentional heavy donor doping during the film-growth process [40]. Also discussed was another influence factor, metal-rich deposition condition (or to say, poor nitrogen incorporation), in [94], where the coexistence of secondary phases such as Zn, Sn metals or formed Zn_3N_2 can be one possible origin of the high electron density. For PV applications, reliable synthesis of film with a relevant carrier density range on the order of ~ 10^{17} cm^{-3} is usually preferable. Therefore, effective strategies to avoid the presence of oxygen impurities and the formation of relative secondary phases are critical to the improvement of $ZnSnN_2$ semiconductor in its future applications.

2.2.2.5 Issue on Bandgap Energy Determination of $ZnSnN_2$

Similar to cousin $ZnGeN_2$ material, estimation of bandgap of $ZnSnN_2$ is hard to attained. Note here, parenthetically, as in the case of $ZnGeN_2$, an earlier study by Larson *et al.* [97]

gave an estimated bandgap of 2.67 eV, Kikkawa and Morisaka [98] estimated a bandgap energy of 3.1 eV from the direct optical absorption edge, in comparison to Larson *et al.*'s results in which estimated bandgap value is probably due to the subband-gap defect absorption. A polycrystalline $ZnGeN_2$ film with superior optical quality [44] gave a 3.40 ± 0.01 eV excitonic bandgap from the photoluminescence (PL) measurements at ~4 K.

The situation of bandgap estimation for the case of $ZnSnN_2$ also remains ambiguous. There is still controversial on its band structure and band gap energy both from theoretical and experimental viewpoints, as illustrated following.

Lahourcade *et al.* [40] carried out electronic structure calculations to predict that $ZnSnN_2$ has orthorhombic structure with a direct bandgap value of 1.42 eV at zero Kelvin. Another theory research group Punya *et al.* [88] yet reported $ZnSnN_2$ to be of orthorhombic structure having a direct bandgap of 2.02 eV.

Quayle *et al.* used plasma-assisted vapor-liquid-solid technique for synthesis of $ZnSnN_2$ and reported a "wurtzite-like" structure with two measured bandgaps: 1.7 ± 0.1 eV for photoluminescence excitation (PLE) measurement and a broad PL peak between 1.3 and 1.7 eV for PL measurements, as presented in Ref. [99]. Electron densities were not given because their films were formed atop Zn melt, which was meaningfulness for Hall measurements. They interpreted such broad range as defect luminescence and considered the PLE value as intrinsic gap. However, another independent group Veal *et al.* [95] employed MBE technique to synthesize single crystal $ZnSnN_2$ films to characterize its optical properties and found that the observed absorption edges ranged from 1.0 to 2.0 eV for films with n_e varying in a range of 10^{19}~10^{21} cm^{-3}. What's interesting here, the same group which predicted bandgap lies in 1.42 eV at zero Kelvin, had also measured the optical absorption edge near 2 eV for their thin films (electron density n_e 10^{19}~10^{21} cm^{-3}) deposited by reactive RF magnetron sputter technique in just the same work [40].

There are two main reasons for illustrating such big discrepancy of bandgap energies among different and independent groups. One is conduction band filling, namely, the Burstein-Möss effect and the other resides in the degree of cation disorder. For the former reason, because most of the reported electron densities are in a range of 10^{19}~10^{21} cm^{-3}, probably leading to conduction band filling and the resulting Burstein-Möss effect. For the latter one, more and more papers conform its existence. Like, Veal's group found a fundamental bandgaps of $ZnSnN_2$ films varying from 1.0 to 2.0 eV as the cation ordering increased, and of course also the existing Burstein-Möss effect [39, 95].

From backgrounds and research issues discussed in Parts 2.2.1 and 2.2.2 above, there are still numerous undiscovered and unreached properties for these very "young" zinc-based nitride materials awaiting further revealed, which remains challengeable to a certainty.

2.3 Approaches and Aims of This Dissertation

This dissertation presents thin film growth by reactive RF magnetron sputtering technique and property characterizations for binary Zn_3N_2 material and ternary $ZnSnN_2$ material, and also discusses their promising applications as versatile semiconductors. This work is organized in the order of "Questions Posed; Questions Analyzed; Questions Settled" with the following three aims.

- The first aim of this work lies in obtaining our high-quality sputtered material films under optimal conditions, and characterized the achieved material films through techniques which consist of (i) structural characterization usage (X-ray diffraction (XRD), X-ray reflectivity (XRR), X-ray photoelectron spectroscopy (XPS), scanning electron microscopy (SEM)); (ii) electrical characterization usage (electrical resistivity, Hall effect measurements and thermopower measurements); (iii) optical characterization usage (optical transmittance and reflectance measurements).

- The second aim of this work is to further understand the structural properties and origin of electrical and optical properties of achieved polycrystalline and epitaxial material films. Epitaxial films were grown to discuss the influence of film crystallinity and grain boundary on electron transport in films. Intentional oxygen-doping in polycrystalline Zn_3N_2 films was conducted to attain films with low resistivity on the order of 10^{-4} Ω cm and to illustrate the impact of oxygen impurities on properties by comparing both intentional and unintentional O_2-doped $Zn_3N_{2-x}O_x$ films.

- The third aim of this work resides within filling in some gap of $ZnSnN_2$ material through attempts to further decreasing its high electron density and deriving its effective electron mass. In order to fulfilling these goals, Cu(I)-doping into $ZnSnN_2$ films and optical property analyses were carried out. Similar to Zn_3N_2 case, oxygen can also unintentionally be incorporated into $ZnSnN_2$ films, and therefor effect of co-doping of oxygen and copper on properties of $ZnSnN_2$ films needs to be investigated as well.

The work presented here is designed to expand diversity from TCOs to TCNs and fill in some gaps of the studied materials by investigating the growth and characterization of their films materials, in which the constituents are entire Earth-abundant, environmentally-benign, economy-efficiency elements. Such a work contributes, though to a certain extent to provide additional evidences in support of the fact that our study objects can be considered as potential candidates for a broader range of electronic, optoelectronic and photovoltaic applications.

2.4 Summary

In this chapter, a brief overview of transparent conductors including transparent conductive oxides and nitrides; our motivators of being absorbed in zinc-based nitride (here, *i.e.*, zinc nitride and zinc tin nitride) thin films; historical backround review, state-of-the-art research

progress, remaining research gaps of related materials; and scopes & aims & meaning of this work are presented. In order to consider such “relatively-young” materials as versatile semiconductors, more detailed information should be given to understand as fully as possible their fundamental properties involved.

2.5 Bibliography

[1] K. Bädeker, Über die elektrische Leitfähigkeit und die thermoelektrische Kraft einiger Schwermetallverbindungen, *Ann. d. Physik* (Leipzig) **22**, p. 749 (1907).

[2] F. A. Selim, M. H. Weber, D. Solodovnikov, and K. G. Lynn, Nature of native defects in ZnO, *Phys. Rev. Lett.* **99**, p. 085502 (2007).

[3] C. H. Park, S. B. Zhang, and S. H. Wei, Origin of *p*-type doping difficulty in ZnO: The impurity perspective, *Phys. Rev. B* **66**, p. 073202 (2002).

[4] J. C. Fan, K. M. Sreekanth, Z. Xie, S. L. Chang, and K. V. Rao, *p*-Type ZnO materials: Theory, growth, properties and devices, *Prog. Mater. Sci.* **58**, p. 874 (2013).

[5]Y. Shigesato, D. C. Paine, and T. E. Haynes, Study of the effect of ion implantation on the electrical and microstructural properties of tin-doped indium oxide thin films, *J. Appl. Phys.* **73**, p. 3805 (1993).

[6] Z. X. Chen, W. C. Li, R. Li, Y. F. Zhang, G. Q. Xu, and H. S. Cheng, Fabrication of highly transparent and conductive indium-tin oxide thin films with a high figure of merit via solution processing, *Langmuir* **29**, p. 13836 (2013).

[7] I. Hamberg and C. G. Granqvist, Evaporated Sn-doped In_2O_3 films: Basic optical properties and applications to energy-efficient windows, *J. Appl. Phys*. **60**, p. R123 (1986).

[8] N. Noor and I. P. Parkin, Enhanced transparent-conducting fluorine-doped tin oxide films formed by aerosol-assisted chemical vapour deposition, *J. Mater. Chem.* **1** p. 984 (2013).

[9] K. Ellmer, Past achievements and future challenges in the development of optically transparent electrodes, *Nat. Photonics* **6**, p. 809 (2012).

[10] H. Hosono, Y. Ogo, H. Yanagi, and T. Kamiya, Bipolar conduction in SnO thin films, *Electrochem. Solid-State Lett.* **14**, p. H13 (2011).

[11] R. Mamazza Jr., D. L. Morel, and C. S. Ferekides, Transparent conducting oxide thin films of Cd_2SnO_4 prepared by RF magnetron co-sputtering of the constituent binary oxides, *Thin Solid Films* **484**, p. 26 (2005).

[12] K. Jeyadheepan, M. Thamilselvan, K. Kim, J. Yi, and C. Sanjeeviraja, Optoelectronic properties of RF magnetron sputtered cadmium tin oxide (Cd_2SnO_4) thin films for CdS/CdTe thin film solar cell applications, *J. Alloy. Compd.* **620**, p. 185 (2015).

[13] C. L. Li, Ö. Dag, T. D. Dao, T. Nagao, Y. Sakamoto, T, Kimura, O. Terasaki, and Y. Yamauchi, Electrochemical synthesis of mesoporous Au films toward mesospace-stimulated optical properties, *Nat. Commun.* **6**, p. 6608 (2015).

[14] Y. Sun and Y. Xia, Shape-controlled synthesis of gold and silver nanoparticles, *Science* **298**, p. 2176 (2002).

[15] A. A. High, R. C. Devlin, A. Dibos, M. Polking, D. S. Wild, J. Perczel, N. P. de Leon, M. D. Lukin, and H. Park, Visible-frequency hyperbolic metasurface, *Nature* **522**, p. 192 (2015).

[16] F. Yang, X. Wang, D. Q. Zhang, J. Yang, D. Luo, Z. W. Xu, J. K. Wei, J. Q. Wang, Z. Xu, F. Peng, X. M. Li, R. M. Li, Y. L. Li, M. H. Li, X. D. Bai, F. Ding, and Y. Li, Chirality-specific growth of single-walled carbon nanotubes on solid alloy catalysts, *Nature* **510**, p.522 (2014).

[17] G. J. Brady, A. J. Way, N. S. Safron, H. T. Evensen, P. Gopalan, and M. S. Arnold, Quasi-ballistic carbon nanotube array transistors with current density exceeding Si and GaAs, *Sci. Adv.* **2**, p. e1601240 (2016).

[18] M. F. L. De Volder, S. H. Tawfick, R. H. Baughman, and A. J. Hart, Carbon nanotubes: Present and future commercial applications, *Science* **339**, p. 535 (2013).

[19] J. Rafiee, Xi Mi, H. Gullapalli, A. V. Thomas, F. Yavari, Y. Shi, P. M. Ajayan and N. A. Koratkar, Wetting transparency of graphene, *Nature Mater.* **11**, p. 217 (2012).

[20] D. Kuzum, H. Takano, E. Shim, J. C. Reed, H. Juul, A. G. Richardson, J. de Vries, H. Bink, M. A. Dichter, T. H. Lucas, D. A. Coulter, E. Cubukcu, and B. Litt, Transparent and flexible low noise graphene electrodes for simultaneous electrophysiology and neuroimaging, *Nat. Commun.* **5**, p. 5259 (2014).

[21] D. S. Hecht, L. B. Hu, and G. Irvin, Emerging transparent electrodes based on thin films of carbon nanotubes, graphene, and metallic nanostructures, *Adv. Mater.* **23**, p. 1482 (2011).

[22] C. Besleaga, G. E. Stan, I. Pintilie, P. Barquinha, E. Fortunato, and R. Martins, Transparent field-effect transistors based on AlN-gate dielectric and IGZO-channel semiconductor, *Appl. Surf. Sci.* **379**, p. 270 (2016).

[23] B. Peng, D. D. Gong, W. L. Zhang, J. Y. Jiang, L. Shu, and Y. H. Zhang, Effects of sputtering parameters on AlN film growth on flexible hastelloy tapes by two-step deposition technique, *Materials* **9**, p. 686 (2016).

[24] I. Akasaki, H. Amano, Y. Koide, K. Hiramatsu, and N. Sawaki, Effects of AlN buffer layer on crystallographic structure and on electrical and optical properties of GaN and $Ga_{1-x}Al_xN$ ($0 < x \leqq 0.4$) films grown on sapphire substrate by MOVPE, *J. Crystal Growth* **98** p. 209 (1989).

[25]I. Akasaki, Nobel Lecture: Fascinated journeys into blue light, *Rev. Mod. Phys.* **87**, p. 1119 (2015).

[26] H. Amano, Nobel Lecture: Growth of GaN on sapphire via low-temperature deposited buffer layer and realization of *p*-type GaN by Mg doping followed by low-energy electron beam irradiation, *Rev. Mod. Phys.* **87**, p. 1133 (2015).

[27] S. Nakamura, Nobel Lecture: Background story of the invention of efficient blue InGaN light emitting diodes, *Rev. Mod. Phys.* **87**, p. 1139 (2015).

[28] K. S. Lye, A. Kobayashi, K. Ueno. J. Ohta, and H. Fujioka, InN thin-film transistors fabricated on polymer sheets using pulsed sputtering deposition at room temperature, *Appl. Phys. Lett.* **109**, p. 032106 (2016).

[29] M. Oseki, K. Okubo, A. Kobayashi, J. Ohta, and H. Fujioka, Field-effect transistors based on cubic indium nitride, *Sci. Rep.* **4**, p. 3951 (2014).

[30] I. Akasaki and H. Amano, Crystal growth and conductivity control of group III nitride semiconductors and their application to short wavelength light emitters, *Jpn. J. Appl. Phys.* **36**, p. 5393 (1997).

[31] N. Lu and I. Ferguson, III-nitrides for energy production: photovoltaic and thermoelectric applications, *Semicond. Sci. Technol.* **28**, p. 074023 (2013).

[32] C. M. Caskey, A. Holder, S. Shulda, S. T. Christensen, D. Diercks, C. P. Schwartz, D. Biagioni, D. Nordlund, A. Kukliansky, A. Natan, D. Prendergast, B. Orvananos, W. Sun, X.

Zhang, G. Ceder, D. S. Ginley, W. Tumas, J. D. Perkins, V. Stevanović, S. Pylypenko, S. Lany, R. M. Richards, and A. Zakutayev, Synthesis of a mixed-valent tin nitride and considerations of its possible crystal structures, *J. Chem. Phys.* **144**, p. 144201 (2016).

[33] R. W. G. Wyckoff, *Crystal Structures.* 2nd ed., Vols. 1 and 2, Wiley, New York, (1963).

[34] N. Yamada, K. Maruya, Y. Yamaguchi, X. Cao, and Y. Ninomiya, *p*- to *n*-Type conversion and nonmetal–metal transition of lithium-inserted Cu_3N films, *Chem. Mater.* **27**, p. 8076 (2015).

[35] A. Zakutayev, C. M. Caskey, A. N. Fioretti, D. S. Ginley, J. Vidal, V. Stevanovic, E. Tea, and S. Lany, Defect tolerant semiconductors for solar energy conversion. *J. Phys. Chem. Lett.* **5**, p. 1117 (2014).

[36] A. N. Fioretti, C. P.S chwartz, J. Vinson, D. Nordlund, D. Prendergast, A. C. Tamboli, C. M. Caskey, F. Tuomisto, F. Linez, S. T. Christensen, E. S. Toberer, S. Lany, and A, Zakutayev, Understanding and control of bipolar self-doping in copper nitride, *J. Appl. Phys.* **119**, p. 181508 (2016).

[37] H. Amano, M. Kito, K. Hiramatsu, and I. Akasaki, *p*-Type conduction in Mg-doped GaN treated with low-energy electron beam irradiation (LEEBI), *Jpn. J. Appl. Phys.* **28**, p. L2112 (1989).

[38] A. Punya, T. R. Paudel, and W. R. L. Lambrecht, Electronic and lattice dynamical properties of II–IV–N_2 semiconductors, *Phys. Status Solidi C* **8**, p. 2492 (2011).

[39] N. Feldberg, J. D. Aldous, W. M. Linhart, L. J. Phillips, K. Durose, P. A. Stampe, R. J. Kennedy, D. O. Scanlon, G. Vardar, R. L. Field III, T. Y. Jen, R. S. Goldman, T. D. Veal, and S. M. Durbin, Growth, disorder, and physical properties of $ZnSnN_2$, *Appl. Phys. Lett.* **103**, p. 042109 (2013).

[40] L. Lahourcade, N. C. Coronel, K. T. Delaney, S. K. Shukla, N. A. Spaldin, and H. A. Atwater, Structural and optoelectronic characterization of RF sputtered $ZnSnN_2$, *Adv. Mater.* **25**, p. 2562 (2013).

[41] S. Y. Chen, P. Narang, H. A. Atwater, and L. W. Wang, Phase stability and defect physics of a ternary $ZnSnN_2$ semiconductor: First principles insights, *Adv. Mater.* **26**, p. 311 (2014).

[42] P. Narang, S. Y. Chen, N. C. Coronel, S. Gul, J. Yano, L. W. Wang, N. S. Lewis, and H. A. Atwater, Bandgap tunability in Zn(Sn,Ge)N_2 semiconductor alloys, *Adv. Mater.* **26**, p. 1235 (2014).

[43] A. M. Shing, Na. C. Coronel, N. S. Lewis, and H. A. Atwater, Semiconducting $ZnSn_xGe_{1-x}N_2$ alloys prepared by reactive radio-frequency sputtering, *APL Mater.* **3**, p. 076104 (2015).

[44] K. Du, C. Bekele, C. C. Hayman, J. C. Angus, P. Pirouz, and K. Kash, Synthesis and characterization of $ZnGeN_2$ grown from elemental Zn and Ge sources, *J. Crystal Growth* **310**, p. 1057 (2008).

[45] T. Misaki, K. Tsuchiya, D. Sakai, A. Wakahara, H. Okada, and A. Yoshida: Growth and characterization of $ZnGeN_2$ by using remote-plasma enhanced metalorganic vapor phase epitaxy. *Phys. Status Solidi C* **0**, p. 188 (2002).

[46] D. E. Partin, D. J. Williams, and M. O'Keeffe, The crystal structures of Mg_3N_2 and Zn_3N_2, *J. Solid State Chem.* **132**, p. 56 (1997).

[47] Z. C. Feng editor, *Handbook of zinc oxide and related materials: Volume Two, Devices and Nano-engineering*, p. 512, CRC Press, 2012.

[48] T. Suda and K. Kakishita, Bandgap energy and electron effective mass of polycrystalline Zn_3N_2, *J. Appl. Phys.* **99**, p. 076101 (2006).

[49] N. Yamada, K. Watarai, T. Yamaguchi, A. Sato, and Y. Ninomiya, Transparent conducting zinc nitride films, *Jpn. J. Appl. Phys.* **53**, p. 05FX01 (2014).

[50] K. Toyoura, H. Tsujimura, T. Goto, K. Hachiya, R. Hagiwara, and Y. Ito, Optical properties of zinc nitride formed by molten salt electrochemical process, *Thin Solid Films* **492**, p. 88 (2005).

[51] E. Aperathitis, V. Kambilafka, and M. Modreanu, Properties of *n*-type ZnN thin films as channel for transparent thin film transistors, *Thin Solid Films* **518**, p. 1036 (2009)..

[52] C. G. Núñez, J. L. Pau, E. Ruíz, and J. Piqueras, Thin film transistor based on zinc nitride as a channel layer for optoelectronic devices, *Appl. Phys. Lett.* **101**, p. 253501 (2012)

[53] C. H. Park, S. B. Zhang, and S. H. Wei, Origin of *p*-type doping difficulty in ZnO: The

impurity perspective, *Phys. Rev. B* **66**, p. 073202 (2002).

[54] S. M. Choua, M. H. Hona, and I. C. Leu, Synthesis of *p*-type Al–N codoped ZnO films using N_2O as a reactive gas by RF magnetron sputtering, *Appl. Surf. Sci.* **255**, p 2958 (2008).

[55] C. Lee, S. Y. Park, J. Lim, and H.W. Kim, Growth of *p*-type ZnO thin films by using an atomic layer epitaxy technique and NH_3 as a doping source, *Mater. Lett.* **61**, p 2495 (2007).

[56] X. Y. Chen, Z. Z. Zhang, B. Yao, M. M. Jiang, S. P. Wang, B. H. Li, C. X. Shan, L. Liu, D. X. Zhao, and D. Z. Shen, Control of N/N_2 species ratio in NO plasma for p-type doping of ZnO, *J. Appl. Phys*. **110**, p. 053305 (2011).

[57] B. S. Li, Y. C. Liu, Z. Z. Zhi, D. Z. Shen, Y. M. Lu, J. Y. Zhang, X. W. Fan, R. X. Mu and Don O. Henderson, Optical properties and electrical characterization of *p*-type ZnO thin films prepared by thermally oxiding Zn_3N_2 thin films, *J. Mater. Res*. **18**, p. 8 (2003).

[58] C. Wang, Z. G. Ji, K. Liu, Y. Xiang, and Z. Z. Ye, *p*-Type ZnO thin films prepared by oxidation of Zn_3N_2 thin films deposited by DC magnetron sputtering, *J. Crystal Growth* **259**, p. 279 (2003).

[59] E. Kaminska, A. Piotrowska, J. Kossut, A. Barcz, R. Butkute, W. Dobrowolski, E. Dynowska, R. Jakiela, E. Przezdziecka, R. Lukasiewicz, M. Aleszkiewicz, P. Wojnar, and E. Kowalczyk, Transparent *p*-type ZnO films obtained by oxidation of sputter-deposited Zn_3N_2, *Solid State Commun.* **135**, p. 11 (2005).

[60] Y. Nakano, T. Morikawa, T. Ohwaki, and Y. Taga, Electrical characterization of *p*-type N-doped ZnO films prepared by thermal oxidation of sputtered Zn_3N_2 films, *Appl. Phys. Lett.* **88**, p. 172103 (2006).

[61] J. Q. Xu, Q. Y. Pan, Y. A. Shun, and Z. Z. Tian, Grain size control and gas sensing properties of ZnO gas sensor. *Sens. Actuat. B Chem.* **66**, p. 277 (2000).

[62] F. D. Qu, Y. Yuan, R. Guarecuco, and M. H. Yang, Low working-temperature acetone vapor sensor based on zinc nitride and oxide hybrid composites, s*mall* **12**, p 3128 (2016).

[63] P. N. Taylor, M. A. Schreuder, T. M. Smeeton, A. J. D. Grundy, J. A. R. Dimmock, S. E. Hooper, J. Heffernana, and M. Kauera, Structural properties and photoluminescence of

zinc nitride nanowires synthesis of widely tunable and highly luminescent zinc nitride nanocrystals, *J. Mater. Chem. C* **2**, p. 4379 (2014).

[64] Z. X. Zhang, X. J. Pan, L. X. Liu, Z. W. Ma, H. T. Zhao, L. Jia, and E. Q. Xie, Green photoluminescence from Zn_3N_2:Tb films prepared by magnetron sputtering, *J. Appl. Phys.* **105**, p. 016101 (2009).

[65] W. S. Khan, C. B. Cao, Z. Alia, F. K. Butt, N. A. Niaz, A. Baig, R. ud Din, M. H. Farooq, F. P. Wang, and Q. ul Ain, Solvo-solid preparation of Zn_3N_2 hollow structures; their PL yellow emission and hydrogen absorption characteristics, *Matter. Lett.* **65**, p. 2127 (2011).

[66] W. M. Haynes, *CRC Handbook of Chemistry and Physics (97th edition)*, §4–100 Physical Constants of Inorganic Compounds, CRC Press, 2016.

[67] F. J. Zong, H. L. Ma, C. S. Xue, H. Z. Zhuang, X. J. Zhang, H. D. Xiao, J. Ma, and F. Jia, Synthesis and thermal stability of Zn_3N_2 powder, *Solid State. Commun.* **132**, p. 521 (2004).

[68] G. Paniconi, Z. Stoeva, R. I. Smith, P. C. Dippo, B. L. Gallagher, and D. H. Gregory, Synthesis, stoichiometry and thermal stability of Zn_3N_2 powders prepared by ammonolysis reactions, *J. Solid State Chem.* **181**, p 158 (2008).

[69] M. D. Lyutaya and S. A. Bakuta, Synthesis of the nitrides of group II elements, translated from *Poroshkovaya Metallurgiya* **206**, p. 57 (1980).

[70] C. G. Núñez, J. L. Pau, M. J. Hernández, and J. Piqueras, Influence of air exposure on the composition nature of Zn_3N_2 thin film, *Thin Solid Films* **522**, p. 208 (2012).

[71] M. Futsuhara, K. Yoshiokab, and O. Takaia, Structural, electrical and optical properties of zinc nitride thin films prepared by reactive rf magnetron sputtering, *Thin Solid Films* **322**, p. 274 (1998).

[72] M. Bär, K. S. Ahn, S. Shet, Y. Yan, L. Weinhardt, O. Fuchs, M. Blum, S. Pookpanratana, K. George, W. Yang, J. D. Denlinger, M. Al-Jassim, and C. Heske, Impact of air exposure on the chemical and electronic structure of ZnO:Zn_3N_2 thin films, *Appl. Phys. Lett.* **94**, p. 012110 (2009).

[73] M. G. Castaño, A. R. Cubero, L. Vazquez, and J. L. Pau, Analysis of zinc nitride resistive indicators under different relative humidity conditions, *ACS Appl. Mater. Interfaces* **8**, p. 29163 (2016).

[74] R. Long, Y. Dai, L. Yu, M. Guo, and B. B. Huang, Structural, electrical, and optical properties of oxygen defects in Zn_3N_2, *J. Phys. Chem. B* **111**, p. 3379 (2007).

[75] R. Long, Y. Dai, L. Yu, B. B. Huang, and S. H. Han, Atomic geometry and electronic structure of defects in Zn_3N_2, *Thin Solid Films* **516**, p. 1297 (2008).

[76] R. Long, Y. Dai, M. Guo, and K. S. Yang, Native defects and impurities in Zn_3N_2: first-principle studies using gradient-correction approximation, *Phy. Scripta* **340**, p. T129 (2007).

[77] T. L. Yang, Z. S. Zhang, Y. H. Li, M. S. Lv, S. M. Song, Z. C. Wu, J. C. Yan, and S. H. Han, Structural and optical properties of zinc nitride films prepared by rf magnetron sputtering, *Appl. Surf. Sci.* **255**, p. 3544 (2009).

[78] N. K. Jiang, D. G.Georgiev, A. H.Jayatissa, R. W. Collins, J. Chen, and E. McCullen, Zinc nitride films prepared by reactive RF magnetron sputtering of zinc in nitrogen containing atmosphere, *J. Phys. D: Appl. Phys.* **45**, p. 135101 (2012).

[79] T. Wen, M. Gautam, A. M. Soleimanpour, and A. H. Jayatissa, Thermal annealing effect on zinc nitride thin films deposited by reactive rf-magnetron sputtering process, *Mater. Sci. Semicon. Proce.* **16**, p. 318 (2008).

[80] C. G. Núñez, J. L. Pau, M. J. Hernández, M. Cervera, E. Ruiz, and J. Piqueras, On the zinc nitride properties and the unintentional incorporation of oxygen, *Thin Solid Films* **520**, p. 1924 (2012).

[81] K. Toyoura, H. Tsujimura, T. Goto, K. Hachiya, R. Hagiwara, and Y. Ito, Optical properties of zinc nitride formed by molten salt electrochemical process, *Thin Solid Films* **492**, p. 88 2005).

[82] T. Oshima and S. Fujita, (111)-Oriented Zn_3N_2 growth on *a*-plane sapphire substrates by molecular beam epitaxy, *Jpn. J. Appl. Phys.* **45**, p. 8653 (2006).

[83] M. L. L. M. S. de Melo, Deposition of Zn_3N_2 thin films and application in T FT structures, Retrieved from: https://fenix.tecnico.ulisboa.pt/downloadFile/3951455285

99/Resumo%20Alargado.pdf

[84] H. A. Wriedt, The N-Zn (nitrogen-zinc) system, *Bull. Alloy Phase Diag.* **9**, p. 247 (1988).

[85] V. Kambilafka, P. Voulgaropoulou, S. Dounis, E. Iliopoulos, M. Androulidaki, V. Šály, M. Ružinský, and E. Aperathitis, Thermal oxidation of *n*-type ZnN films made by rf-sputtering from a zinc nitride target, and their conversion into *p*-type films, *Superlattices Microstruct.* **42**, p. 55 (2007).

[86] W. Shockley and H. J. Queisser, Detailed balance limit of efficiency of *p-n* junction solar cells, *J. Appl. Phys.* **32**, p. 510 (1961).

[87] L. Han, K. Kash, and H. Zhao, High efficiency green lighte mitting diodes based on InGaN-$ZnGeN_2$ type-II quantum wells, in *Light-Emitting Diodes: Materials, Devices, and Applications for Solid State Lighting XVIII*, Proc. of SPIE Vol. 9003, (Klaus P. Streubel, Heonsu Jeon, Li-Wei Tu, and Martin Strassburg editors), SPIE-Int. Soc. Optical Engineering, Bellingham, WA, p. 90030W–1–5, 2014.

[88] A. Punya, W. R. L. Lambrecht, and M. van Schilfgaarde, Quasiparticle band structure of Zn-IV-N_2 compounds. *Phys. Rev. B* **84**, p. 165204 (2011).

[89] T. Paskova editor, *Nitrides with Nonpolar Surfaces: Growth, Properties, and Devices*, WILEY-VCH Press, Weinheim, 2008.

[90] M. Maunaye and J. Lang, Préparation et Proprietés de $ZnGeN_2$, *Mater. Res. Bull.* **5**, p. 793, (1970).

[91] M. Wintenberger, M. Maunaye, and Y. Laurent, Groupe spatial et ordre des atomes de zinc et de germanium dans $ZnGeN_2$, *Mater. Res. Bull.* **8**, p. 1049 (1973).

[92] T. Endo, Y. Sato, H. Takizawa, and M. Shimada, High Pressure Synthesis of new compounds, $ZnSiN_2$ and $ZnGeN_2$ with distorted wurtzite structure, *J. Mater. Sci. Lett.* **11**, p. 424 (1992).

[93] F. Kawamura, N. Yamada, M . Imai, and T. Taniguchi, Synthesis of $ZnSnN_2$ crystals via a high-pressure metathesis reaction, *Cryst. Res. Technol.* **51**, p. 220 (2016).

[94] P. Narang, (2016) *Light-matter Interactions in Semiconductors and Metals: From Nitride Optoelectronics to Quantum Plasmonics* (Doctoral Dissertation), California. Retrieved from http://thesis.library.caltech.edu/9004/9/PrinehaNarang-Thesis.pdf

[95] T. D. Veal, N. Feldberg, N. F. Quackenbush, W. M. Linhart, D. O. Scanlon, L. F. J. Piper, and S. M. Durbin, Band gap dependence on cation disorder in $ZnSnN_2$ solar absorber, *Anv. Energy Mater.* **5**, p. 1501462 (2015).

[96] A. N. Fioretti, E. S. Toberer, A. Zakutayev, and A. C. Tamboli, Effects of low temperature annealing on the transport properties of zinc tin nitride, *Photovoltaic Specialist Conference (PVSC), IEEE 42nd*, p. 1 (2015).

[97] W. L. Larson, H. P. Maruska, and D. A. Stevenson, Synthesis and properties of $ZnGeN_2$, *J. Electrochem. Soc.* **121**, p. 1673 (1974).

[98] S. Kikkawa, H. Morisaka, RF-sputter deposition of Zn-Ge nitride thin films, *Solid State Commun.* **112**, p. 513 (1999).

[99] P. C. Quayle, K. L. He, J. Shan, and K. Kash, Synthesis, lattice structure, and band gap of $ZnSnN_2$, *MRS Commun.* **3**, p. 135 (2013).

Chapter 3

Intentional Oxygen-Doping into Polycrystalline Zn_3N_2 Thin Films: Preparation, Characterization, and Analysis

The good life is one inspired by love and guided by knowledge.

—Bertrand Russell

3.1 Background and Objective

Compared to the case of ZnO, its isogenous metal nitride (zinc nitride; Zn_3N_2) has as yet garnered much less attention from the standpoints of both fundamental and applied research in materials science. A resurgence of its research has been witnessed over the past two decades, however still remained less "undiscovered" in contrast with its first synthesis in 1940. Such a case belies the fact that numerous pioneering research work on nitride properties was performed in earlier 20^{th}, let alone much unknown so far awaits further exploitation. Accelerated progress is being made for Zn_3N_2 case via investigating its structural, electrical, and optical properties in the terms of Zn_3N_2 powder [1-2], Zn_3N_2 thin film [3-4], Zn_3N_2 nanowires [5-6], or Zn_3N_2 hollow structures [7-8]. However, some major property concerns are still left undecided such as its stern intrinsic synthesis (impurities, in particular oxygen impurities, exist within Zn_3N_2 materials no matter what kinds of deposition techniques is used, even in an ultra-high vacuum MBE system [9]), or the origin

of high electron mobility in thin film. Many reports have merely stated that the oxygen impurity states can be observed not only on the surface but also within their unintentionally-doped Zn_3N_2 film host without any further illustrations.

This *Chapter 3* in our work will perform intentional oxygen-doping into zinc nitride to probe into the oxygen impurity factor and carry out a thorough discussion about the influence of the oxygen impurities on the structural, electrical, and optical properties of zinc nitride thin films.

3.2 Preparation Details for Zinc Nitride Thin Films

3.2.1 Film Deposition Technique

The film deposition technique employed in our work is the reactive radio-frequency magnetron sputtering, which is a well-established and widely-used technique for one of the mainstream industrial deposition ways as well as for research and development [10-20]. The reactive radio-frequency magnetron sputtering is a physical vapor deposition hybrid process of reactive sputtering, radio-frequency sputtering, and magnetron sputtering. The basic process is schematically shown as Figure 3.1.

A target, *i.e.*, a source of the thin film material planed to be deposited, is bombarded with energetic ions, typically inert gas ions such as high purity Argon (Ar^+; as this work used). In reactive sputtering process, we also introduced the sputter reactive gases nitrogen (N_2) and oxygen (O_2) into the sputter vacuum chamber. A "glow discharge" plasma (hot gas-like phase consisting of ions and electrons) thus formed by the passage of electric current through a low-pressure sputter gases. During the sputtering process, generated ions directly affect onto the target and then eject the target atoms into the vacuum chamber space. With the forceful bombardment, in the glow discharge plasma region, these sputtered atoms (though only a small fraction of the ejected atoms are ionized) then can ballistically travel

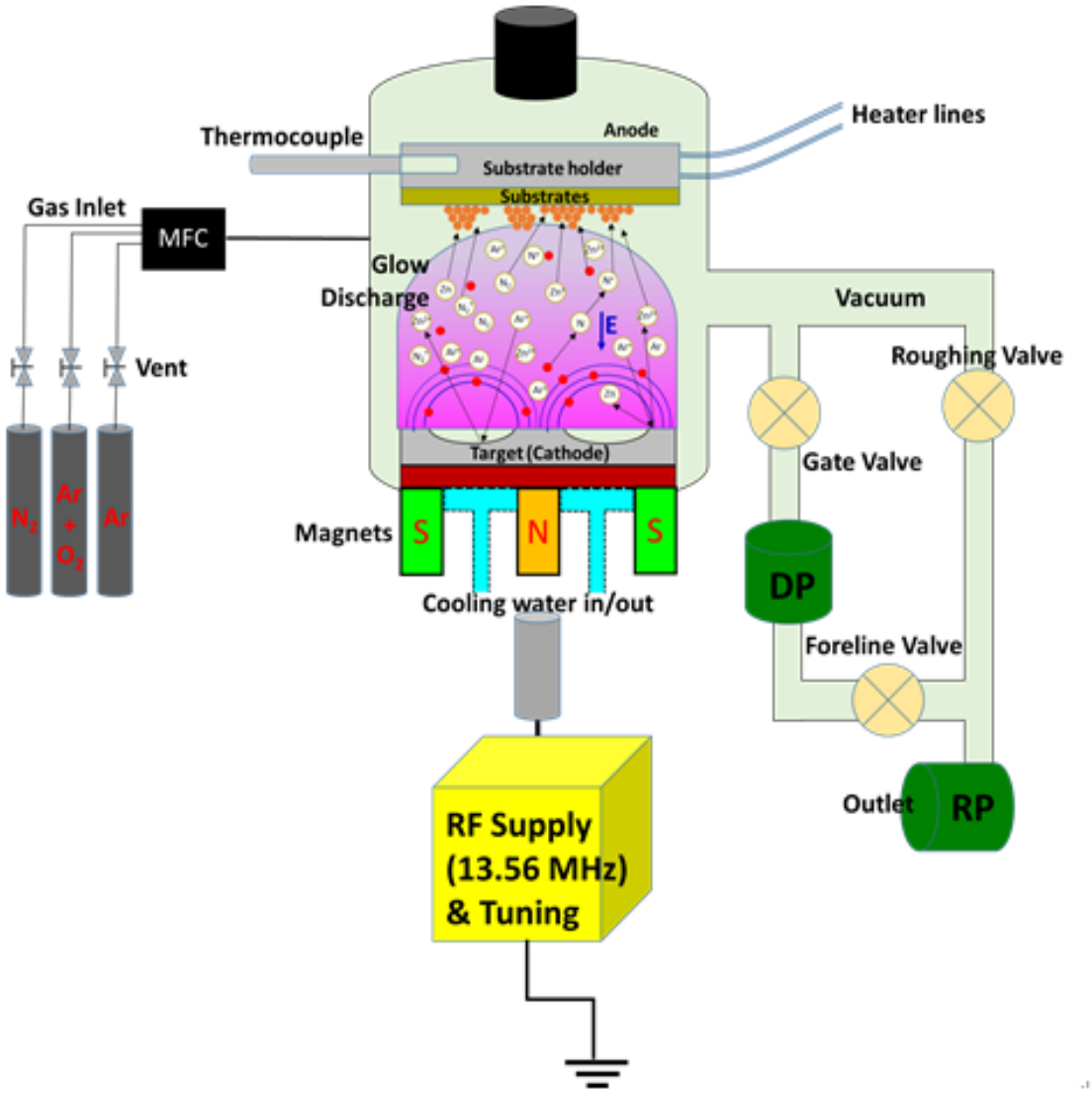

Figure 3.1. A schematic diagram illustrating the reactive radio-frequency magnetron sputtering system employed in our whole experiments. Red circles balls represent the free electron, white circle balls dominate the ions, radicals, neutral particles; while the blue arrow and blue dashed arcs mean the electric field, primary magnetic field, respectively. Ionized argon (Ar^+) are accelerated to "fly" towards to the target and bombard the target atoms to release atoms to react sputter gas form layers atop substrates. Electrons and gas ions form a plasma, which is located near the target due to the magnetic field, resulting in sputter process greater efficiency and quality. A shutter above the target material and the cooling water in/out liquid inlet lines are not shown in this schematic diagram.

everywhere of the space from the target in straight lines; besides, the powerful magnets employed can not only increase the ionization of target atoms and also confine charged plasma particles close to the surface of the sputter target. In a magnetic field, traveling electrons undergo more ionizing collisions and spiral along the magnetic flux lines near the target surface instead of being attracted toward the substrate without causing damages to the thin film being formed. As more and more target material atoms and sputtered reactive gas atoms coalesce atop the substrate, they begin to bind to each other at the molecular level, forming a tightly bound atomic layer. Such a hybrid process can create at will one or more layers of desired thin film by controlling the sputtering time with a considerable deposition rate, enable many kinds of possible spattered materials even including insulating targets, allow various parameters to be controlled to grow thin films with good step coverage and uniformity. The absolute reactive radio-frequency magnetron apparatus used in our whole work is depicted in Figure 3.2.

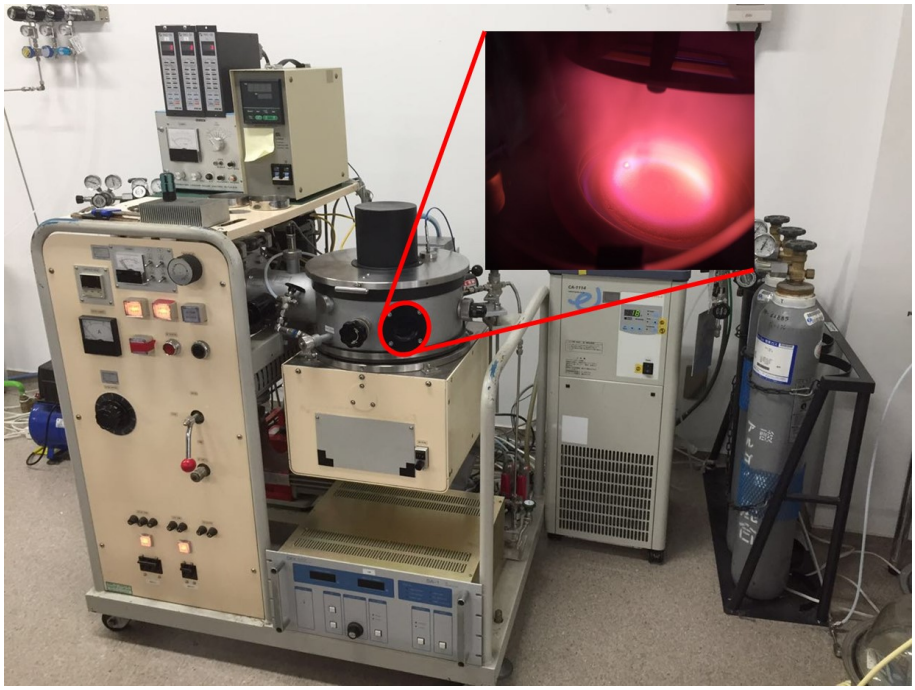

Figure 3.2. An absolute apparatus used for all film deposition in our work. The inset figure shows the plasma plume produced by reactive RF magnetron sputtering of metal target.

3.2.2 Experimental Procedures

Oxygen-doped zinc nitride ($Zn_3N_{2-x}O_x$) thin films were grown on non-alkali glass (Corning Eagle XG) heated at 200 °C by reactive RF magnetron sputtering technique using a disk of metal Zn as a target (Φ100 × 5 mm, purity of 99.9%). The substrates were ultrasonically degreased in methanol for 5 min, and then in acetone for 5 min, and one more time in methanol for 5 min. At last, they were dried with nitrogen gas blowing. A gas mixture consisting of Ar (99.999%), N_2 (99.9995%), and O_2 (99.999%) was introduced into the film-deposition chamber as the sputtering gases, with a constant N_2 / (Ar + N_2+ O_2) flow ratio of 80%, under a working pressure of 2.0 Pa. All of theses sputtering gases were introduced into the chamber by using a mass flow controller (MFC). The substrates were fixed on a sample holder at a distance of 5.50 cm from the surface of target in a sputter-up geometry. To fabricate the $Zn_3N_{2-x}O_x$ films with various x values, sputtering was conducted with various flow ratios of O_2 / (Ar + N_2+ O_2), $f(O_2)$, ranging from 0 to 0.3%. When oxygen was intentionally introduced to the film-growth chamber, deposition rate was decreased from 50 to 40 nm min^{-1} as oxygen partial pressures increased. An RF power of 120 W was applied to the target. Prior to the thin film deposition process, a 5-min-long sputter-etching with pure Ar gas was performed, followed by a 5-min-long pre-sputtering under the same condition with film deposition. The film deposition time was 3 min. The thickness of a typical film was 100−150 nm. To minimize oxidation and/or hydroxylation, all measurements were performed within a day after the deposition.

3.2.3 Main Measurement Methods and Experimental Procedures

3.2.3.1 X-Ray Diffraction (XRD)

X-ray diffraction (XRD) measurements using Cu Kα radiation (λ = 1.5418 Å) were performed in θ–2θ mode to characterize the crystalline phase of the films by using a diffractometer (Rigaku ATX-E). All XRD patterns were recorded in a 2θ range of 20°–65°

with a scan speed of 1.000 °/min. The thing film samples in this whole work were analyzed with this XRD system in terms of their phase determination and orientation relationships between samples and YSZ substrate, employing various measurement techniques, such as out-of-plane and in-plane XRD measurements.

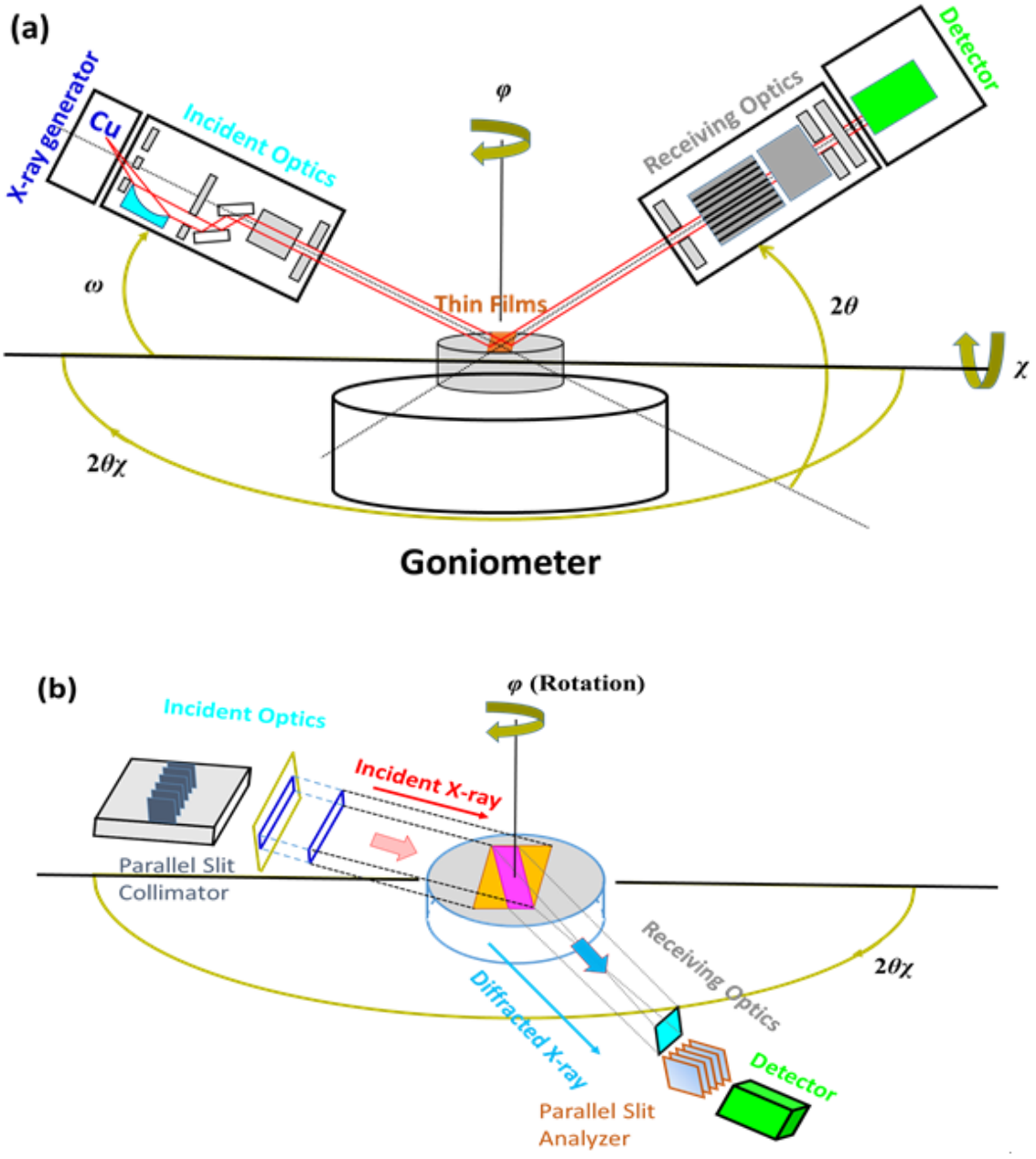

Figure 3.3. (a) Schematic illustrations for goniometer configuration and the out-of-plane diffraction conventional θ–2θ mode. (b) A schematic illustration of goniometer setup and motion for in-plane diffraction $2\theta\chi$-φ–scan mode measurements.

We gave a brief introduction of out-of-plane (see Figure 3.3(a)) and in-plane measurements (see Figure 3.3(b)) of this technique at the beginning of experimental section of whole work, which were shown as above.

3.2.3.2 X-Ray Reflectivity (XRR)

The XRR measurement technique is a non-destructive method which can be used to determine thin-film parameters (thickness, density, and surface roughness) by analyzing X-ray reflection intensity curves originated from grazing incident X-ray beam. The thickness, density, and surface roughness of the films were evaluated by XRR measurements for 2θ ranging from 0 to 1.0° using the same diffractometer with XRD, as illustrated in Figure 3.4. Interference occurs between the X-ray beam reflected from the surface of film and the interface between film and substrate, this X-ray interference can thus bring about oscillations in XRR profiles. These oscillations were called Kiessig fringes which was first observed by Kiessig in 1931. From the calculations of these oscillations, we can get the thin-film thickness, while the amplitude of these oscillations and the critical angle of the total reflection profile can furnish the density and the roughness information we are desired to know.

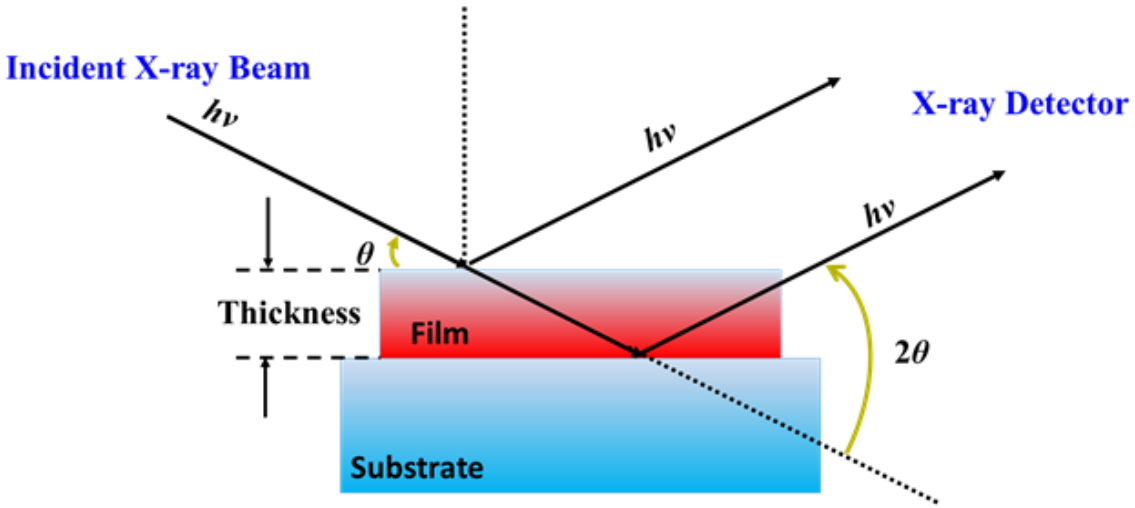

Figure 3.4. A schematic illustration of X-ray reflectivity measurement.

3.2.3.3 Scanning Electron Microscope (SEM)

A scanning electron microscope (SEM; JEOL JSM-6510LA) was employed for surface morphology observations.

3.2.3.4 X-Ray Photoelectron Spectroscopy (XPS)

X-ray photoelectron spectroscopy (XPS) using monochromated Al Kα (hv = 1486.6 eV) radiation was employed (PHI Versa Probe) for examining the chemical state and composition of the films. XPS was performed on both as-deposited and 2 min Ar^+-sputtered-surface films. The latter was carried out by the sputter-etching using an Ar^+-gun with an ion energy of 4 keV and emission current of 7 mA, with a raster size of 3 × 3 mm^2. The semi-quantitative evaluation of XPS signals was done by an XPS peak fitting program, namely, XPSPEAK 4.1 software. The Shirley algorithm [21], the most widely used background subtraction method, was chosen for the background subtraction before entering the fit iterations. The peak shapes were typically determined by using Gaussian-Lorentzian sum function, and a linear least squares curve fitting procedure was adopted to fit the spectra. Electrical resistivity (ρ) of films was measured using the van der Pauw method with a source current of 1 mA. Carrier density (n_e) and Hall mobility (μ_H) were determined by Hall effect measurement in the van der Pauw configuration (Toyo Corp. Resitest 8200): the magnetic fields of ±1 T were applied normal to the film surface. For selected samples, temperature dependence of ρ, n_e, and μ_H were also measured, for temperatures ranging from 77 to 350 K. Optical transmittance and reflectance measurements in the ultraviolet-visible region were performed by using a spectrophotometer.

3. 3 Results and Discussions

3.3.1 Structural Properties

θ–2θ XRD patterns of as-deposited films fabricated at $f(O_2)$ = 0.0–0.3% are shown in Figure 3.3(a). This figure shows that all as-deposited films were in polycrystalline form. All diffraction peaks corresponded to those from Zn_3N_2 (ICDD card No. 35-0762). No ZnO peaks were detected even at $f(O_2)$ > 0%. That is, polycrystalline films of phase-pure $Zn_3N_{2-x}O_x$ with cubic anti-bixbyite structure were obtained under the deposition condition of $f(O_2)$ = 0.0–0.3%. While the 400 peak was most prominent for the $f(O_2)$ = 0% film, the 222 peaks were most dominant for the $f(O_2)$ > 0% ones. In addition, film crystallinity seemed to be slightly improved by introducing oxygen gas during the deposition. These phenomena remain unexplained, and further studies are required to understand the underlying mechanism.

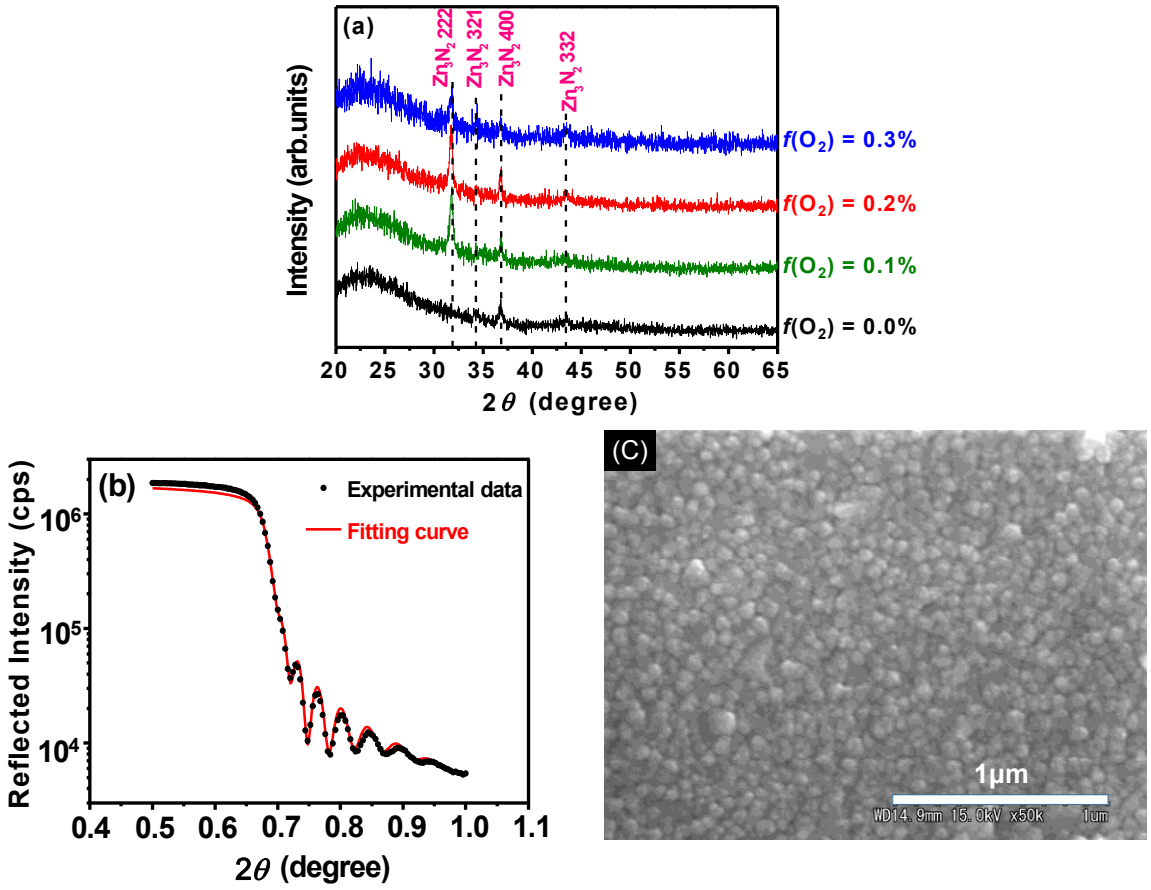

Figure 3.5. (a) XRD patterns for oxygen-doped Zn_3N_2 films fabricated at $f(O_2)$ = 0.0–0.3%, (b) XRR spectrum for a film deposited at $f(O_2)$ = 0.2%, and (c) a typical top-view SEM image at ×50,000 magnification for Zn_3N_2 films.

Figure 3.5(b) shows the XRR spectrum for the 115 nm thick $f(O_2)$ = 0.2% film. We fitted the XRR spectrum to obtain the density and surface roughness of the film. For the fit, we assumed film homogeneity along the thickness direction. Surface and/or interface layers were not taken into account (one-layer model). The best fit was obtained when the density and surface roughness were 6.2 g cm^{-3} and 5.0 nm, respectively, as shown in Figure 3.5(b). The good fit implied that inhomogeneity in the thickness direction and the existence of surface/interface layer could be ignored. The obtained density value indicated that the film was a highly dense polycrystalline film, because the theoretical value of Zn_3N_2 is 6.37 g cm^{-3}. The relative density was estimated to be above 90%. Similar density and surface roughness values were obtained for other films.

A typical top-view SEM image at ×50,000 magnification for a Zn_3N_2 film is presented in Figure 3.5(c). The film was composed of grains with diameters of approximately 100 nm.

The grains were densely and uniformly packed together. The dense and relatively smooth structure was consistent with the density and surface roughness values deduced from the XRR analysis. From the SEM observation and XRR analysis, we confirmed that the polycrystalline films deposited in this study were dense and smooth enough to be subject to electrical and optical measurements.

3.3.2 Chemical State and Composition

XPS analyses were performed to determine the chemical states of Zn, N, and O, and semi-quantitative analysis of the composition. Herein, we present spectra for the films deposited at $f(O_2)$ = 0 and 0.2%.

We used Zn Auger $L_3M_{4,5}M_{4,5}$ lines to analyze the chemical state of Zn, because the Auger line is more sensitive to the chemical state than Zn 2p core lines. Figure 3.6(a) shows X-ray excited $L_3M_{4,5}M_{4,5}$ Auger spectra of Zn for the $f(O_2)$ = 0.2% film. Peaks attributed to Zn–OH (kinetic energy, *KE* = 986.8 eV [22]), Zn–O (*KE* = 987.8 eV [22]), and Zn–N (*KE*

= 990.0 eV [22]) bonds were mainly observed on the as-deposited surface. The peak

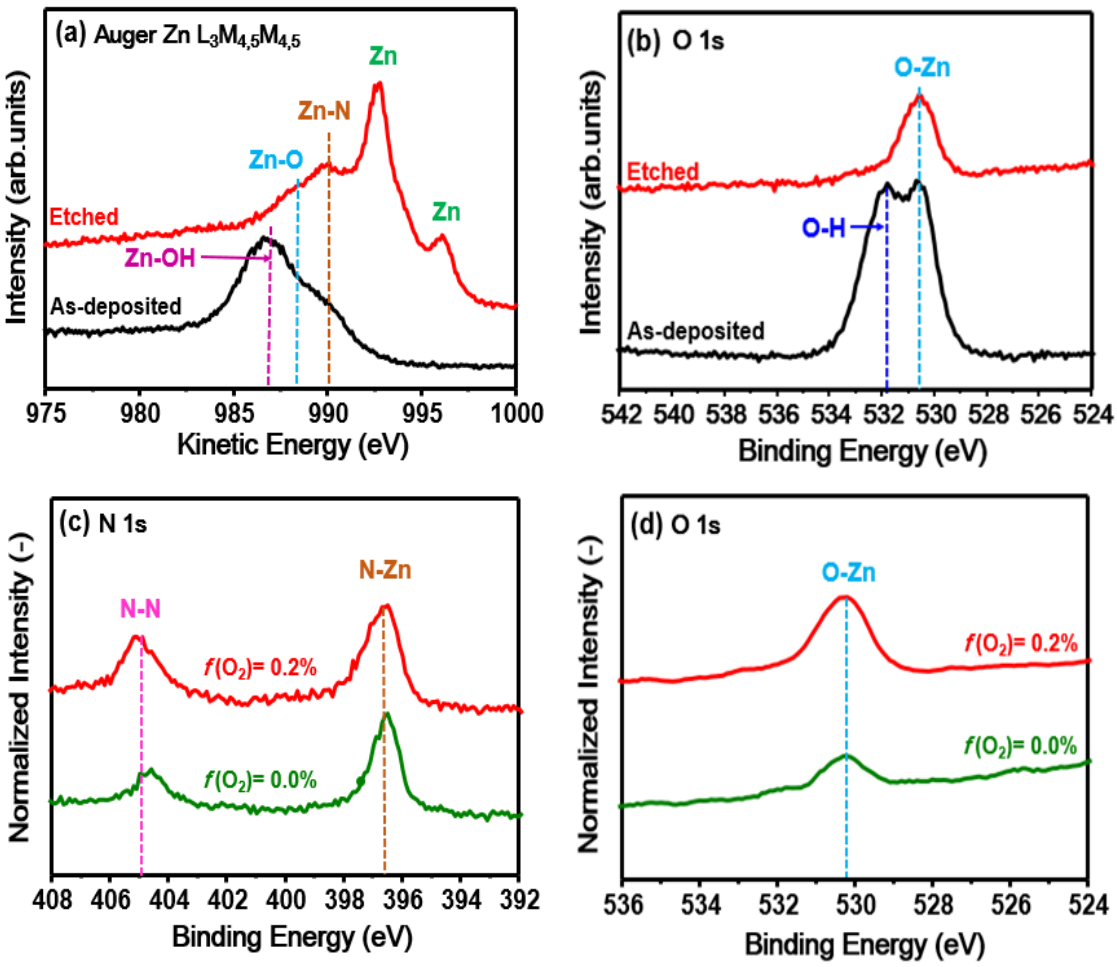

Figure 3.6. (a) X-ray excited $L_3M_{4,5}M_{4,5}$ Auger spectra and (b) O 1s XPS core spectra from as-deposited and sputter-etched surface of a Zn_3N_2 film deposited at $f(O_2)$ = 0.2%. (c) N 1s and (d) O 1s XPS core spectra from sputter-etched surfaces of Zn_3N_2 films deposited at $f(O_2)$ = 0 and 0.2%.

intensity of the Zn-OH signal was much stronger than that of Zn–O and Zn–N signals, suggesting that the surface mainly consisted of $Zn(OH)_2$. Similar results were obtained for the other films deposited under different conditions (see Figure 3.7). These results are consistent with the ones that were reported previously [22]. The existence of OH–Zn and O–Zn bonds on the as-deposited surface was also observed in O 1s spectrum (OH–Zn: binding energy, *BE* = 532.0 eV , [23-24] O–Zn: BE = 530.4 eV [23-24]), shown in Figure

3.6(b). Formations of $Zn(OH)_2$ may be caused by air humidity when the film is exposed to the air. The thickness of the surface $Zn(OH)_2$ layer was expected to be only a few nanometers because a good fit of the XRR spectrum was obtained by using the uniform one-layer model [Figure 3.5(b)]. If the surface layer was thicker than a few nanometers, the good fit could not be obtained. After 2-min-long sputtering (etching rate: ~10 nm/min), the OH–Zn peak in the O 1s spectrum disappeared, indicating that the $Zn(OH)_2$ surface layer was removed. On the other hand, the O–Zn peak was still seen after the etching as shown in Figure 2(b). We obtained similar results for the other films deposited under different conditions. We confirmed that the O–Zn bonds uniformly existed along the film thickness direction by using depth profiling of O 1s peak (see Figure 3.8). This result indicated that the Zn_3N_2 film was doped with oxygen.

Although the 2-min-long sputter-etching partially decomposed Zn_3N_2 into metal Zn [Figure 3.6(a)], the peaks attributed to the N–Zn bonds (*BE* = 396.2 eV [23-24]) were clearly observed in N 1s core spectra [Figure 3.6(c)]. In addition, small peaks in the vicinity of *BE* = 405 eV were observed. The small peak was observed for all films in this study [see Figure 3.7(b)]. The 405 eV peak has been observed recently [24-25]. It was attributed to the N–N bond in molecular nitrogen on nitrogen sites in Zn_3N_2 [denoted as $(N_2)_N$] because the peak position was very similar to that of the N–N bond in molecular nitrogen on oxygen sites in nitrogen-doped ZnO [denoted as $(N_2)_O$] [25]. Although the details have not been clarified yet, we postulate that $(N_2)_N$ consists of a lattice nitrogen (N_N) and a self-interstitial nitrogen (N_I), *i.e.*, N_N–N_I bond, for the following reasons. Theoretical studies showed that the formation energy of N_I is small, suggesting that the existence of N_I in Zn_3N_2 is quite possible [26-27]. In addition, the N_I formation energy was shown

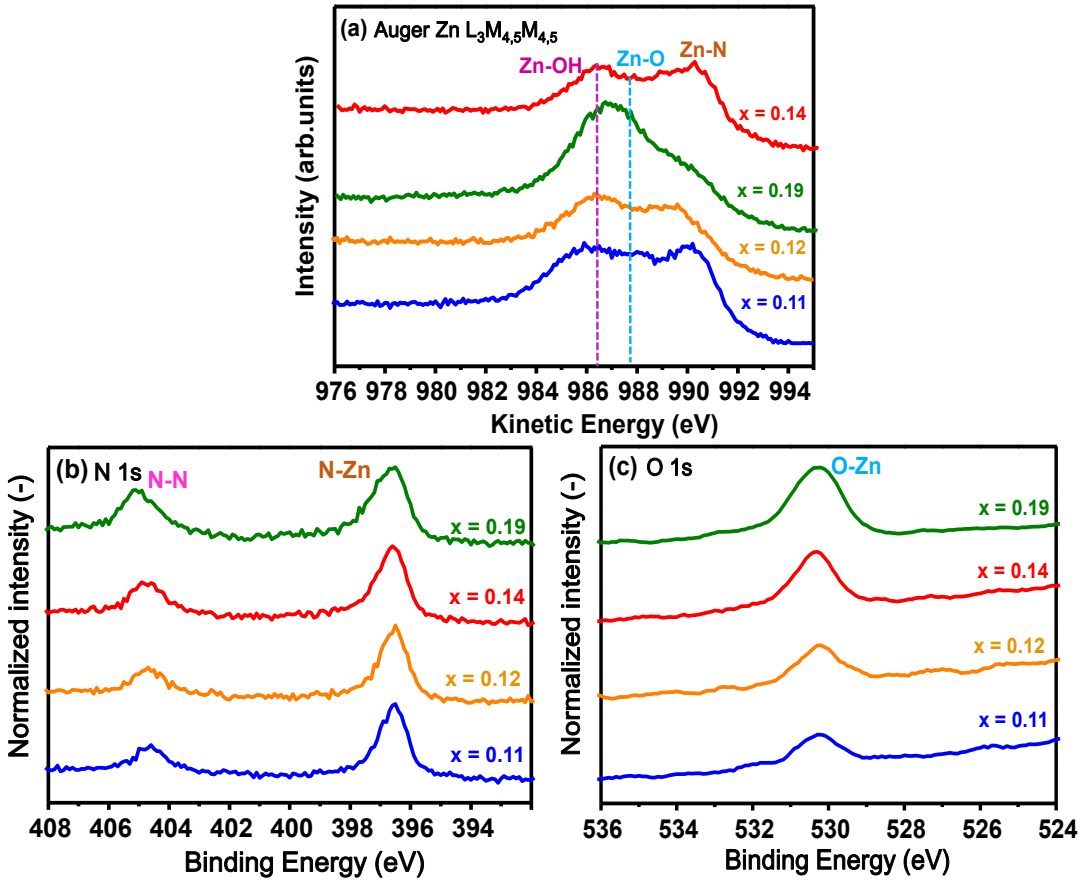

Figure 3.7. (a) X-ray excited $L_3M_{4,5}M_{4,5}$ Auger spectra of Zn on as-deposited surfaces of $Zn_3N_{2-x}O_x$ films. (b) N 1s and (c) O1s XPS core spectra of sputter-etched surfaces of $Zn_3N_{2-x}O_x$ films. The peak intensities of O 1s peaks are normalized by the peak intensities of N 1s peaks located in the vicinity of *BE* = 396 eV (N-Zn bond).

to become smaller when Zn_3N_2 was fabricated in N-rich condition [27]. Since the $Zn_3N_{2-x}O_x$ films in this study were grown at the $f(N_2)$ value as high as 80% (*i.e.*, in N-rich condition), it is quite possible that the films included a certain amount of N_I. Furthermore, N_I was shown to form a chemical bond with nearest neighbor N_N [26]. As we discuss later, the existence of N_I can consistently explain the electrical and optical properties of oxygen-doped Zn_3N_2 films obtained in the present study.

O 1s spectra of sputter-etched (2 min) surfaces for Zn_3N_2 films deposited at $f(O_2)$ = 0 and 0.2% are shown in Figure 3.6(d). In this figure, the spectra are normalized by the peak

intensities of N–Zn peaks in the N 1s spectra. It is noteworthy that O–Zn bond is observed inside the $f(O_2)$ = 0% film. This clearly indicates that non-intentional oxygen doping occurred even at $f(O_2)$ = 0%, which is consistent with previous reports [9, 23-24, 28-29]. The O–Zn peak intensities for intentionally doped films deposited at $f(O_2)$ > 0% were higher than that for the non-intentionally doped one [Figure 3.6(d), also see Figure 3.7(c)], implying increased oxygen content.

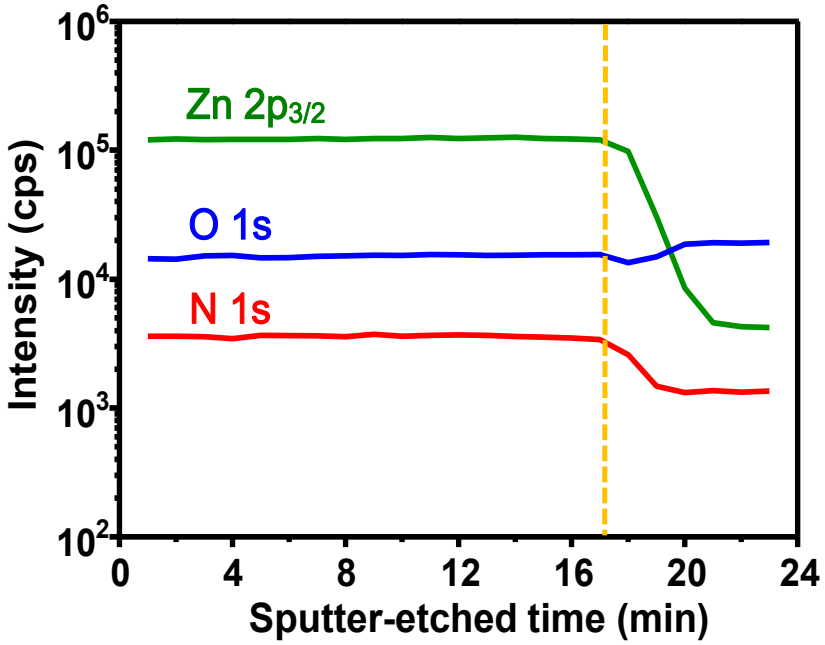

Figure 3.8. XPS depth profiles of Zn $2p_{3/2}$ (*BE* ~ 1022 eV), O 1s (*BE* ~ 530 eV), and N 1s (*BE* ~ 396 eV) signals. The *dashed line* roughly demarcates the film/substrate interface. The peak intensities were obtained without subtracting the background levels. Thus, the peak intensity of the O 1s peak is higher than that of the N 1s peak (the background levels in the O 1s spectra are always higher than those in the N 1s spectra). The etching rate was ~10 nm/min.

Assuming that the etching rate of oxygen is the same as that of nitrogen, we performed semi-quantitative analysis of x in $Zn_3N_{2-x}O_x$ films employing the relative sensitivity factor method and using the integral intensities of O–Zn peak in O 1s spectra and N–Zn peak in

N 1s spectra that were obtained from the surfaces sputter-etched for 2 min. The ratio of the integral intensities of the O–Zn [I(O)] and N–Zn [I(N)] peaks is related to the atomic density ratio (X_O/X_N) by

$$\frac{X_O}{X_N} = \frac{I(O)/S_O}{I(N)/S_N} \tag{3.1}$$

where S_O and S_N are the relative sensitivity factors determined for the pure chemical elements for the specific electron analyzer used. We used S_O = 0.711 and S_N = 0.477 as provided by PHI [30]. Finally, x values in $Zn_3N_{2-x}Ox$ were calculated from the relationship of $x = 2(1 + X_N/X_O)^{-1}$. Figure 3.9(a) shows the dependence of x on $f(O_2)$ in $Zn_3N_{2-x}O_x$. An increase in $f(O_2)$ from 0 to 0.2% caused an increase in x from 0.11 to 0.19. Contrary to our expectation, x decreased slightly when $f(O_2)$ surpassed 0.2%. This slight decrease in x might be caused by a fluctuation in $f(O_2)$ due to the control accuracy of our mass flow controllers.

Table 3.1. Oxygen doping concentration x, lattice length, and carrier density of $Zn_3N_{2-x}O_x$ films.

sample	x in $Zn_3N_{2-x}O_x$	lattice length (nm)	carrier density n_e (cm^{-3})
#1	0.11	0.9784	3.4×10^{19}
#2	0.12	0.9780	4.3×10^{19}
#3	0.14	0.9771	6.3×10^{19}
#4	0.19	0.9764	1.2×10^{20}

The four $Zn_3N_{2-x}O_x$ films were labeled as #1–#4 in the order of increasing x, and are listed in Table 3.1. This table also includes the values of lattice length calculated from the XRD patterns and carrier densities determined by Hall effect measurements. As seen from Table

3.1, the lattice length and carrier density are closely related to semi-quantitative *x*. The lattice length decreased as *x* increased, as shown in Figure 3.9(b). This clearly indicates the

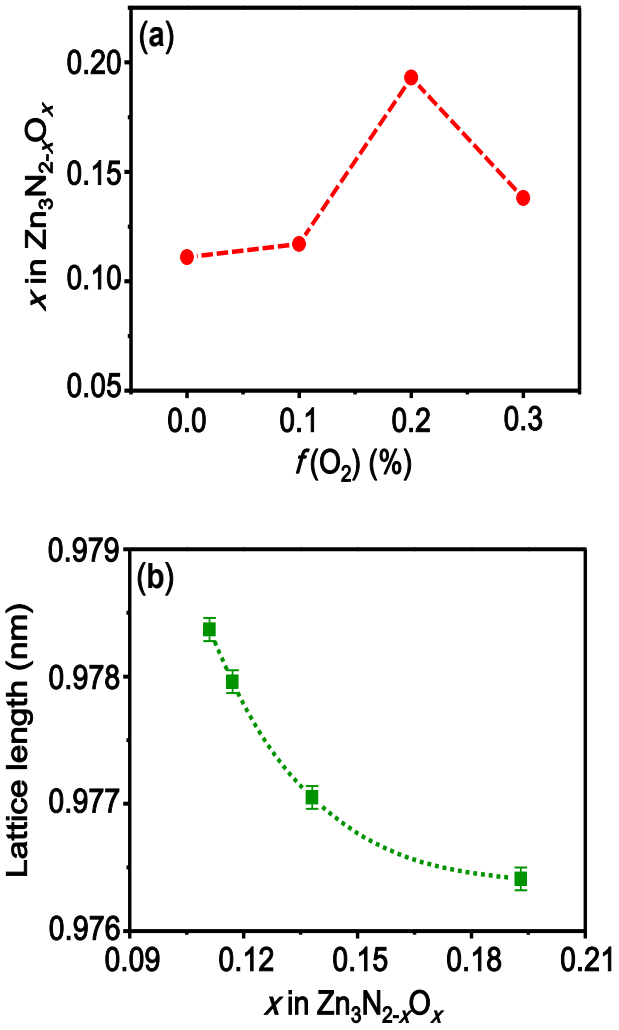

Figure 3.9. (a) Dependence of *x* in $Zn_3N_{2-x}O_x$ on $f(O_2)$ during film deposition. (b) Lattice length vs. *x*, for $Zn_3N_{2-x}O_x$ films. The *x* values were estimated from the integrated intensity ratio of O 1s and N 1s XPS spectra using the RSF method.

replacement of nitrogen in Zn_3N_2 by oxygen, because the ionic radius of O^{2-} is smaller than that of N^{3-} (O^{2-}: 138 pm, N^{3-}: 146 pm [31]). Furthermore, carrier density increased with increasing *x* (*i.e.*, the increase in the substitution fraction of oxygen), implying increasing electron donor density. In the next subsection, we discuss the dependence of electrical properties of $Zn_3N_{2-x}O_x$ films on *x*.

3.3.3 Electrical Properties

Figure 3.10(a) shows room temperature (RT) resistivity ρ as a function of x in $Zn_3N_{2-x}O_x$. As seen from this figure, ρ decreases with increasing x. The minimal ρ of 6.2×10^{-4} Ω cm was obtained for $x = 0.19$. We successfully obtained highly conducting $Zn_3N_{2-x}O_x$ films exhibiting ρ on the order of 10^{-4} Ω cm. To check the reproducibility of our results, the $Zn_3N_{2-x}O_x$ films deposition experiment was repeated three times, under identical conditions. As a result, ρ values of $(5.7 \pm 0.9)\times10^{-4}$ Ω cm were obtained, indicating good reproducibility. The ρ values obtained here are comparable to those of SnO_2- and ZnO-based TCOs. The ρ values achieved in the present work are the smallest among the values achieved so far. Hence, we conclude that intentional oxygen doping is an effective method for reducing ρ in Zn_3N_2 films. From the viewpoint of electrical conductivity, $Zn_3N_{2-x}O_x$ can be regarded as a candidate nitride-based transparent conductor.

Hall coefficients for $Zn_3N_{2-x}O_x$ films were always negative, indicating that the majority carrier was electron (*i.e.*, *n*-type). The decreasing trend of ρ with increasing x reflected increasing carrier density n_e. As shown in Figure 3.10(b), n_e gradually increased with increasing x, suggesting that substitutional oxygen (O_N) released an electron. This can be written using the Köger–Vink notation as $O_N^{x} \rightarrow O_N^{\cdot} + e'$. The n_e attained the maximum of 1.2×10^{20} cm^{-3} at $x = 0.19$, whereas ρ reached the minimum of 6.2×10^{-4} Ω cm. These results clearly indicate that oxygen in $Zn_3N_{2-x}O_x$ films effectively acts as an electron donor, which agrees with the theoretical prediction [32]. Nevertheless, the ionization efficiency of oxygen was very low and was estimated to be only 2–4%. The origin of this low ionization efficiency remains elusive. One possible explanation is that an in-gap state is created by N_I captures of electrons generated from O_N^{x}: Long *et al*. showed that N_I introduces a half-filled N 2p state in the bandgap [26] and such half-filled in-gap state usually acts as an electron trap. Nevertheless, additional studies are still needed to understand this low

ionization efficiency.

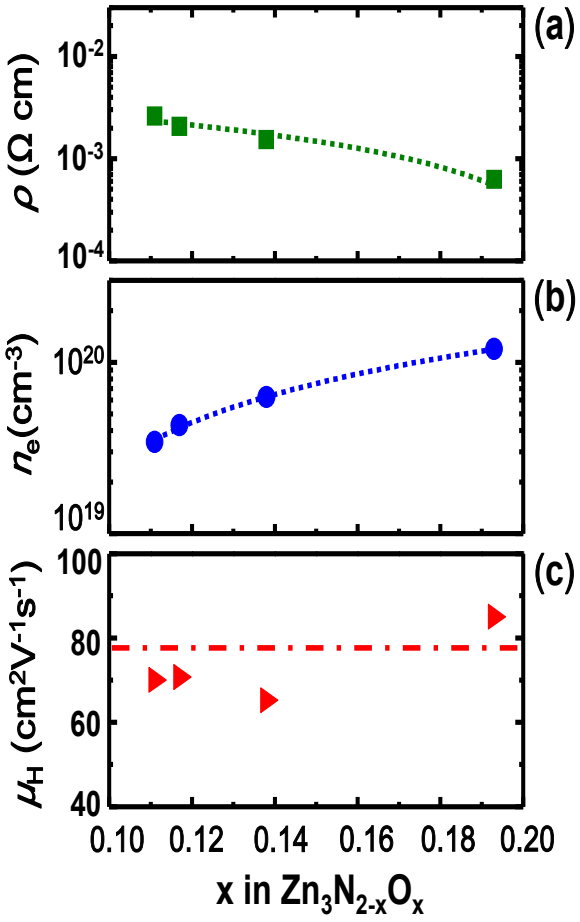

Figure 3.10. (a) Resistivity ρ, (b) carrier density n_e, and (c) Hall mobility μ_H as functions of x in $Zn_3N_{2-x}O_x$ films, at room temperature.

Meanwhile, as shown in Figure 3.10(c), μ_H did not exhibit clear x dependence. It should be noted that $Zn_3N_{2-x}O_x$ films have large μ_H, even in polycrystalline form. In most cases, μ_H values were above 70 $cm^2\,V^{-1}\,s^{-1}$. The highest value of 85 $cm^2\,V^{-1}\,s^{-1}$ was obtained for x = 0.19. The highest value is 100-fold higher than those measured in degenerately doped GaN polycrystalline films (μ_H < 1 $cm^2\,V^{-1}\,s^{-1}$) [33], and approximately 2-fold higher than those measured in conventional TCOs such as In_2O_3, ZnO, and SnO_2 polycrystalline thin films (μ_H = 20–40 $cm^2\,V^{-1}\,s^{-1}$) [34]. Because the electron effective mass ($m_e^* \sim 0.3m_0$) in Zn_3N_2 is similar to those in conventional TCOs and GaN, the electron scattering time (τ) in $Zn_3N_{2-x}O_x$ is thought to be larger than τ values in those semiconductors. Therefore,

$Zn_3N_{2-x}O_x$ can be regarded as a high-mobility semiconductor.

Temperature (T) dependence of ρ, n_e, and μ_H for $Zn_3N_{2-x}O_x$ films with x = 0.11 and 0.19 is shown in Figure 3.11(a)–(c), respectively. The ρ–T curves exhibit nearly temperature-independent behavior. These curves have very small positive temperature coefficient, suggesting metallic conductivity in $Zn_3N_{2-x}O_x$ films. Conduction electrons in the films could be regarded as highly degenerate electron gas, because n_e values are independent of temperature, as shown in Figure 3.11(b). Similar to n_e, the μ_H was nearly constant for temperatures ranging from 77 to 350 K [Figure 3.11(c)]. The μ_H–T behavior suggests that ionized impurity scattering mainly governs electron transport in $Zn_3N_{2-x}O_x$, because electron mobility limited by the ionized impurity scattering does not depend on temperature in degenerate semiconductors [35].

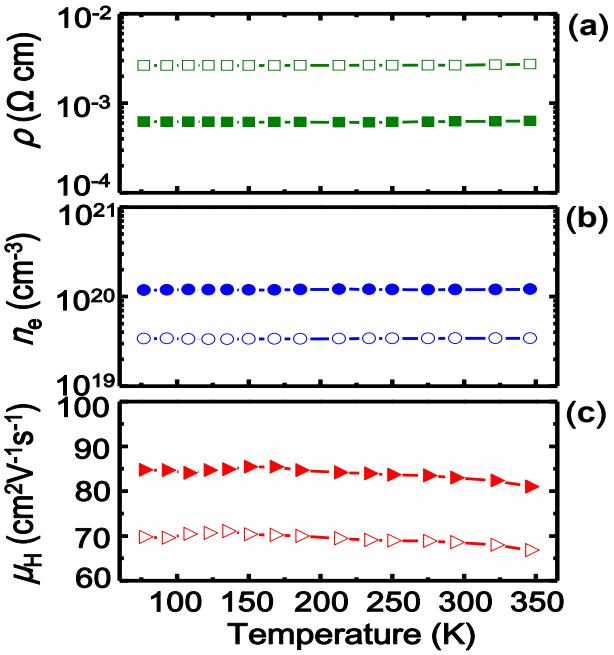

Figure 3.11. Temperature dependence of (a) resistivity ρ, (b) carrier density n_e, and (c) Hall mobility μ_H for $Zn_3N_{2-x}O_x$ films with x = 0.11 (open symbols) and x = 0.19 (closed symbols).

To get insight into the electron transport in polycrystalline $Zn_3N_{2-x}O_x$ films, we compared experimental μ_H values with theoretical mobility limited by the ionized impurity scattering

(μ_I). The theoretical μ_I values were calculated by using the Books–Herring–Dingle formula [35],

$$\mu_I = \frac{24\pi^3(\varepsilon_0\varepsilon_r)^2\hbar^3}{e^3 m_e^{*2}} \frac{1}{g(\zeta)} \cdot \frac{n_e}{Z^2 n_I} \tag{3.2}$$

where the screening function $g(\zeta)$ is given by

$$g(\zeta) = \ln\left(1+\frac{4}{\zeta}\right) - \left(1+\frac{\zeta}{4}\right)^{-1} \tag{3.3}$$

and

$$\zeta = \frac{e^2 m_e^*}{\pi\varepsilon_0\varepsilon_r\hbar^2(3\pi^5 n_e)^{\frac{1}{3}}} \tag{3.4}$$

Here, ε_0 and ε_r are the static dielectric constants of free space and the material, respectively. Z is the relative charge of the ionized impurity, n_I is the density of the ionized scattering center, e is the elemental charge, and $\hbar$ is the reduced Planck constant. We used $\varepsilon_r = 5.3$ [36] and $m_e^* = 0.3m_0$ [9, 37] for the calculation of μ_I. We calculated μ_I for two cases: in the first case, free carriers are generated entirely from substitutional oxygen $O_N^{\cdot}$ (μ_I^o), and in the second case, free carriers originate entirely from nitrogen vacancy (μ_I^v). Based on the first-principles calculation, the nitrogen vacancy was predicted to have low formation energy and to behave as an electron donor [21, 26]. In addition, in our experimental study we found that in nitrogen-deficient $Zn_3N_{2-\delta}$ films n_e values were above 10^{18} cm^{-3} [37]. Thus, the nitrogen vacancy as an ionized impurity scattering center was taken into account as well. In the case of $O_N^{\cdot}$, $n_e/(Z^2 n_I)$ in Eq. (3.2) was set to 1 because the following relations, $n_e = n_I$ and $Z = 1$, hold. For the nitrogen vacancy case, we assumed that one vacancy releases three electrons: this can be written using the Köger–Vink notation as $V_N \rightarrow V_N^{\cdots} + 3e'$. Hence, $n_e/(Z^2 n_I)$ value in Eq. (3.2) was set to 1/3 assuming the relationships of $n_e = 3n_I$ and $Z = 3$.

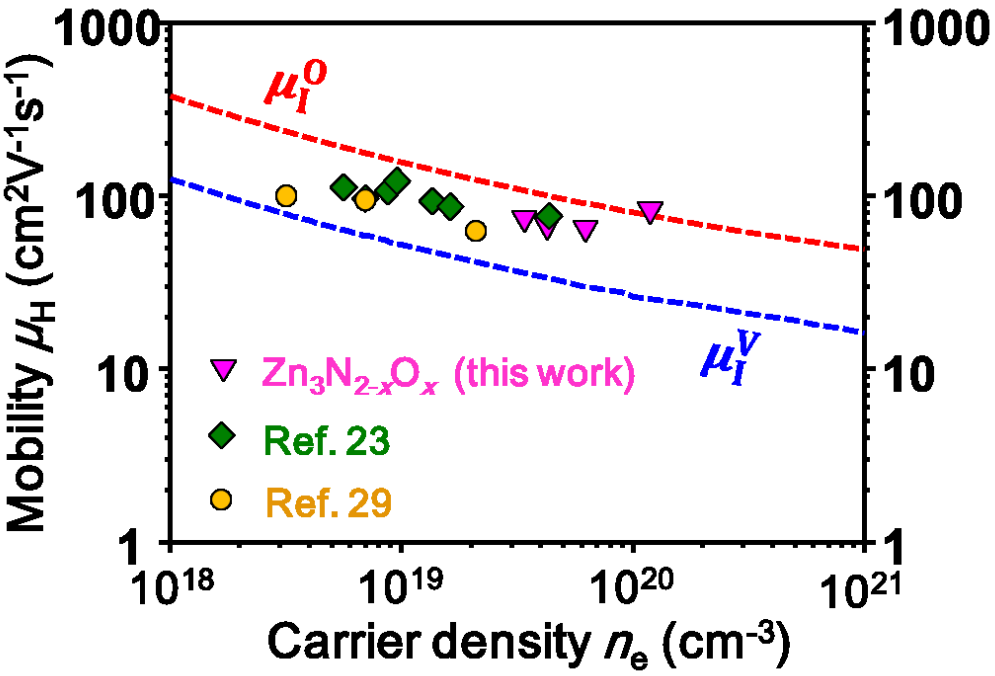

Figure 3.12. Plots of μ_H values (closed triangles) as a function of carrier density n_e. The μ_I^O and μ_I^V curves are the theoretical electron mobility due to ionized impurities, assuming that the free carriers originate entirely from singly charged $O_N^{\cdot}$ and triply charged $V_N^{\cdots}$, respectively. Literature values for non-intentionally doped $Zn_3N_{2-x}O_x$ are also shown as closed diamonds (Ref. 3) and closed circles (Ref. 9).

In Figure 3.12, the RT values of μ_H are plotted along with theoretical curves as functions of n_e. Literature values [23, 29] for non-intentionally doped $Zn_3N_{2-x}O_x$ polycrystalline films having n_e on the order of 10^{18}–10^{19} cm^{-3} were also included in this figure. As seen from this figure, all experimental μ_H values are located between μ_I^V and μ_I^O curves. The μ_H values are always above the μ_I^V curve, suggesting that the dominant ionized impurity scattering center in $Zn_3N_{2-x}O_x$ is the substitutional oxygen $O_N^{\cdot}$ rather than the nitrogen vacancy $V_N^{\cdots}$. Furthermore, the μ_H values obtained in this study are close to the μ_I^O curve. This led us to conclude that the contributions of additional scattering mechanisms, such as phonon, neutral impurity, and grain boundary scattering are very minor in electron mobility of heavily doped $Zn_3N_{2-x}O_x$ at RT.

3.3.4 Optical Properties

Optical transmittance (T_{opt}) spectra for $Zn_3N_{2-x}O_x$ films with x = 0.11 (n_e = 3.4×10^{19} cm^{-3}), x = 0.14 (n_e = 6.3×10^{19} cm^{-3}), and x = 0.19 (n_e = 1.2×10^{20} cm^{-3}) are shown in Figure 3.13(a). For comparison, this figure also includes transmittance spectra of a Zn_3N_2 film (thickness of 300 nm) reported by Kuriyama *et al*. [38]. The presently obtained films exhibited transmittance below 40% in the visible region. In our films, transmittance values were substantially lower than the previously reported transmittance throughout the spectrum of wavelengths, although our films were thinner than 300 nm. In what follows, we explain the lower transmittance obtained in the present study.

It is likely that the low transmittance in the visible region is attributed to the formation of N_I, for the following reasons. As discussed in Sec. 3.3.2, $Zn_3N_{2-x}O_x$ films in this study probably contained a certain amount of N_I. Formation of N_I introduces a half-filled N 2p state in the bandgap [26], so that optical absorption by electron transition between the interstitial N 2p in-gap state and the conduction/valence band state (defect-to-band transition) occurs. Therefore, we infer that the visible light absorption by the defect-to-band transition is responsible for the low optical transmittance reported in Figure 3.13(a). The defect-to-band transition would relate to broad blue light (2.3–2.9 eV) emissions along with UV emission reported in photoluminescence studies [5, 39]. To establish $Zn_3N_{2-x}O_x$ as a transparent conductor, one has to address the issue of reduction in N_I density. Since the N_I formation energy increases when Zn_3N_2 is fabricated in N-poor condition, nitrogen partial pressure or nitrogen activity during the film growth is a key to the N_I density reduction. Efforts aimed at optimizing nitrogen partial pressure or nitrogen activity during the growth would allow us to achieve truly transparent conducting $Zn_3N_{2-x}O_x$ films.

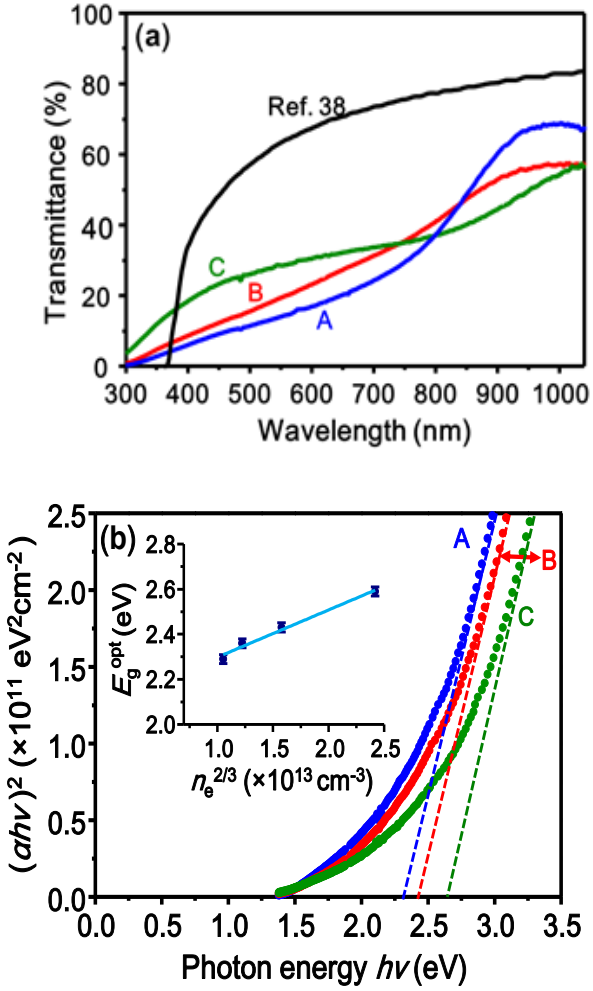

Figure 3.13. (a) Optical transmittance spectra for $Zn_3N_{2-x}O_x$ films with different x values. The reported spectrum taken from Ref. [38] is also shown in this figure. (b) hv versus $(\alpha hv)^2$ plots for $Zn_3N_{2-x}O_x$ films with different x values. The curves A, B, and C are for $Zn_3N_{2-x}O_x$ films with x = 0.11 (n_e =3.4×10^{19} cm^{-3}), 0.14 (n_e =6.3×10^{19} cm^{-3}), and 0.19 (n_e =1.2×10^{20} cm^{-3}), respectively. The inset of (b) represents $n_e^{2/3}$ dependence of E_g^{opt}.

To investigate the effect of n_e on the bandgap energy, we evaluated the optical gap (E_g^{opt}) in our films. Because Zn_3N_2 has been reported to be a direct gap semiconductor [5, 9, 38-40, 23-24, 28-29], we estimated E_g^{opt} values using the well-established relation $\alpha hv = A(hv - E_g)^{1/2}$, where α is the absorption coefficient, A is a constant, and hv is the photon energy. α values were calculated using transmittance (T_{opt}) and reflectance (R_{opt}) spectra using the equation $\alpha = d^{-1}\ln[(1-R_{opt})/T_{opt}]$, where d is the film thickness (R_{opt} spectra are shown in Figure 3.14). Figure 3.13(b) shows the plots of $(\alpha hv)^2$ versus hv for $Zn_3N_{2-x}O_x$ films with x

= 0.11, 0.14, and 0.19. We determined the E_g^{opt} values by extrapolating the linear portions to $(\alpha h\nu)^2 = 0$. E_g^{opt} was 2.3 eV for the $x = 0.11$ film, 2.5 eV for the $x = 0.14$ film, and 2.6 eV for the $x = 0.19$ film. That is, E_g^{opt} exhibited a blue shift as n_e increased (also see Figure 3.15e). As seen from the inset of Figure 3.13(b), the blue shift was linearly related to $n_e^{2/3}$. This behavior can be explained by the Burstein-Moss (B-M) effect [41] in which E_g^{opt} increases proportionally to $n_e^{2/3}$ in a degenerate semiconductor having a parabolic conduction and valence band. The observation of the B-M shift strongly supports the notion that $Zn_3N_{2-x}O_x$ films are degenerate semiconductors, as discussed in Sec. 3.3.3.

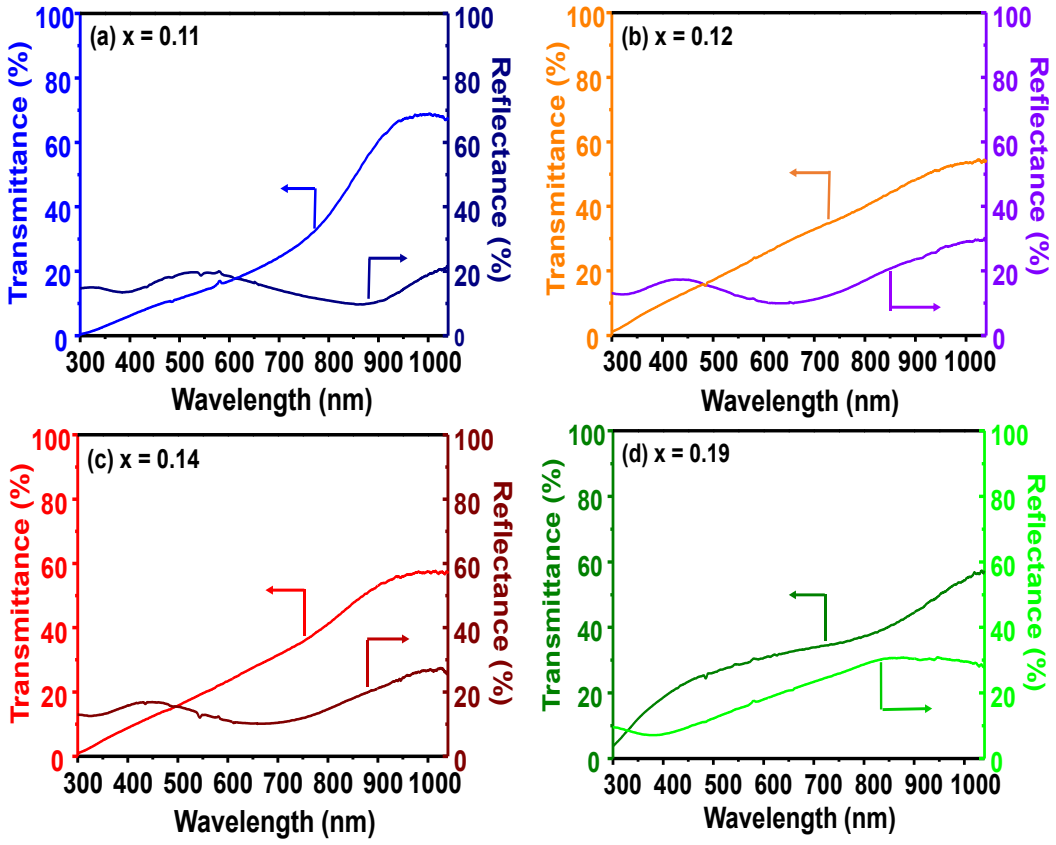

Figure 3.14. Optical transmittance and reflectance spectra for $Zn_3N_{2-x}O_x$ films with (a) $x = 0.11$, (b) $x = 0.12$, (c) $x = 0.14$, and (d) $x = 0.19$.

The E_g^{opt} values obtained in this study were somewhat smaller than the reported E_g^{opt} value of 3.2 eV [5, 38-40]. We speculate that the E_g^{opt} values were underestimated owing to the

contribution of defect-to-band transition. The visible–ultraviolet absorption in the presently

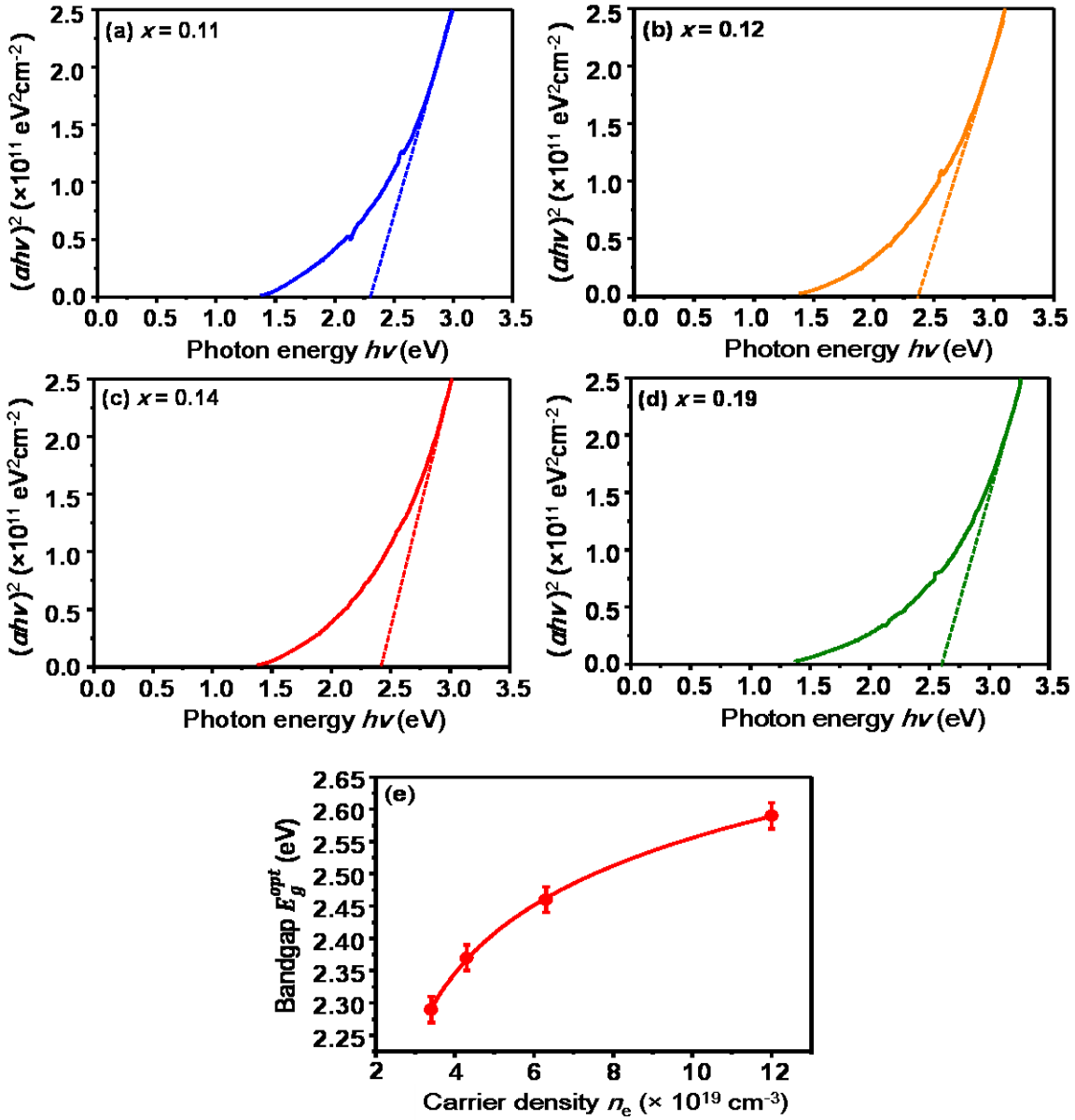

Figure 3.15. Plots of $(\alpha h\nu)^2$ vs. $h\nu$ for $Zn_3N_{2-x}O_x$ films with x = (a) 0.11, (b) 0.12, (c) 0.14, and (d) 0.19. (e) E_g^{opt} as a function of carrier density n_e.

obtained $Zn_3N_{2-x}O_x$ films is attributable not only to the band-to-band transition but also to the defect-to-band transition. The α values calculated for the bandgap estimation would include contributions of both band-to-band (α_B) and defect-to-band (α_D) transitions: *i.e.*, $\alpha = \alpha_B + \alpha_D$. If so, the E_g^{opt} values evaluated from the $h\nu$–$(\alpha h\nu)^2$ plots are smaller than the true bandgap energy.

The true E_g^{opt} value of Zn_3N_2 remains undetermined: values ranging from 1.01 to 3.4 eV have been reported so far [5, 9, 22-24, 28-29, 37-40, 42]. The range of E_g^{opt} spans over 2 eV, which is unusual for general semiconductors. The highest E_g^{opt} value of 3.2 eV was reported in Refs. 5, 38–40, whereas E_g^{opt} values reported in Refs. 9, 23-24, and 28-29 were as low as 1.0–1.7 eV. Furthermore, intermediate values, ranging from 2.1 to 2.7 eV, similar to our E_g^{opt} values, were also reported [43-45]. This discrepancy can be interpreted in terms of the contribution of the defect-to-band transition, as follows. Zn_3N_2 films for which the literature values were reported were deposited by using various techniques and under different conditions. The formation energy of N_I depends on whether the deposition condition is N-rich or N-poor [27]. Thus, the N_I density would be different in each Zn_3N_2 film, yielding different α_D values. The variation of α_D would be responsible for the disagreement with the reported E_g^{opt} values.

3.4 Summary

In chapter 3, we investigated the properties of oxygen-doped Zn_3N_2 as a potential nitride-based transparent conductor. Polycrystalline films of Zn_3N_2, intentionally doped with oxygen, were reactively sputtered from a Zn target using a gas mixture of Ar, N_2, and O_2. XRD and XPS measurements revealed the substitution of oxygen on the nitrogen site in Zn_3N_2 films. We demonstrated that electron transport properties could be controlled by varying x in $Zn_3N_{2-x}O_x$. Heavily doped $Zn_3N_{2-x}O_x$ films with x = 0.11–0.19 were n-type degenerate semiconductors. The free electron density (n_e) in $Zn_3N_{2-x}O_x$ films increased from 3.4×10^{19} to 1.2×10^{20} cm^{-3} as x increased from 0.11 to 0.19, indicating that the substitutional oxygen behaves as an electron donor. As a result, a highly conducting $Zn_3N_{2-x}O_x$ film with a resistivity of 6.2×10^{-4} Ω cm was obtained for x = 0.19. It is notable that $Zn_3N_{2-x}O_x$ films exhibited electron mobility (μ) above 70 cm^2 V^{-1} s^{-1} even in polycrystalline form. The μ values were approximately 100-fold those in degenerately doped GaN polycrystalline films and two-fold those in polycrystalline TCOs. Therefore, $Zn_3N_{2-x}O_x$ can be regarded as a high-mobility nitride-based semiconductor. Detailed

analysis of mobility revealed that the electron transport is governed by ionized impurity scattering at temperatures ranging from 77 to 350 K. In addition, the main ionized scattering center was found to be the substitutional oxygen. Bandgap widening due to the Burstein–Moss effect was observed, supporting the notion that $Zn_3N_{2-x}O_x$ was degenerately doped. The optical gap (E_g^{opt}) was estimated to range from 2.3 to 2.6 eV, which was smaller than the previously reported value of 3.2 eV. We postulate that the small E_g^{opt} originates from the optical absorption by electron transition between the interstitial N 2p in-gap state and conduction/valence band. Further research is required for achieving truly transparent $Zn_3N_{2-x}O_x$ films with low resistivity reduction of the N_I density.

3.5 Bibliography

[1] F. J. Zong, H. L. Ma, C. S. Xue, H. Z. Zhuang, X. J. Zhang, H. D. Xiao, J. Ma, and F. Jia, Synthesis and thermal stability of Zn_3N_2 powder, *Solid State. Commun.* **132**, p. 521 (2004).

[2] G. Paniconi, Z. Stoeva, R. I. Smith, P. C. Dippo, B. L. Gallagher, and D. H. Gregory, Synthesis, stoichiometry and thermal stability of Zn_3N_2 powders prepared by ammonolysis reactions, *J. Solid State Chem.* **181**, p 158 (2008).

[3] A. Trapalis, J. Heffernan, I. Farrer, J. Sharman, and A. Kean, Structural, electrical, and optical characterization of as grown and oxidized zinc nitride thin films, *J. Appl. Phys.* **120**, p. 205102 (2016).

[4] X. Cao, Y. Yamaguchi, Y. Ninomiya, and N. Yamada, Comparative study of electron transport mechanisms in epitaxial and polycrystalline zinc nitride films, *J. Appl. Phys.* **119**, p. 025104 (2016).

[5] F. J. Zong, H. L. Ma, J. Ma, W. Du, X. J. Zhang, H. D. Xiao, F. Ji, and C. S. Xue, Structural Properties and Photoluminescence of Zinc Nitride Nanowires. *Appl. Phys. Lett.* **87**, p. 233104 (2005).

[6] M. Zervos, C. Karipi, and A. Othonos, Zn_3N_2 nanowires: growth, properties and oxidation, *Nanoscale Res. Lett.* **8**, p. 221 (2013).

[7] W. S. Khan, C. B. Cao, Z. Alia, F. K. Butt, N. A. Niaz, A. Baig, R. ud Din, M. H. Farooq, F. P. Wang, and Q. ul Ain, Solvo-solid preparation of Zn_3N_2 hollow structures; their PL yellow emission and hydrogen absorption characteristics, *Matter. Lett.* **65**, p. 2127 (2011).

[8] F. J. Zong, H. L. Ma, C. S. Xue, W. Du, X. J. Zhang, H. D. Xiao, J. Ma, and F. Ji, Structural properties of zinc nitride empty balls, *Matter. Lett.* **60**, p. 905 (2006).

[9] T. Suda and K. Kakishita, Bandgap energy and electron effective mass of polycrystalline Zn_3N_2, *J. Appl. Phys.* **99**, p. 076101 (2006).

[10] D. K. Maurya, A. Sardarinejad, and K. Alameh, Recent developments in R.F. magnetron sputtered thin films for pH sensing applications–An overview, *Coatings* **4**, p.

756 (2014)

[11] Micro Magnetics, Inc., *Magnetron Sputtering Technology*, Retrieved from http://www.directvacuum.com/pdf/what_is_sputtering.pdf

[12] P. J. Kelly and R. D. Arnell, Magnetron sputtering: a review of recent developments and applications, *Vacuum* **56**, p. 159 (2000)

[13] J. B. Webb, D. F. Williams, and M. Buchanan, Transparent and highly conductive films of ZnO prepared by rf reactive magnetron sputtering, *Appl. Phys. Lett.* **39**, p. 640 (1981).

[14] V. Şenay, S. Pat, Ş. Korkmaz, T. Aydoğmuş, S. Elmas, S. Özen, N. Ekem, and M. Z. Balbağ, ZnO thin film synthesis by reactive radio frequency magnetron sputtering, *Appl. Surf. Sci.* **318**, p. 2 (2014).

[15] C. Chen, Y. Cheng, Q. L. Dai, and H. W. Song, Radio frequency magnetron sputtering deposition of TiO_2 thin films and their perovskite solar cell applications, *Sci. Rep.* **5**, p. 17684 (2015).

[16] L. Y. Liang, H. T. Cao, Q. Liu, K. M. Jiang, Z. M. Liu, F. Zhuge, and F. L. Deng, Substrate biasing effect on the physical properties of reactive RF-magnetron-sputtered aluminum oxide dielectric films on ITO glasses, *ACS Appl. Mater. Interfaces* **6**, p. 2255 (2014).

[17] A. Kale, R. S. Brusa, and A. Miotello, Structural and electrical properties of AlN films deposited using reactive RF magnetron sputtering for solar concentrator application, *Appl. Surf. Sci.* **258**, p. 3450 (2012).

[18] M. Jiang, X. Cao, S. H. Bao, H. J. Zhou, and P. Jin, Regulation of the phase transition temperature of VO2 thin films deposited by reactive magnetron sputtering without doping, *Thin Solid Films*, **562**, p. 314 (2014).

[19] T. Suzuki, S. Hibino, R. Katayama, Y. Kato, F. Ohashi, T. Itoh, and S. Nonomura, Effects of substrate temperature on properties of amorphous $In_xGa_{1-x}N$ films deposited by reactive radio frequency sputtering, *Jpn. J. Appl. Phys.* **52**, p. 11NG05 (2013).

[20] K. Ellmer and T. Welzel, Reactive magnetron sputtering of transparent conductive oxide thin films: Role of energetic particle (ion) bombardment, *J. Mater. Res.* **27**, p. 765

(2002).

[21] D. A. Shirley, High-Resolution X-Ray Photoemission Spectrum of the Valence Bands of Gold, *Phys. Rev. B* **5**, p. 4709 (1972).

[22] K. Toyoura, H. Tsujimura, T. Goto, K. Hachiya, R. Hagiwara, R. And Y. Ito, Optical properties of zinc nitride formed by molten salt, electrochemical process. *Thin Solid Films* **492**, p. 88 (2005).

[23] M. Futsuhara, K. Yoshioka, and O. Takai, Structural, electrical and optical properties of zinc nitride thin films prepared by reactive RF magnetron sputtering. *Thin Solid Films* **322**, p. 274 (1998).

[24] N. K. Jiang, D. G. Georgiev, A. H. Jayatissa, R. W. Collins, J. Chen, and E. McCullen, Zinc nitride films prepared by reactive RF magnetron sputtering of zinc in nitrogen-containing atmosphere. *J. Phys. D: Appl. Phys.* **45**, p. 135101. (2012).

[25] G. Z. Xing, D. D. Wang, B. Yao, L. F. N. Ah Qune, T. Yang, Q. He, J. H. Yang, and . L. Yang, Structural and electrical characteristics of high quality (100) orientated-Zn_3N_2 thin films grown by radio-frequency magnetron sputtering. *J. Appl. Phys.* **108**, p. 083710 (2010).

[26] R. Long, Y. Dai, L. Yu, B. B. Huang, and S. H. Han, Atomic geometry and electronic structure of defects in Zn_3N_2, *Thin Solid Films* **516**, p. 1297 (2008).

[27] N. K. Jiang, J. L. Roehl, S. V. Khare, D. G. Georgiev, and A. H. Jayatissa, An *ab initio* computational study of pure Zn_3N_2 and its native point defects and dopants Cu, Ag and Au. *Thin Solid Films* **564**, p. 331 (2014).

[28] T. L. Yang, Z. S. Zhang, Y. H. Li, M. S. Lv, S. M. Song, Z. C. Wu, J. C. Yan, and S. H. Han, Structural and optical properties of zinc nitride films prepared by rf magnetron sputtering, *Appl. Surf. Sci.* **255**, p. 3544 (2009).

[29] C. G. Núñez, J. L. Pau, M. J. Hernández, M. Cervera, E. Ruiz, and J. Piqueras, On the zinc nitride properties and the unintentional incorporation of oxygen, *Thin Solid Films* **520**, p. 1924 (2012).

[30] J. F. Moulder, W. F. Stickle, P. E. Sobol, and K. D. Bomben, *Handbook of X-ray Photoelectron Spectroscopy*, Physical Electronics, Inc.: Chanhassen, MN, 1995.

[31] R. D. Shannon, Revised effective ionic radii and systematic studies of interatomic distances in halides and chalcogenides. *Acta Crystallogr.* **A 23**, p. 751 (1976).

[32] R. Long, Y. Dai, L. Yu, M. Guo, and B. B. Huang, Structural, electrical, and optical properties of oxygen defects in Zn_3N_2, *J. Phys. Chem. B* **111**, p. 3379 (2007).

[33] H. Sato, T. Minami, E. Yamada, M. Ishii, and S. Takata, Transparent and conductive impurity-doped GaN thin films prepared by an electron cyclotron resonance plasma metalorganic chemical vapor deposition method. *J. Appl. Phys.* **75**, p. 1405 (1994).

[34] D. S. Ginley, H. Hosono, D. C. Paine, Eds. *Handbook of Transparent Conductors*, Springer: New York, 2010.

[35] V. I. Fistul', *Heavily Doped Semiconductors*, Plenum Press, New York, 1969.

[36] M. Zervos, C. Karipi, and A. Othonos, Zn_3N_2 Nanowires: growth, properties and oxidation. *Nanoscale Res. Lett.* **8**, p. 221 (2013).

[37] N. Yamada, K. Watarai, T. Yamaguchi, A. Sato, and Y. Ninomiya, Transparent conducting zinc nitride films, *Jpn. J. Appl. Phys.* **53**, p. 05FX01 (2014).

[38] K. Kuriyama, Y. Takahashi, and F. Sunohara, Optical band gap of Zn_3N_2 films, *Phys Rev B* **48**, p. 2781 (1993).

[39] S. Sinha and S. K. Sarkar, Atomic layer deposition of textured zinc nitride thin films. *RSC Adv.* **4**, p. 47177 (2014).

[40] R. Ayouchi, C. Casteleiro, L. Santos, and R. Schwarz, RF-plasma assisted PLD growth of Zn_3N_2 thin films. *Phys. Status Solidi C.* **7**, p. 2294 (2010).

[41] K. Seeger, *Semiconductor Physics*; *An Introduction*, Springer, New York, 2011.

[42] V. Kambilafka, P. Voulgaropoulou, S. Dounis, E. Iliopoulos, M. Androulidaki, V. Šály, M. Ružinský, and E. Aperathitis, Thermal oxidation of *n*-type ZnN films made by rf-sputtering from a zinc nitride target, and their conversion into *p*-type films, *Superlattices Microstruct.* **42**, p. 55 (2007).

[43] F. J. Zong, H. L. Ma, W. Du, J. Ma, X. J. Zhang, H. D. Xiao, F. Ji, and C. S. Xue, Optical band gap of zinc nitride films prepared on quartz substrates from a zinc nitride target by reactive RF magnetron sputtering. *Appl. Surf. Sci.* **252**, p. 7983 (2006).

[44]J. Y. Wu, J. L. Yan, W. Yue, and T. Li, Structural and optical properties of Zn_3N_2 films prepared by magnetron sputtering in NH_3−Ar mixture gases. *J. Semicond.* **33**, p. 043001 (2012).

Chapter 4

Origin of High Electron Mobility of Zn_3N_2 Films: Effective Electron Mass and Electron Transport Mechanisms

Without continual growth and progress, such words as improvement, achievement, and success have no meaning.

—Benjamin Franklin

4.1 Background and Objective

As we illustrated in previous parts, zinc nitride as a *n*-type semiconductor has been undergoing a considerable revival in the past three decades [1-8]. One crucial reason for zinc nitride regained substantial research attentions resides with its the seductive electrical properties of Zn_3N_2 films even in polycrystalline form, especially the high electron mobility [9-11]. Noted here that even for degenerate polycrystalline Zn_3N_2 films, electron mobility values higher than 80 $cm^2\ V^{-1}\ s^{-1}$ are still achievable in Refs. [12-14]. The electron mobility values are extraordinarily large for a nitride semiconductor, because electron mobility values of GaN [15], (In,Ga)N [16] and InN [17] polycrystalline films are typically less than 10 $cm^2\ V^{-1}\ s^{-1}$. Accordingly, Zn_3N_2 can be regarded as a high-electron mobility *n*-type semiconductor. What's more, a recent theoretical study suggested the possibility of bipolar doping of Zn_3N_2 [18]. Therefore, it is important and necessary to

reveal the unknown origin of the high electron mobility of Zn_3N_2 material when considering it as an attractive nitride semiconductor composed of non-toxic, Earth-abundant, environmental-friendly elements.

The high electron mobility in polycrystalline Zn_3N_2 films gives us an indication that optimization in material quality may bring about further improvement of its electrical properties. The first literature on Zn_3N_2 thin films by Kuriyama's group [19]. reported its polycrystalline form. Inspired by their successful thin-film growth and stimulating findings, more and more group have grown Zn_3N_2 thin films by using various techniques such as sputtering [11-14, 20-22], pulse laser deposition [23], molecular beam epitaxy [24-25], chemical vapor deposition [24,26], and an electrochemical process [27]. One common thing is that all of their thin films were in polycrystalline form. However, single-crystal or epitaxial growth of Zn_3N_2 has rarely been reported so far, in contrast the current reports on Zn_3N_2 polycrystalline films with poor crystallinity. Hence, the influence of crystallinity on the electrical and optical properties of Zn_3N_2 films has not been elucidated yet. Electron transport in polycrystalline films usually suffers from scattering at the grain boundary, though polycrystalline films grown at low temperature are technologically important for low-cost electronic devices. Thus, it is also important to examine effects of the grain boundary scattering on electron transport in Zn_3N_2 polycrystalline films.

In this Chapter, we prepared both epitaxial and polycrystalline films of Zn_3N_2 on the (100) plane of yttria-stabilized zirconia ($Y_{0.13}Zr_{0.87}O_2$; YSZ) single crystalline substrates, and analyzed their electron transport properties by means of direct current (DC) and optical techniques. The YSZ has a cubic fluorite structure with an *a*-axis length of 0.513 nm. Thus, a relatively small lattice mismatch value of ~4.8% between *a* of Zn_3N_2 and 2*a* of YSZ is expected, suggesting the heteroepitaxial growth of Zn_3N_2.

4.2 Preparation Details for Epitaxial Zn_3N_2 Thin Films

4.2.1 Thin Film Growth Methods

Zn_3N_2 thin films were grown on YSZ(100) single-crystal substrates with substrate temperatures ranging from 100−250 °C by the reactive radio frequency (RF) magnetron sputtering technique. A disk of metal Zn was used as the target (a diameter of 10 cm and purity of 99.9%). The substrates were ultrasonically degreased in methanol for 5 min, and then in acetone for 5 min, and one more time in methanol for 5 min. At last, they were dried with nitrogen gas blowing. An RF power of 80 W was applied to the Zn target. A base pressure lower than 2×10^{-4} Pa was established in the growth chamber before the film growth. Sputtering was conducted in a gas mixture consisting of Ar (99.999% pure) and N_2 (99.9995% pure) at a total pressure of 2 Pa. Each gas was introduced into the growth chamber by using a mass flow controller. Thin films were grown under various atmospheres with $f(N_2)$ [$f(N_2) = N_2/(Ar+N_2)$] ranging from 20%–80%. Prior to the growth, the target surface was sputter-etched with pure Ar for 30 min and was subsequently pre-sputtered for 10 min under the same condition with the film growth. The growth time was adjusted to obtain a thin film with a thickness of 250–300 nm. After the film growth, the films were immediately stored in another vacuum chamber (the pressure was about 1 Pa) for subsequent measurements.

4.2.2 Characterizations for Epitaxial Zn_3N_2 Thin Films

Crystalline phases of the films were examined by X-ray diffraction (XRD) measurements using a four-axis diffractometer with Cu Kα radiation (Rigaku ATX-E). In addition to conventional θ–2θ scans, φ–scans were also performed in order to determine the in-plane epitaxial relationship between epitaxial films and substrates. For polycrystalline films with poor crystallinity, the crystalline phases were analyzed by using GIXRD (grazing incidence X-ray diffraction) measurements with an X-ray incident angle of 0.3°. All XRD

patterns were recorded with a scan speed of 1.000 °/min. Surface morphology was observed by using a scanning electron microscope (SEM; JEOL JSM-6510LA). X-ray photoelectron spectroscopy (XPS) using monochromated Al Kα radiation (PHI Versa Probe) was employed for examining the composition of the films. The XPS measurements were carried out after mild Ar^+-sputter etching (ion energy of 4 keV and emission current of 7 mA) for 2 min to avoid the influence of adsorbed species, such as oxygen, on XPS signals. Constant-depth profiles of the peak intensities of zinc, oxygen, and nitrogen were confirmed after removal of adsorbates [12]. The resistivity (ρ) of the films was measured using the van der Pauw method with a source current of 1 mA. Carrier density (n_e) and Hall mobility (μ_H) were determined by Hall effect measurement in the van der Pauw configuration (Toyo Corp. Resitest 8200). Magnetic fields of ±1 T were applied normal to the film surface. The thermopower (Seebeck coefficient S) measurements were performed using a standard DC technique with a custom-made setup. A temperature gradient (usually chosen to be less than 5 K) was provided using a Manganin wire heater, and the temperatures at the cold and hot ends were measured with a calibrated K-type thermocouple. The thermovoltages were recorded with a digital multimeter (Keithley 2000). Electron transport measurements were all carried out at room temperature. Infrared transmittance at normal incidence and reflectance at near-normal incidence (~5°) in a wavenumber range of 1000–4600 cm^{-1} were measured by using a Fourier transform infrared (FTIR) spectrophotometer (Shimadzu IRAffinity-1). To minimize film oxidation and/or hydroxylation, all measurements were performed within a day after the film growth.

4.3 Results for Growth and Characterizations of Zn_3N_2 Films

4.3.1 Thin Film Growth

Structure and phase composition of Zn_3N_2 films strongly depended on the growth conditions. In particular, substrate temperature (T_s) and nitrogen concentration in the

sputtering atmosphere [$f(N_2)$] were the two crucial parameters. Figure1 depicts the phase diagram for Zn_3N_2 thin films grown on YSZ(100) substrates, as functions of T_s and f (N_2).

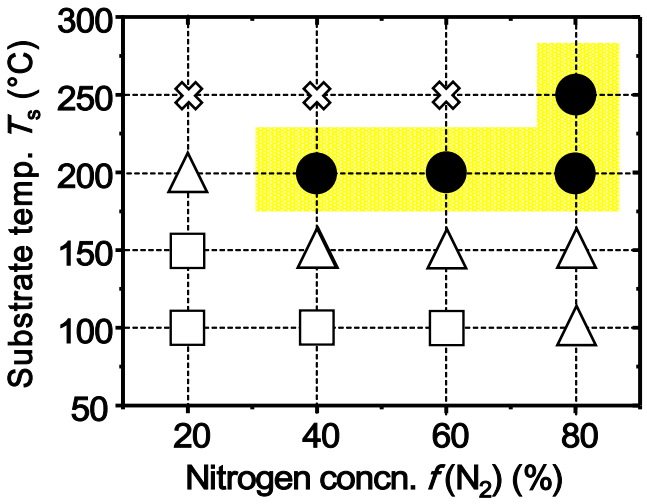

Figure 4.1. T_s–$f(N_2)$ growth parameter-based phase diagram of Zn_3N_2 thin films on yttria-stabilized zirconia (100) substrates: circles, triangles, and squares denote Zn_3N_2 epitaxial films, single phase Zn_3N_2 polycrystalline films, and polycrystalline films composed of metal Zn and Zn_3N_2, respectively. The shadowed region represents the growth condition for Zn_3N_2 epitaxial films. Thin films were not grown under the conditions represented by cross marks.

As shown in Figure 4.1, epitaxial growth occurred in a relatively narrow region (closed circles in the shadowed region). Hereafter, we refer to the shadowed region in Figure 4.1 as the epitaxial region. Thin films grown at T_s lower than the epitaxial region were in polycrystalline form. Phase-pure Zn_3N_2 polycrystalline films were obtained when we conducted the growth at a T_s of 150 °C with sufficient N_2 supplied to the growth chamber (triangles). The polycrystalline nature was confirmed from GIXRD patterns shown in Figure 4.2(a). In this figure, a halo pattern at 2θ around 30–35° is visible, indicating that the polycrystalline film somewhat contains an amorphous phase. That is, Zn_3N_2 polycrystalline films grown at low temperatures had poor crystallinity. In fact, when XRD

measurements were carried out in the conventional θ–2θ mode, we could not observe clear diffraction peaks. Further decrease in T_s to 100 °C resulted in the growth of mixture films of metal Zn and Zn_3N_2 (squares). Since low T_s does not provide enough thermal energy to promote the chemical reaction between zinc and nitrogen on the substrates, mixture films of Zn and Zn_3N_2 were obtained. The GIXRD pattern for the film grown at T_s = 100 °C and $f(N_2)$ = 40% is presented in Figure 4.2(b). Peaks from metal Zn are clearly seen.

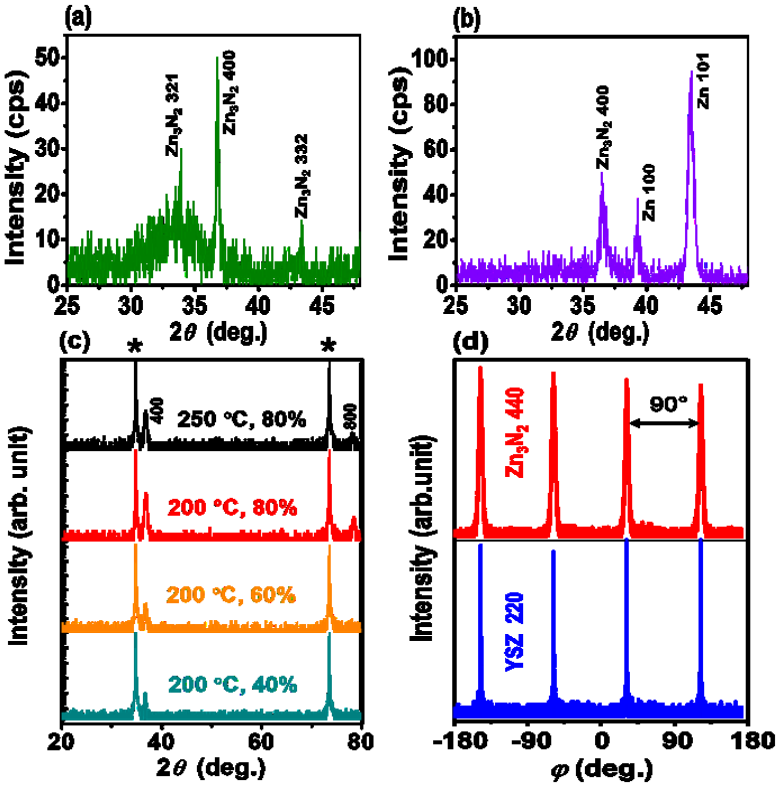

Figure 4.2. Grazing incidence X-ray diffraction (GIXRD) profiles of (a) a film grown at T_s = 150 °C and $f(N_2)$ = 60% and (b) a film grown at T_s = 100 °C and $f(N_2)$ = 40%. (c) θ–2θ XRD profiles of Zn_3N_2 film deposited under the growth condition of the epitaxial region. Diffraction peaks from the substrates are marked by asterisks. 400 and 800 diffraction peaks from Zn_3N_2 are also labeled. (d) φ−scan patterns of Zn_3N_2 440 and yttria-stabilized zirconia (YSZ) 220 for a Zn_3N_2 film grown at T_s = 200 °C and $f(N_2)$ = 80%.

Meanwhile, we could hardly grow thin films at T_s higher than the epitaxial region (T_s > 250 °C). One possible reason for this is the re-evaporation of zinc from the substrate surface before reacting with nitrogen, because zinc is an element with very high vapor

pressure even at low temperature [28]. Another possible reason may be the decomposition of Zn_3N_2, because it partially decomposes at temperatures as low as 200−500 °C [29]. As a result, Zn_3N_2 epitaxial films were grown in the narrow epitaxial process window.

Figure 4.2(c) displays θ–2θ XRD profiles of Zn_3N_2 thin films grown in the epitaxial region. Besides 200 and 400 diffraction peaks from the substrates, only 400 and 800 diffraction peaks from Zn_3N_2 were observed. The results indicated that the films are 100-orientated and the (100) planes are parallel to the (100) planes of the substrates, i.e., the out-of-plane orientation relationship is $(100)_{Zn_3N_2} \parallel (100)_{YSZ}$. To examine the in-plane relationship, XRD asymmetric reflection measurements in φ–scan mode were performed. Figure 4.2(d) depicts typical φ–scan patterns of the Zn_3N_2 440 and YSZ 220 peaks. Four evenly spaced peaks from Zn_3N_2 and YSZ were clearly observed, which reflects four-fold rotational symmetry around the [100] direction of both the Zn_3N_2 and the YSZ. The coincidence in φ–positions of the Zn_3N_2 440 and YSZ 220 peaks is seen in Figure 4.2(d). The zone axis associated with the (100) and (110) planes of a cubic system is [001]. Therefore, the result presented in Figure 2(d) indicates that the zone axis in the Zn_3N_2 is aligned with that in the YSZ, *i.e.*, the in-plane epitaxial relationship is $[001]_{Zn_3N_2} \parallel [001]_{YSZ}$. From the XRD measurements, we confirmed that Zn_3N_2 was epitaxially grown on YSZ(100) with the epitaxial relationship of $(100)[001]_{Zn_3N_2} \parallel (100)[001]_{YSZ}$ under the limited growth condition mentioned above.

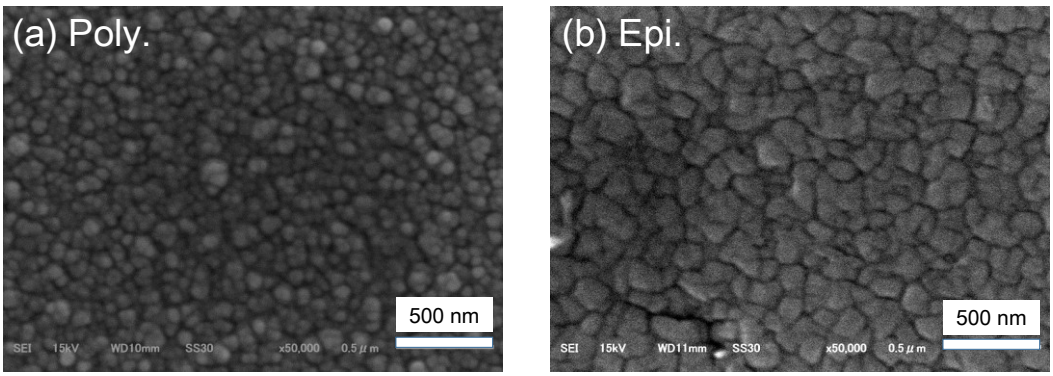

Figure 4.3. Top-view scanning electron microscopy (SEM) images with ×50,000 magnification for (a) polycrystalline and (b) epitaxial film.

Typical SEM images for polycrystalline and epitaxial films, respectively, are shown in Figures 4.3(a) and 4.3(b) as above. The polycrystalline film has a homogeneous compact structure comprising small grains with diameters of ~100 nm. On the other hand, the epitaxial film is composed of larger grains with diameters of 200–300 nm and has a smoother surface.

4.3.2 Unintentional Oxygen Incorporation

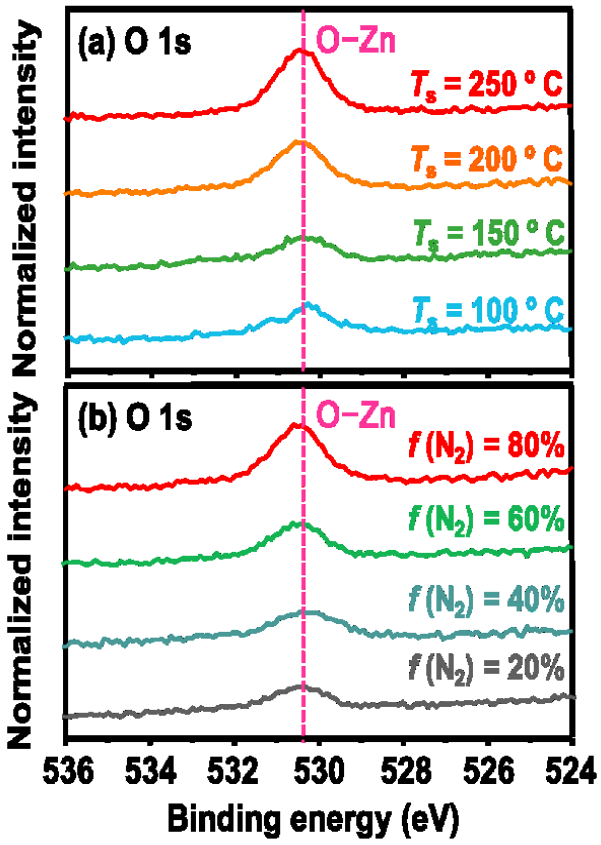

Figure 4.4. O 1s X-ray photoelectron spectroscopy (XPS) core spectra of 2 min–long sputter-etched surfaces for Zn_3N_2 films grown at (a) substrate temperatures T_s ranging from 100 to 250 °C, and (b) nitrogen concentrations $f(N_2)$ varying from 20% to 80%. Peaks at *BE* ~530.4 eV were attributed to O–Zn bonds. The dashed lines are a guide for the eyes.

Unintentional oxygen incorporation into Zn_3N_2 films during the film growth has been reported [12-14,20,22,24]. The incorporated oxygen is believed to come from water vapor

in the residual gas present in the growth chamber. Unintentional incorporation into Zn_3N_2 films was observed even when the growth chamber was pumped down to $<10^{-4}$ Pa before the film growth [14, 22]. The incorporated oxygen partially replaces lattice-nitrogen in Zn_3N_2 and acts as an electron donor [12, 30], which is very similar to the InN case [31, 32]. We performed semi-quantitative analysis of oxygen concentration in Zn_3N_2 films using XPS measurements.

Figure 4.4(a) shows O 1s core spectra for Zn_3N_2 films grown at T_s ranging from 100–250 °C. These spectra clearly indicate the existence of oxygen in the Zn_3N_2 films. The O 1s peaks are located in the vicinity of a binding energy (*BE*) of 530.4 eV. Hence, these peaks were attributed to O–Zn bonds [13, 22]. The spectra were normalized with respect to the intensity of Zn $2p_{3/2}$ peaks, so as to reflect the oxygen-to-zinc atomic ratio (X_O/X_{Zn}) in the Zn_3N_2 films. As seen from Figure 4.4(a), the peak intensity gradually increased with increasing T_s, implying an increase in X_O/X_{Zn}. This phenomenon is probably due to the enhancement of the reactivity between zinc and oxygen on the growing film surface with the increase in T_s. Moreover, the increase in T_s could promote the desorption of nitrogen from the film surface, because Zn_3N_2 has a low decomposition temperature [29]. This could also be one reason for the increase in X_O/X_{Zn} with increasing T_s.

On the basis of the relative sensitivity factor (RSF) method, the ratio X_O/X_{Zn} can be estimated from the formula $X_O/X_{Zn} = (I_O/I_{Zn})(S_{Zn}/S_O)$, where I_O and I_{Zn} respectively represent the integral intensities of the O 1s and Zn $2p_{3/2}$ peaks, and S_{Zn} and S_O are the RSFs of zinc and oxygen, respectively. Representing the composition of the films as $Zn_3N_{2-x}O_x$, x values were calculated from the relationship $x = 3(X_O/X_{Zn})$. Although x values derived from XPS results are semiquantitative, we confirmed that the x values could explain electrical and optical properties of oxygen-doped Zn_3N_2 [12]. For the calculation of x, we used $S_O = 0.711$ and $S_{Zn} = 3.354$ as provided by PHI [33]. We obtained $x = 0.04$, 0.05, 0.10, 0.11 at $T_s = 100$, 150, 200, 250°C, respectively (also see Table 4.1 and Figure 4.5(b)). The x values were consistent with those determined by more accurate Rutherford

backscattering spectrometry for unintentionally oxygen-doped Zn_3N_2 films grown under growth conditions similar to ours [14].

O 1s core spectra for Zn_3N_2 films grown at $f(N_2)$ ranging from 20–80% are displayed in Figure 4.4(b). The O 1s peaks located at $BE \sim 530.4$ eV were attributed to O–Zn bonds. These spectra are also normalized with respect to the intensity of Zn $2p_{3/2}$ peaks. Figure 4.4(b) suggests that an increase in X_O/X_{Zn} occurred when an increase in $f(N_2)$ occurred. We estimated x values by the above-mentioned RSF method: $x = 0.05$ at $f(N_2) = 20\%$, $x = 0.08$ at $f(N_2) = 40\%$, $x = 0.09$ at $f(N_2) = 60\%$, and $x = 0.10$ at $f(N_2) = 80\%$ (also see Table 4.1 and Figure 4.6(b)). Although the reason why x increased with increasing $f(N_2)$ has not been clarified yet, the variation of electrical properties of Zn_3N_2 can be interpreted in terms of the $f(N_2)$ dependence of x, as discussed in section 4.3.3.

4.3.3 Electron Transport Properties

Both Hall coefficients R_H and Seebeck coefficients S for the Zn_3N_2 films were always negative (see Table 4-1), indicating that the Zn_3N_2 films show n-type conductivity. Figure 6.5(a) shows the T_s dependence of carrier density n_e. The films had n_e values larger than 10^{19} cm^{-3}, regardless of T_s. In our study, Zn_3N_2 having $n_e > 10^{19}$ cm^{-3} was identified as a degenerate semiconductor [12]. Hence, those films had degenerate conduction electrons. As seen from Figure 4.5(a), n_e monotonically increased with increasing T_s. That is, n_e values in the epitaxial films were larger than those in the polycrystalline ones. This gives us an impression that improvements in the crystallinity of Zn_3N_2 may enhance n_e. However, n_e does not have a crucial relationship to the crystallinity. As displayed in Figure 4.5(b), T_s dependence of oxygen concentration in Zn_3N_2 was very similar to that of n_e. Since oxygen incorporated in Zn_3N_2 behaves as an electron donor (oxygen occupies a nitrogen site), we concluded that the dependence of n_e on T_s is mainly determined by oxygen concentration in Zn_3N_2 films.

Table 4.1. Electron transport properties in Zn_3N_2 films. The errors were determined by several different least squares fitting runs using different initial parameters.

Sample				n_e	S	ω_p	τ	m_e^*/m_0	μ_H	μ_{opt}
T_s	$f(N_2)$	x	form	(cm^{-3})	($\mu V\ K^{-1}$)	($10^{14}\ s^{-1}$)	(10^{-14} s)		($cm^2\ V^{-1}\ s^{-1}$)	
100 °C	80%	0.04	Poly.	2.3×10^{19}	−55.3	6.8 ± 0.5	1.1 ± 0.2	0.16 ± 0.03	56	114 ± 5
150 °C	80%	0.05	Poly.	2.5×10^{19}	−50.1	7.2 ± 0.3	1.1 ± 0.1	0.17 ± 0.02	62	112 ± 2
200 °C	20%	0.05	Poly.	1.3×10^{19}	−76.4	– [a]	– [a]	– [a]	73	–
200 °C	40%	0.08	Epi.	6.2×10^{19}	−34.1	8.3 ± 0.3	1.2 ± 0.1	0.29 ± 0.02	68	75 ± 5
200 °C	60%	0.09	Epi.	6.8×10^{19}	−35.5	8.8 ± 0.1	1.2 ± 0.1	0.28 ± 0.01	65	77 ± 1
200 °C	80%	0.10	Epi.	7.1×10^{19}	−34.0	8.7 ± 0.3	1.0 ± 0.1	0.30 ± 0.02	64	67 ± 4
250 °C	80%	0.11	Epi.	9.8×10^{19}	−24.9	9.1 ± 0.1	1.1 ± 0.2	0.37 ± 0.01	58	56 ± 3

[a]Drude-fitting could not be applied to the infrared transmittance and reflectance spectra.

A plot of electrical resistivity ρ against T_s is displayed in Figure 4.5(c). A steep decrease in ρ with increasing T_s is clearly seen. While n_e strongly depends upon T_s as described above, μ_H shows relatively weak T_s dependence, as shown in Figure 4.5(d). Thus, the ρ–T_s behavior is concluded to be a result of the variation in n_e with T_s. Hall mobility, μ_H, as a function of T_s is displayed in Figure 4.5(d). A weak bell-shaped dependence of μ_H on T_s is seen in this figure. It should be noted that μ_H values of the polycrystalline films with poor crystallinity are comparable to those of the epitaxial films. Namely, even in polycrystalline films with poor crystallinity, high electron mobility is achievable. This is due to a small electron effective mass of $< 0.2m_0$ (m_0 denotes the free electron mass) in Zn_3N_2 with $n_e < 3\times10^{19}$ cm^{-3} (see Table 4.1). Details of effective mass and mobility will be discussed in section 4.4.

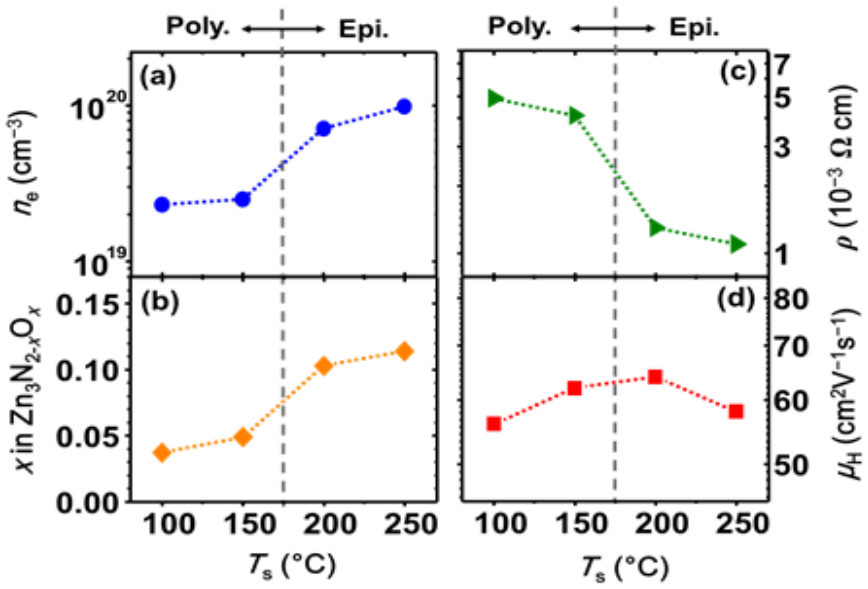

Figure 4.5. (a) Carrier density n_e, (b) x in $Zn_3N_{2-x}O_x$, (c) resistivity ρ, and (d) Hall mobility μ_H of Zn_3N_2 films plotted as functions of the substrate temperature T_s. The films were grown at $f(N_2)$ = 80%. The dashed lines represent the approximate boundary between polycrystalline and epitaxial films.

Next, we present $f(N_2)$ dependence of electrical properties. Figure 4.6(a) shows the $f(N_2)$ dependence of carrier density n_e. The films also had n_e values larger than 10^{19} cm^{-3}, so that these can be regarded as degenerate semiconductors. As shown in Figure 4.6(a), n_e increases as $f(N_2)$ increases. This trend is generally synchronized with an increase in oxygen concentration, shown in Figure 4.6(b). The trend seen in Figure 4.6(a) is explained in terms of the variation in oxygen concentration. As for $f(N_2)$ dependence of ρ (see Figure 4.6(c)), ρ exhibits a decreasing trend that is almost opposite to the increasing trend of n_e. Hence, the decrease in ρ with increasing $f(N_2)$ is largely ascribed to the increase in n_e. Figure 4.6(d) is a plot of μ_H against $f(N_2)$. A gradual decrease in μ_H with increasing $f(N_2)$ is observed in this figure. The decreasing tendency is attributable to the increase in the concentration of oxygen, which behaves as an ionized impurity scattering center. The maximum μ_H value is obtained in the polycrystalline film. This suggests that electron transport in Zn_3N_2 is insensitive to its crystallinity. Surprisingly, the polycrystalline film had a μ_H value of 73 cm^2 V^{-1} s^{-1}, which is more than seven times as large as those of

polycrystalline GaN [15] and InN [17]. The high μ_H value mainly comes from a small electron effective mass of ~0.15m_0 as discussed later.

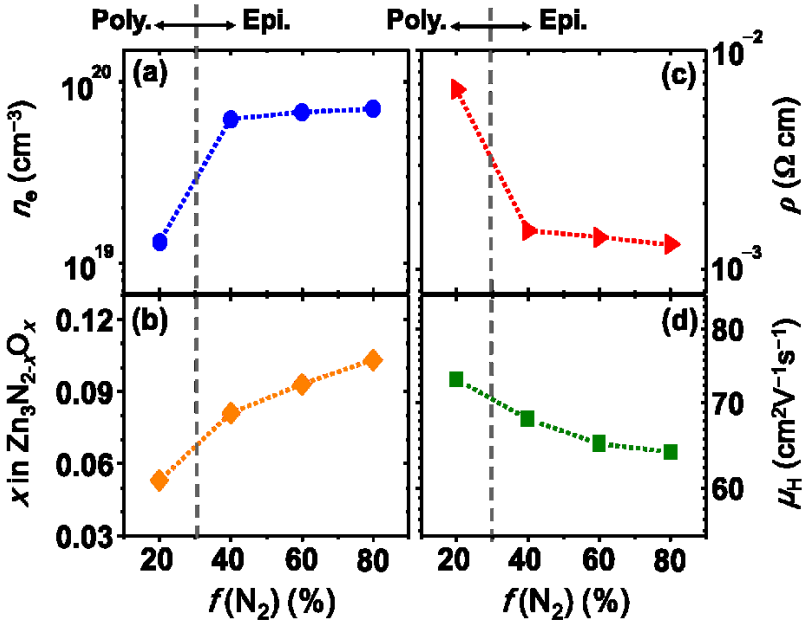

Figure 4.6. (a) Carrier density n_e, (b) x in $Zn_3N_{2-x}O_x$, (c) resistivity ρ, and (d) Hall mobility μ_H of Zn_3N_2 films plotted as functions of nitrogen concentration $f(N_2)$. The films were grown at T_s = 200 °C. The dashed lines represent the approximate boundary between polycrystalline and epitaxial films.

4.4 Discussions for Epitaxial Zn_3N_2 Thin Films

4.4.1 Effective Mass

Effective mass is of great significance for the electron transport properties. We optically derived the electron effective mass (m^*) by using the classical Drude dielectric function. As seen in Figures 4.7(a) and 4.7(b), infrared transmittance and reflectance of epitaxial and polycrystalline films with $n_e > 2 \times 10^{19}$ cm^{-3} showed typical Drude-like behavior: an increase in reflectance and a decrease in transmittance with decreasing wavenumber. As for the polycrystalline films with $n_e = 1.3 \times 10^{19}$ cm^{-3}, the Drude-like behavior could not be observed in this wavenumber range because ω_p is expected to be much smaller than

1000 cm^{-1}. Within the simple Drude model framework, the frequency-dependent dielectric function $\varepsilon(\omega)$ can be expressed as

$$\varepsilon(\omega) = \varepsilon_\infty - \frac{\omega_p^2 \tau}{\omega^2 \tau + i\omega}, \tag{4.1}$$

$$\omega_p = \sqrt{\frac{n_e e^2}{\varepsilon_0 m^*}}. \tag{4.2}$$

where ε_∞ is the high-frequency permittivity (5.8 for Zn_3N_2 [11]), ω_p the plasma frequency, τ the scattering time, e the elementary electric charge, and ε_0 the permittivity of vacuum, respectively.

Theoretical T and R spectra calculated through the Fresnel formulas combined with the Drude dielectric function were fitted to the experimental spectra. In the fitting procedure, ω_p and τ were used as fitting parameters. We obtained fairly good fits for all the films (typical cases presented by solid lines shown in Figures 4.7(a) and 4.7(b)). The best-fit parameters are listed in Table 4.1. The values of m^* can be calculated from Eq. (4.2) using n_e values determined from Hall measurements (the m^* values are listed in Table 4.1). As shown in Figure 4.8, m^* was found to increase with increasing n_e. To our best knowledge, we revealed n_e-dependent m^* in Zn_3N_2 for the first time. A nearly constant m^* value of ~$0.3m_0$ has been reported in literature [8, 24]. These values were determined for only Zn_3N_2 films having n_e on the order of 10^{20} cm^{-3}. The determination of m^* in Zn_3N_2 films with n_e values much lower than 10^{20} cm^{-3} has not been investigated to date. Accordingly, the n_e dependence of m^* has not been revealed until this study. Our m^* values obtained at $n_e > 6 \times 10^{19}$ cm^{-3} are very close to the literature values (see Figure 4.8). On the other hand, m^* values at $n_e < 3 \times 10^{19}$ cm^{-3} were lower than $0.2m_0$, which is smaller than the literature values. The small m^* (< $0.2m_0$) is one reason why high μ_H values are achievable even in polycrystalline films grown at low T_s (see Figure 4.5(d) and Figure 4.6(d)). The attainability of high electron mobility in polycrystalline films grown at low temperatures

makes this material attractive as a semiconductor for cost-effective polycrystalline semiconductor devices, including polycrystalline thin-film transistors.

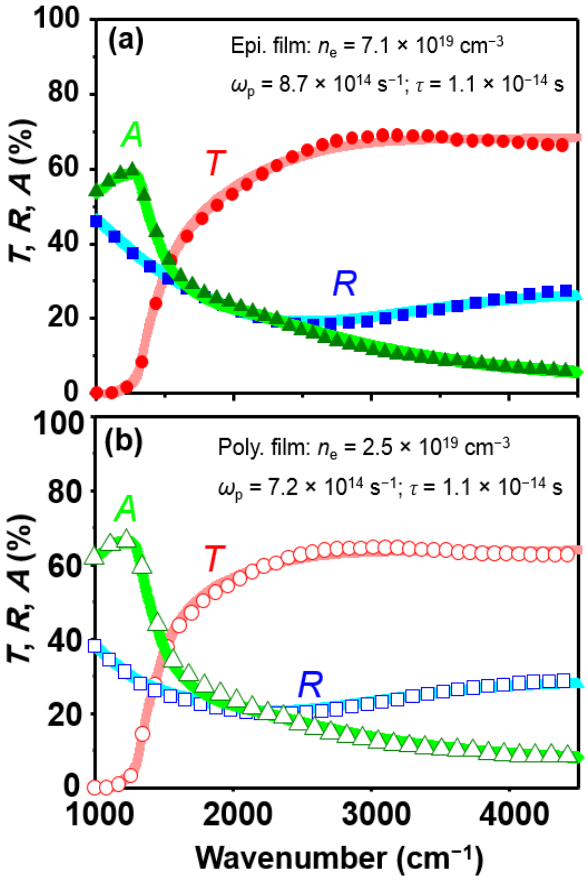

Figure 4.7. Infrared transmittance (T), reflectance (R) and absorption (A) for (a) epitaxial Zn_3N_2 film grown with n_e = 7.1 × 10^{19} cm^{-3} and (b) polycrystalline Zn_3N_2 film with n_e = 2.5 × 10^{19} cm^{-3}. The results of least-squares fitting using the Drude dielectric function are shown as solid lines.

Meanwhile, enhancements in m^* with increasing n_e have been reported for other degenerately doped semiconductors such as GaN [34], InN [35], GaAs [36], InSb [37], TiO_2 [38], ZnO [39-41], Cd_2SnO_4 [42]. Hereafter, the effective mass is denoted $m^*(n_e)$. Such a trend has generally been interpreted as a result of the nonparabolicity of the conduction band. For degenerately doped ZnO in which the conduction band mainly is composed of the Zn 4s state, n_e dependence of $m^*(n_e)$ has been reproduced well by

adopting an empirical non-parabolic band dispersion model $E(k)$:

$$\frac{\hbar^2 k^2}{2m_0^*} = E(k) + \alpha E(k)^2 \quad , \tag{4.3}$$

Where k is the wave vector of the electron, m_0^* is the effective mass at the bottom of the conduction band, and α is the nonparabolic parameter [43]. From Eq. (4.3), n_e-dependent $m^*(n_e)$ is given as

$$m^*(n_e) = m_0^* \sqrt{1 + 2\alpha \frac{\hbar^2}{m_0^*} (3\pi^2 n_e)^{2/3}} \quad . \tag{4.4}$$

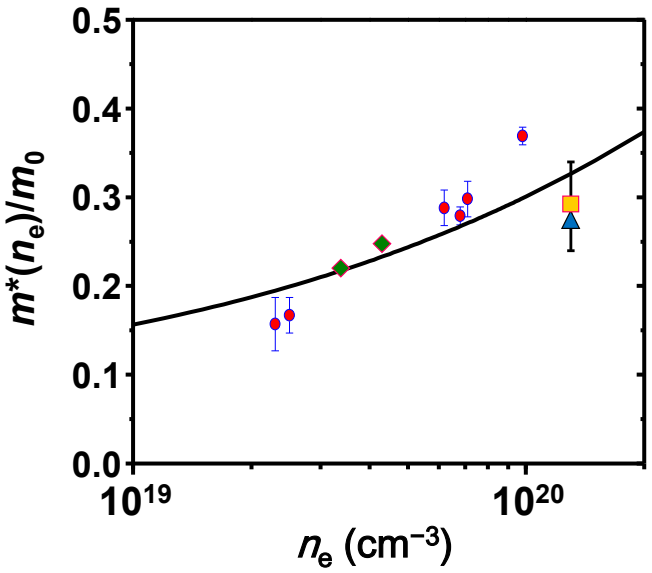

Figure 4.8. Effective mass $[m^*(n_e)/m_0]$ as a function of carrier density n_e. The solid curve represents the theoretical $m^*(n_e)/m_0$ calculated from Eq. (4.4) using $m_0^* = 0.08m_0$ and α = 2.1 eV^{-1}. Literature values are also shown as a closed triangle [8], closed diamonds [12], and a closed square [24].

Since the conduction band in Zn_3N_2 is mainly composed of the Zn 4s state as well, we adopted Eq. (4.4) to analyze $m^*(n_e)$. Eq. (4) was fitted to the experimental $m^*(n_e)$, including literature values, by using m_0^* and α as fitting parameters. We obtained a good fit when m_0^*

and α values were (0.08 ± 0.03) m_0 and (4.0 ± 2.0) eV^{-1}, respectively (presented by the solid line in Figure 4.8). That is, the fitting analysis extracted a very small m_0^* value of (0.08 ± 0.03) m_0, which is comparable to that in InN [44,45]. This result suggests that Zn_3N_2 is promising as a high-mobility semiconductor with small effective mass. To achieve extremely high electron mobility, efforts to grow Zn_3N_2 with low n_e (*i.e.*, a low density of oxygen impurity) are still necessary.

4.4.2 Transport Mechanisms

Although thermopower measurements are useful for understanding the electron transport mechanism, the Seebeck coefficient (S) of Zn_3N_2 has not been reported to date. As mentioned before, we measured S values and the values were always negative, indicating n-type conductivity (see Table 4.1). A plot of $|S|$ versus n_e allows us to gain insight into electron transport mechanisms in a degenerate semiconductor because |S| of a degenerate semiconductor is given by [46]

$$|S| = \frac{8\pi^2}{3}\left(r+\frac{3}{2}\right)\frac{k_B^2 m^* T}{eh^2} n_e^{-\frac{2}{3}}, \tag{4.5}$$

where r represents the scattering constant (e.g., r = 3/2 for ionized impurity scattering, r = 0 for neutral impurity scattering, and r = −1/2 for phonon scattering), k_B is the Boltzmann constant, T is the temperature, and h is the Planck constant.

A log–log plot of $|S|$ *vs.* n_e is shown in Figure 4.9(a). As seen from this figure, the experimental $|S|$ approximately obeys a power law of $n_e^{-2/3}$, which is consistent with Eq. (4.5). Theoretical $|S|$ curves for r = 3/2, 0, −1/2 calculated by taking into account the n_e dependence of $m^*(n_e)$ are also plotted in Figure 4.9(a). The experimental data lie close to the theoretical line for r = 3/2 (solid line), implying that ionized impurity scattering is one of the dominant scattering mechanisms for electron transport in the degenerately doped Zn_3N_2 films. It should be stressed that the $|S|$ values for the epitaxial films are located on

the curve for r = 3/2. That is, the contributions of scattering mechanisms other than the ionized impurity scattering are negligibly small in Zn_3N_2 epitaxial films. As discussed later, this is confirmed by detailed mobility analysis. As for polycrystalline films, the experimental values of $|S|$ somewhat deviate from the theoretical curve for r = 3/2, implying that the contributions of additional scattering mechanisms, including neutral impurity scattering and grain boundary scattering, cannot be ignored.

To get further insights into the electron transport mechanisms, we carried out detailed analysis of electron mobility. We already revealed that μ_H of degenerate Zn_3N_2 films exhibits temperature-independent behavior, which indicates that acoustic and optical phonon scattering do not have significant influence on electron transport [12]. Here, we discuss impurity scattering in Zn_3N_2. In general, a mobility *vs.* carrier density plot provides helpful information to understand impurity scattering of charge carriers in a semiconductor. Figure 4.9(b) shows μ_H values in Zn_3N_2 films as a function of n_e (open circles). This figure also includes our own data [12] for polycrystalline films of Zn_3N_2 (open triangles). The values of μ_H fall in the range of 60–70 $cm^2\ V^{-1}\ s^{-1}$.

The Seebeck data discussed above suggests that ionized impurity scattering is one of the dominant scattering mechanisms in the Zn_3N_2 films. Thus, theoretical mobility limited by ionized impurity scattering (μ_I) was calculated on the basis of the Brooks-Herring-Dingle (BHD) theory [47]. The theoretical μ_I is expressed as

$$\mu_I = \frac{24\pi^3(\varepsilon_0\varepsilon_r)^2\hbar^3}{e^3 m^{*2}} \frac{1}{g(\zeta)} \frac{n_e}{Z^2 n_I}, \tag{4.6}$$

where the scattering function $g(\zeta)$ is given by

$$g(\zeta) = \ln\left(1+\frac{4}{\zeta}\right) - \left(1+\frac{\zeta}{4}\right)^{-1}, \tag{4.7}$$

with

$$\zeta = \frac{e^2 m^*}{\pi \varepsilon_0 \varepsilon_r \hbar^2 \sqrt[3]{(3\pi^5 n_e)}} \quad (4.8)$$

Here, ε_r is the relative permittivity, Z is the relative charge of the ionized impurity, and n_I is the density of the ionized scattering center. $\hbar$ is the reduced Planck constant. We calculated μ_I, assuming that free electrons are generated entirely from substitutional oxygen (*i.e.*, Z = 1 and $n_I = n_e$). In addition, we took account of the n_e dependence of m^*: this is given by Eq. (4.4) (see section 4.4.1). We incorporated Eq. (4.4) into Eqs. (4.6) and (4.8) in order to calculate theoretical μ_I. The μ_I curve is shown in Figure 4.9(b). The μ_H values for the epitaxial films agree well with the theoretical curve, indicating that the most dominant scattering mechanism is the ionized impurity scattering. That is, oxygen unintentionally incorporated into Zn_3N_2 acts as an ionized impurity scattering center and governs the electron transport in the epitaxial films.

As for the polycrystalline films, μ_H values show a significant departure from the theoretical curve. This implies that additional scattering mechanisms should be considered. In general, Hall mobility μ_H in polycrystalline materials is known to be degraded substantially from the intrinsic value by scattering due to the grain boundaries. We calculated optical mobilities (μ_{opt}) as intra-grain mobilities by using $m^*(n_e)$, optically determined τ, and ω_p through the formula:

$$\mu_{opt} = \frac{e}{m^*(n_e)}\tau \quad (4.9)$$

It is reasonable to think that μ_{opt} represents the intra-grain mobility. This is justified by estimating a mean free path (l_e) using the optically obtained τ value. In the free electron model, l_e is defined as $l_e = v_F\tau = (3\pi n_e)^{1/3}\tau$ (v_F is the Fermi velocity) [48]. The values of l_e were estimated to be ~6 nm for all the films. The estimated l_e values were much smaller than the grain size of the polycrystalline films (~100 nm: see Figure 4.3), indicating that the contribution of the grain boundary scattering is negligible for electrons controlling optical response.

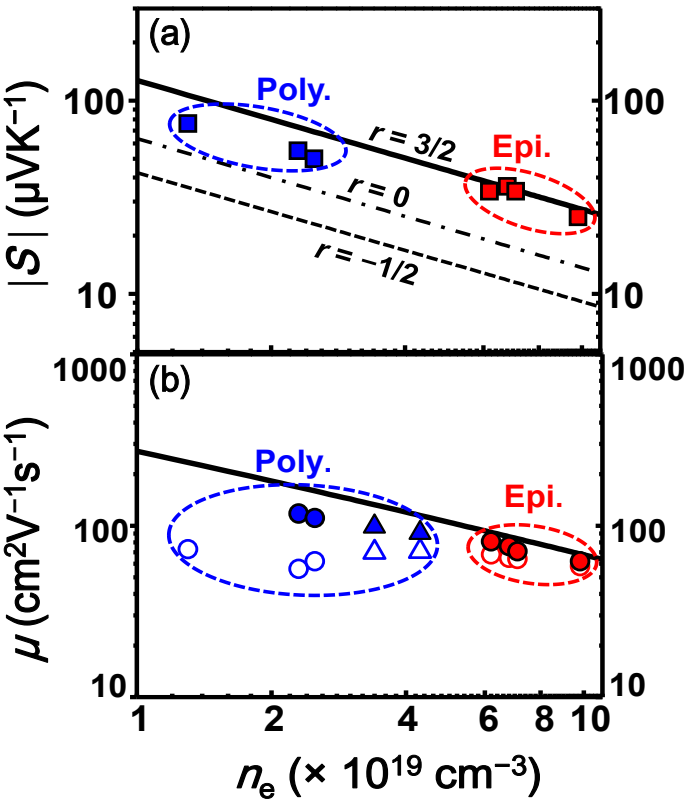

Figure 4.9. (a) Absolute value $|S|$ of Seebeck coefficient for polycrystalline and epitaxial films as a function of carrier density n_e. Theoretical lines for r = 3/2 (solid line), 0 (dash dot line), −1/2 (dashed line) are also included. (b) Plots of intra-grain mobility μ_{opt} (closed circles) and Hall mobility μ_H (open circles) as a function of carrier density n_e. The solid curve represents the theoretical mobility due to ionized impurity scattering.

The calculated μ_{opt} values are plotted in Figure 4.9(b) (closed marks). It should be noted that μ_{opt} values are significantly higher than μ_H for polycrystalline films. This indicates that the DC electron transport in the polycrystalline films is substantially impeded by scattering at the grain boundaries. In contrast, μ_{opt} values similar to μ_H values were obtained for the epitaxial films, indicating that the grain boundary scattering hardly affects DC electron transport in the epitaxial films. The intra-grain μ_{opt} for the polycrystalline films shows n_e dependence similar to the theoretical curve, suggesting that ionized impurity scattering is one of the dominant scattering mechanisms in the individual crystalline grains. Nevertheless, the values of the intra-grain μ_{opt} are still lower than the theoretical curves.

This suggests that a certain number of scattering centers, in addition to the ionized impurity, are present in the crystalline grains. The polycrystalline films have poor crystallinity as shown in Figure 4.1(a), so that high-density defects, including neutral impurities, vacancies, and dislocations, are expected to exist in the individual grains. Thus, we speculate that those defects behave as scattering centers in the polycrystalline films. Although further study on the additional scattering centers is still necessary, it should be emphasized again that high DC mobility (> 60 $cm^2\ V^{-1}\ s^{-1}$) is achievable in Zn_3N_2 polycrystalline films from the benefits of small electron effective mass. The high electron mobility in low temperature-deposited polycrystalline films is a unique feature that polycrystalline films of III-nitride semiconductors do not possess.

4.4.3 Comparison of Electron Mobility

In this section, we compare the electron mobilities of Zn_3N_2 films with those of other semiconductors including ZnO, GaN, and InN.

InN epitaxial films with n_e on the order of 10^{19} cm^{-3} have μ_H values exceeding 200 $cm^2\ V^{-1}\ s^{-1}$ which is 3–4 times as large as those of the Zn_3N_2 epitaxial films in this study [49-52]. The higher μ_H values in InN may largely come from larger static dielectric constant (ε_r ~11) of InN. As seen from Eq. 4.6, ionized impurity scattering limited mobility, μ_I, is proportional to the square value of ε_r. That is, large ε_r has beneficial effect in the reduction of the long-range coulomb potential which ionized impurities make. The square value of ε_r for InN is ~121, whereas that value for Zn_3N_2 is ~28 which is approximately quarter of the InN value. In addition, n_e dependence of m_e^* in InN is so weak that m_e^* remains a small value of $0.15m_0$ even when n_e increased up to ~5×10^{19} cm^{-3} [50]. The larger μ_H values in InN can be explained in terms of the large ε_r and small m_e^*.

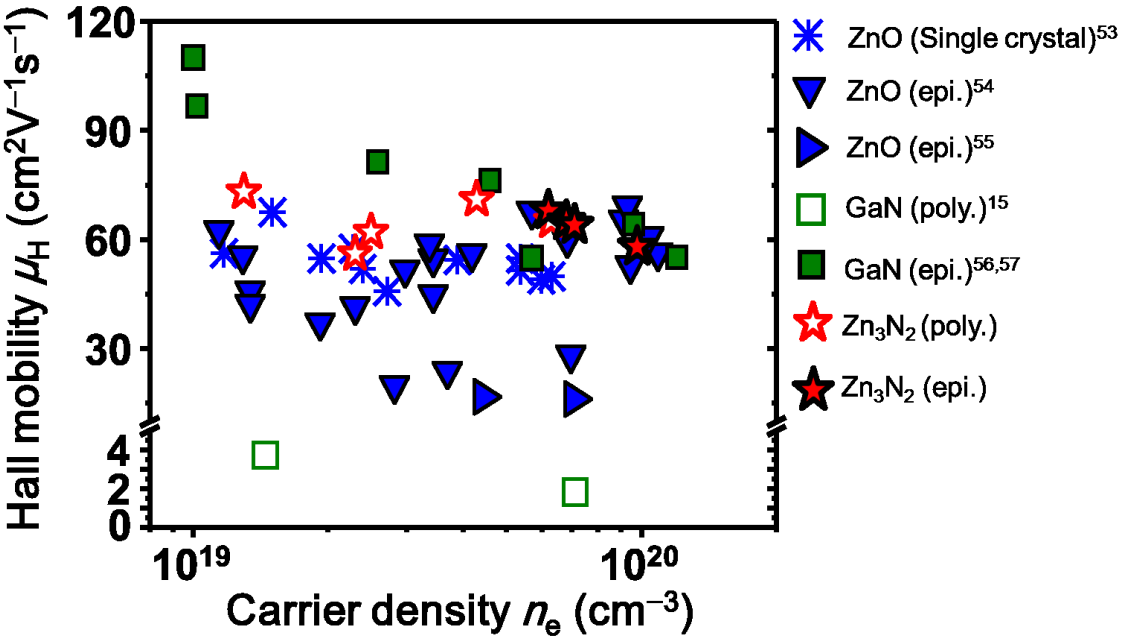

Figure 4.10. Hall mobility as a function of carrier density for different semiconductors (ZnO, GaN and Zn_3N_2). Experimental mobilities have been reported for ZnO single crystals [53] and epitaxial films (triangles) [54-55], polycrystalline GaN films (open square) [15] and epitaxial GaN films (solid squares) [56-57]. The mobility values of our Zn_3N_2 films are shown as stars.

Figure 4.10 plots μ_H of Zn_3N_2 films together with those of *n*-type ZnO and GaN, as functions of n_e. Zn_3N_2 epilayers show μ_H values comparable to those in ZnO epitaxial films, which have been known as one of high mobility semiconductors. Moreover, Zn_3N_2 epitaxial films have μ_H values similar to those of degenerate GaN epilayers which were grown by sophisticated methods using GaN [56] or AlN [57] buffer layers. We think that this is notable because detailed optimization of the growth conditions of Zn_3N_2 epitaxial films has not been established yet. Surprisingly, the μ_H values of Zn_3N_2 polycrystalline films are almost equivalent to those of ZnO single crystals [53], even though those polycrystalline films contain many defects and grain boundaries. Therefore, we believe that Zn_3N_2 can be regarded as a high mobility Zn-based compound semiconductor. If high quality Zn_3N_2 epitaxial films with n_e lower than 10^{19} cm^{-3} can be grown, much higher μ_H

would be attained.

In general, polycrystalline films of semiconductors exhibit μ_H values substantially lower than those in the epitaxial films. For example, the μ_H values of GaN polycrystalline films are only a few $cm^2\ V^{-1}\ s^{-1}$[15], which are 20 times lower than those of GaN epitaxial films. On the contrary, such a degradation of μ_H did not occur in Zn_3N_2 films: the polycrystalline films of Zn_3N_2 have high μ_H values as well. This is a striking feature as compared with GaN.

4.5 Summary

Zn_3N_2 thin films were grown on YSZ(100) under various growth conditions. By adjusting the growth condition, we grew polycrystalline and epitaxial films of Zn_3N_2 on YSZ(100). All the films were confirmed to be unintentionally doped with oxygen. As a result, the films had degenerate conduction electron gas with n_e higher than 10^{19} cm^{-3}. The polycrystalline films had n_e values in the range of 1.3–2.5 × 10^{19} cm^{-3}, while the epitaxial films had n_e values in the range of 6.2–9.8 × 10^{19} cm^{-3}. The difference in n_e was a result of different oxygen concentrations in the films. Surprisingly, DC-measured μ_H values in the polycrystalline films were comparable to or higher than those in the epitaxial films. The highest μ_H value of 73 $cm^2\ V^{-1}\ s^{-1}$ was obtained for the polycrystalline films with an n_e value of 1.3 × 10^{19} cm^{-3}.

We analyzed their electronic transport mechanisms by using DC and optical techniques in order to clarify the reason why such a high μ_H is achievable in Zn_3N_2 films. Electron density dependence on the electron effective mass $m^*(n_e)$ was determined using the classical Drude dielectric function. We found that $m^*(n_e)$ decreases with decreasing n_e; this was attributable to the nonparabolicity of the conduction band. Using a nonparabolic conduction band model, the m^* at the bottom of the conduction band was derived to be (0.08 ± 0.03) m_0, which is as small as that in InN. We also analyzed the electron mobility

and Seebeck coefficient in detail. Electron transport in the epitaxial films was found to be governed solely by ionized impurity scattering. On the other hand, in the polycrystalline films, scattering at the grain boundaries and ionized impurity scattering were revealed to mainly dominate electron transport. Even though electron transport across the grains in the polycrystalline films is impeded by the grain boundary scattering, high μ_H values were achievable. Intra-grain mobility μ_{opt} higher than 110 $cm^2\ V^{-1}\ s^{-1}$ was observed in the polycrystalline films, which is due to the small $m^*(n_e)$. Therefore, we concluded that high μ_H in Zn_3N_2 is largely due to the high μ_{opt}. The achievability of high electron mobility makes this material attractive for applications in large-area polycrystalline semiconductor devices, such as thin-film transistors and solar cells.

4.6 Bibliography

[1] C. Wang, Z. G. Ji, , K. Liu, Y. Xiang, and Z. Z. Ye, *p*-Type ZnO thin films prepared by oxidation of Zn_3N_2 thin films deposited by DC magnetron sputtering, *J. Gryst. Growth* **259**, p. 279 (2003).

[2] M. Bär, K. S. Ahn, S. Shet, Y. Yan, L. Weinhardt, O. Fuchs, M. Blum, S. Pookpanratana, K. George, W. Yang, J. D. Denlinger, M. Al-Jassim, and C. Heske, Impact of air exposure on the chemical and electronic structure of ZnO:Zn_3N_2 thin films, *Appl. Phys. Lett.* **94**, p. 012110 (2009).

[3] N. Pereira, L. C. Klein, and G. G. Amatucci, The Electrochemistry of Zn_3N_2 and LiZnN: A lithium reaction mechanism for metal nitride electrodes, *J. Electrochem. Soc.* **149**, p. A262 (2002).

[4] A. Trapalis, J. Heffernan, I. Farrer, J. Sharman, and A. Kean, Structural, electrical, and optical characterization of as grown and oxidized zinc nitride thin films, *J. Appl. Phys.* **120**, p. 205102 (2016).

[5] M. A. Dominguez, J. L. Pau, M. Gómez-Castaño, J. A. Luna-Lopez, and P. Rosales, High mobility thin film transistors based on zinc nitride deposited at room temperature, *Thin Solid Films* **619**, p. 261 (2016).

[6] M. G. Castaño, A. R. Cubero, L. Vazquez, and J. L. Pau, Analysis of zinc nitride resistive indicators under different relative humidity conditions, *ACS Appl. Mater. Interfaces* **8**, p. 29163 (2016).

[7] P. Wu, T. Tiedje, H. Alimohammadi, V. Bahrami-Yekta, M. Masnadi-Shirazi, and C. Wang, Molecular beam epitaxy growth and optical properties of single crystal Zn_3N_2 films, *Semicond. Sci. Technol.* **31**, p. 10LT01 (2016).

[8] N. Yamada, K. Watarai, T. Yamaguchi, A. Sato, and Y. Ninomiya, Transparent conducting zinc nitride films, *Jpn. J. Appl. Phys.* **53**, p. 05FX01 (2014).

[9] E. Lee, A. Benayad, T. Shin, H. Lee, D. S. Ko, T. S. Kim, K. S. Son, M. Ryu, S. Jeon, and G. S. Park, Nanocrystalline ZnON; high mobility and low band gap semiconductor material for high performance switch transistor and image sensor application, *Sci Rep.* **4**, p. 4948 (2014).

[10] S. H. Yoo, A. Walsh, D. O. Scanlonc, and A. Soon, Electronic structure and band alignment of zinc nitride, Zn_3N_2, *RSC Adv.* **4**, p. 3306 (2014).

[11] T. Wen, (2014) *Fabrication of zinc nitride thin films using RF magnetron sputtering deposition for optoelectronic applications* (Doctoral Dissertation), Ohio. Retrieved from http://utdr.utoledo.edu/cgi/viewcontent.cgi?article=1490&context=theses-dissertations

[12] X. Cao, A. Sato, Y. Ninomiya, and N. Yamada, Oxygen-doped zinc nitride as a high-mobility nitride-based semiconductor, *J. Phys. Chem. C* 119, p. 5327 (2015).

[13] M. Futsuhara, K. Yoshioka, and O. Takai, Structural, electrical and optical properties of zinc nitride thin films prepared by reactive RF magnetron sputtering. *Thin Solid Films* **322**, p. 274 (1998).

[14] C. G. Núñez, J. L. Pau, M. J. Hernández, M. Cervera, E. Ruiz, and J. Piqueras, On the zinc nitride properties and the unintentional incorporation of oxygen, *Thin Solid Films* **520**, p. 1924 (2012).

[15] H. Sato, T. Minami, E. Yamada, M. Ishii, and S. Takata, Transparent and conductive impurity-doped GaN thin films prepared by an electron cyclotron resonance plasma metalorganic chemical vapor deposition method. *J. Appl. Phys.* **75**, p. 1405 (1994).

[16] M. A. Qaeed, K. Ibrahim, K. M. A. Saron, M. A. Ahmed, and Nageh K. Allam, Low-temperature solution-processed flexible solar cells based on (In,Ga)N nanocubes, *ACS Appl. Mater. Interfaces*. **6**, p. 9925 (2014).

[17] M. Yoshimoto, H. Yamamoto, W. Huang, H. Harima, J. Saraie, A. Chayahara, and Y. Horino, Widening of optical bandgap of polycrystalline InN with a few percent incorporation of oxygen, *Appl. Phys. Lett.* **83**, p. 3480 (2003).

[18] N. K. Jiang, J. L. Roehl, S. V. Khare, D. G. Georgiev, and A. H. Jayatissa, An *ab initio* computational study of pure Zn_3N_2 and its native point defects and dopants Cu, Ag and Au. *Thin Solid Films* **564**, p. 331 (2014).

[19] K. Kuriyama, Y. Takahashi, and F. Sunohara, Optical band gap of Zn_3N_2 films, *Phys Rev B* **48**, p. 2781 (1993).

[20] T. L. Yang, Z. S. Zhang, Y. H. Li, M. S. Lv, S. M. Song, Z. C. Wu, J. C. Yan, and S. H. Han, Structural and optical properties of zinc nitride films prepared by rf magnetron

sputtering, *Appl. Surf. Sci.* **255**, p. 3544 (2009).

[21] G. Z. Xing, D. D. Wang, B. Yao, L. F. N. Ah Qune, T. Yang, Q. He, J. H. Yang, and . L. Yang, Structural and electrical characteristics of high quality (100) orientated-Zn_3N_2 thin films grown by radio-frequency magnetron sputtering. *J. Appl. Phys.* **108**, p. 083710 (2010).

[22]N. K. Jiang, D. G. Georgiev, A. H. Jayatissa, R. W. Collins, J. Chen, and E. McCullen, Zinc nitride films prepared by reactive RF magnetron sputtering of zinc in nitrogen-containing atmosphere. *J. Phys. D: Appl. Phys.* **45**, p. 135101. (2012).

[23] R. Ayouchi, C. Casteleiro, L. Santos, and R. Schwarz, RF-plasma assisted PLD growth of Zn_3N_2 thin films. *Phys. Status Solidi C.* **7**, p. 2294 (2010).

[24] T. Suda and K. Kakishita, Bandgap energy and electron effective mass of polycrystalline Zn_3N_2, *J. Appl. Phys.* **99**, p. 076101 (2006).

[25] T. Oshima and S. Fujita, (111)-Oriented Zn_3N_2 growth on *a*-plane sapphire substrates by molecular beam epitaxy, *Jpn. J. Appl. Phys.* **45**, p. 8653 (2006).

[26] E. Maile, and R. A. Fischer, MOCVD of the cubic zinc nitride phase, Zn_3N_2, using $Zn[N(SiMe_3)_2]_2$ and ammonia as precursors, *Chem. Vap. Deposition* **11**, p. 409 (2005).

[27] K. Toyoura, H. Tsujimura, T. Goto, K. Hachiya, R. Hagiwara, R. And Y. Ito, Optical properties of zinc nitride formed by molten salt, electrochemical process. *Thin Solid Films* **492**, p. 88 (2005).

[28] J. H. Hildebrand, The vapor pressures of liquid metals, *J. Am. Chem. Soc.* **40**, p. 45 (1918).

[29] F. J. Zong, H. L. Ma, W. Liang, W. Du, X. J. Zhang, H. D. Xiao, J. Ma, F. Ji, C. S. Xue, and H. Z. Zhuang, Thermal decomposition behaviour of Zn_3N_2 Powder, *Chinese Phys. Lett.* **22**, p. 907 (2005).

[30] R. Long, Y. Dai, L. Yu, M. Guo, and B. B. Huang, Structural, electrical, and optical properties of oxygen defects in Zn_3N_2, *J. Phys. Chem. B* **111**, p. 3379 (2007).

[31] C. S. Gallinat, G. Koblmüller, and J. S. Speck, The role of threading dislocations and unintentionally incorporated impurities on the bulk electron conductivity of In-face InN, *Appl. Phys. Lett.* **95**, p. 022103 (2009).

[32] VC. G. Van de Walle, J. L. Lyons, and A. Janotti, Controlling the conductivity of InN, *Phys. Status Solidi A* **207**, p. 1024 (2010).

[33] J. F. Moulder, W. F. Stickle, P. E. Sobol, and K. D. Bomben, *Handbook of X-ray Photoelectron Spectroscopy*, Physical Electronics Inc., Minnesota, USA, 1995.

[34] C. Skierbiszewski, P. Perlin, P. Wisniewski, W. Knap, T. Suski, W. Walukiewicz, W. Shan, K. M. Yu, J. W. Ager, E. E. Haller, J. F. Geisz, and J. M. Olson, Large, nitrogen-induced increase of the electron effective mass in $In_yGa_{1-y}N_xAs_{1-x}$, *Appl. Phys. Lett.* **76**, p. 2409 (2000).

[35] C. P. Foley, and T. L. Tansley, Pseudopotential band structure of indium nitride, *Phys. Rev. B* **33**, p. 1430 (1986).

[36] D. M. Szmyd, P. Porro, A. Majerfeld, and S. Lagomarsino, Heavily doped GaAs:Se. I. Photoluminescence determination of the electron effective mass, *J. Appl. Phys.* **68**, p. 2367 (1990).

[37] W. G. Spitzer, and H. Y. Fan, Determination of Optical Constants and Carrier Effective Mass of Semiconductors, *Phys. Rev.* **106**, p. 882 (1957).

[38] Y. Furubayashi, N. Yamada, Y. Hirose, Y. Yamamoto, M. Otani, T. Hitosugi, T, Shimada, and T. Hasegawa, Transport properties of d-electron-based transparent conducting oxide: Anatase $Ti_{1-x}Nb_xO_2$, *J. Appl. Phys.* **101**, p. 093705 (2007).

[39] T. Minami, H. Sato, K. Ohashi, T. Tomofuji, and S. Takata, Conduction mechanism of highly conductive and transparent zinc oxide thin films prepared by magnetron sputtering, *J. Cryst. Growth* **117**, p. 370 (1992).

[40] H. Fujiwara, and M. Kondo, Effects of carrier concentration on the dielectric function of ZnO:Ga and In_2O_3:Sn studied by spectroscopic ellipsometry: Analysis of free-carrier and band-edge absorption, *Phys. Rev. B* **71**, p. 75109 (2005).

[41] J. S. Kim, J. H. Jeong, J. K. Park, Y. J. Baik, I. H. Kim, T. Y. Seong, and W. M. Kim, Optical analysis of doped ZnO thin films using nonparabolic conduction-band parameters, *J. Appl. Phys.* **111**, p.123507 (2012).

[42] X. Wu, T. J. Coutts, and W. P. Mulligan, Properties of transparent conducting oxides formed from CdO and ZnO alloyed with SnO_2 and In_2O_3, *J. Vac. Sci. Technol. A* **15**, p.1057

(1997).

[43] T. Pisarkiewicz, K. Zakrzewska, and E. Leja, Scattering of charge carriers in transparent and conducting thin oxide films with a non-parabolic conduction band, *Thin Solid Films* **174**, p. 217 (1989).

[44] M, Goiran, M. Millot, J. M. Poumirol, I. Gherasoiu, W. Walukiewicz, and J. Leotin, Electron cyclotron effective mass in indium nitride, *Appl. Phys. Lett.* **96**, p. 052117 (2010).

[45] M. Millot, N. Ubrig, J. M. Poumirol, I. Gherasoiu, W. Walukiewicz, S. George, O. Portugall, J. Léotin, M. Goiran, and J. M. Broto, Determination of effective mass in InN by high-field oscillatory magnetoabsorption spectroscopy, *Phys. Rev. B* **83**, p. 125204 (2011).

[46] K. Seeger, *Semiconductor Physics; An Introduction*, Springer, New York, 2011.

[47] D. S. Ginley, H. Hosono, and D. C. Paine, *Handbook of Transparent Conductors*, Springer, New York, USA, 2010.

[48] C. Kittel, *Introduction to Solid State Physics*, Wiley, New York, 1986.

[49] A. Yamamoto, T. Shin-ya, T. Sugiura, and A. Hashimoto, Determination of effective mass in InN by high-field oscillatory magnetoabsorption spectroscopy, *J. Cryst. Growth* **189/190**, p. 461 (1998).

[50] B. R. Nag, Electron mobility in indium nitride, *J. Cryst. Growth* **269**, p. 35 (2004).

[51] L. Hsu, R. E. Jones, S. X. Li, K. M. Yu, and W. Walukiewicz, Electron mobility in InN and III-N alloys, *J. Appl. Phys.* **102**, p. 073705 (2007).

[52] N. Khan, A. Sedhain, J. Li, J. Y. Lin, and H. X. Jiang, High mobility InN epilayers grown on AlN epilayer templates, *Appl. Phys. Lett.* **92**, p. 172101 (2008).

[53] K. Ellmer, and R. Mientus, Carrier transport in polycrystalline ITO and ZnO:Al II: The influence of grain barriers and boundaries, *Thin Solid Films* **516**, p. 5829 (2008).

[54] M. Lorenz, E. M. Kaidashev, H. von Wenckstern, V. Riede, C. Bundesmann, D. Spemann, G. Benndorf, H. Hochmuth, A. Rahm, H.-C. Semmelhack, and M. Grundmann, Optical and electrical properties of epitaxial $(Mg,Cd)_xZn_{1-x}O$, ZnO, and ZnO:(Ga,Al) thin films on c-plane sapphire grown by pulsed laser deposition, *Solid-State Electronics* **47**, p.

2205 (2003).

[55] T. Makino, Y. Segawa, A. Tsukazaki, A. Ohtomo, and M. Kawasaki, Electron transport in ZnO thin films, *Appl. Phys. Lett.* **87**, p. 2003 (2005).

[56] S. Fritze, A. Dadgar, H. Witte, M. Bügler, A. Rohrbeck, J. Bläsing, A. Hoffmann, and A. Krost, High Si and Ge *n*-type doping of GaN doping - Limits and impact on stress, *Appl. Phys. Lett.* **100**, p. 122104 (2012).

[57] P. R. Hageman, W. J. Schaff, J. Janinski, and Z. Liliental-Weber, *n*-Type doping of wurtzite GaN with germanium grown with plasma-assisted molecular beam epitaxy, *J. Crys. Growth* **267**, p. 123 (2004).

Chapter 5

Preparation, Characterization, Analysis of $ZnSnN_2$ Thin Films

Nothing is too wonderful to be true, if it be consistent with the laws of nature.

—Michael Faraday

5.1 Background and Objective

To meet the world economic growth demand by 2050, it requires over 20 TW (10^{12} W) new power instead of fossil fuel to maintain the atmosphere CO_2 concentrations at their current level [1]. Solar photovoltaics are considered as one of the most promising options for a low-carbon future [1-3]. Besides the silicon-based PVs, aggressive development of non-silicon-based PV materials, such as CdTe and $CuInGaSe_2$ (CIGS) has greatly inspired confidence in reducing PV module price per watt by increasing the photoelectric conversion efficiency or/and using inexpensive materials [4]. For example, the CdTe and CIGS technologies are still suffering serious problems of toxicity (Cd) or rarity (Te ~ 0.005 ppm, In ~ 0.048 ppm, and Se ~ 0.05 ppm) for TW-scale deployment [5-6]. Moreover, even the CIGS represents one of the current cost-competitive alternatives to silicon and a bandgap tunability through alloying, however, CIGS is economical only in polycrystalline from, making it unsuitable for solid-state lighting devices, where InGaN dominates. Both CIGS and InGaN system contain indium, which is an expensive element

with price fluctuations exceeding an order of magnitude over the past decade [7] . Thus, it becomes more and more imperative to develop new PV technology and solid-state lighting based on environmentally friendly materials which are earth-abundant (*i.e.*, new-generation earth-abundant solar PV and SSL).

5.2 Preparation Details for Epitaxial $ZnSnN_2$ Thin Films

5.2.1 Growth of $ZnSnN_2$ Thin Films

During the process of writing up this dissertation, in terms of $ZnSnN_2$ thin film deposition only a few literature has been reported. Veal *et al.* [8] employed N-plasma-assisted MBE technique to grown epitaxial $ZnSnN_2$ thin films on single-crystal YSZ(111) substrates with different nominal Zn:Sn flux ratios. Lahourcade *et al.* [9] applied reactive RF magnetron sputtering technique to obtain their experimentally stoichiometric $ZnSnN_2$ films. In the initial exploration of $ZnSnN_2$ sputter deposition, it was absolutely important to ensure that the desired stoichiometry could be achieved. Two different methods of deposition were expected: sputtering from a single mixed Zn_xSn_{1-x} target and simultaneously sputtering from elemental zinc and tin targets. In our current work, we used the former method to deposit $ZnSnN_2$ thin films, while the latter is our next step in our future work.

$ZnSnN_2$ thin films were grown on YSZ(111) single-crystal substrates with substrate temperatures ranging from 250−350 °C by the reactive RF magnetron sputtering deposition technique. A disk of metal $Zn_{0.5}Sn_{0.5}$ was used as the target (a diameter of 10 cm and purity of 99.9%). An RF power of 70 W was applied to the Zn target. A base pressure lower than 2×10^{-4} Pa was established in the growth chamber before the film growth. The substrates were ultrasonically degreased in methanol for 5 min, and then in acetone for 5 min, and one more time in methanol for 5 min. At last, they were dried with nitrogen gas blowing. Sputtering was conducted in a gas mixture consisting of Ar (99.999% pure) and N_2

(99.9995% pure) at a total pressure of 2 Pa. Each gas was introduced into the growth chamber by using a mass flow controller. Thin films were grown under various atmospheres with $f(N_2)$ [$f(N_2) = N_2/(Ar+N_2)$] ranging from 50%–100%, at an interval of 10%. Prior to the growth, the target surface was sputter-etched with pure Ar for 30 min and was subsequently pre-sputtered for 10 min under the same condition with the film growth. The growth time was adjusted to obtain a thin film with a thickness of 100–300 nm. After the film growth, the films were immediately stored in another vacuum chamber (the pressure was about 1 Pa) for subsequent measurements.

5.2.2 Characterizations of $ZnSnN_2$ Thin Films

The structure and phase composition of as-deposited $ZnSnN_2$ films were determined by X-ray diffraction (XRD) measurements using an X-ray diffractometer equipped with a Cu Kα source (Rigaku ATX-G). For epitaxial films, besides the conventional θ–2θ mode scan, a $2\theta\chi$-φ–scan mode was also performed to examine the in-plane relationship between epitaxial films and YSZ(111) substrates. The determination of the chemical state and composition of the films was conducted by an XPS (PHI Versa Probe) instrument with monochromated Al Kα (hv = 1486.6 eV) radiation. XPS was performed on both as-deposited and 2 min Ar^+-sputtered-surface films. The latter was carried out by the sputter-etching using an Ar^+-gun with an ion energy of 4 keV and emission current of 7 mA, with a raster size of 3 × 3 mm^2. The semi-quantitative evaluation of XPS signals was done by an XPS peak fitting program, namely, XPSPEAK 4.1 software. The Shirley algorithm, the most widely used background subtraction method, was chosen for the background subtraction before entering the fit iterations. The peak shapes were typically determined by using Gaussian-Lorentzian sum function, and a linear least squares curve fitting procedure was adopted to fit the spectra. The van der Pauw method (with a 1 mA source current) was utilized to measure electrical resistivity (ρ). Hall effect measurements in the van der Pauw configuration (Toyo Corp. Resitest 8200) were employed to detect electron density (n_e) and Hall mobility (μ_H). Magnetic fields of ± 1 T were applied normal

to the film surface. For selected samples, temperature dependence of ρ, n_e , and μ_H were also measured for temperatures ranging from 77 to 300 K. A temperature gradient (usually chosen to be less than 5 K) was provided using a Manganin wire heater, and the temperatures at the cold and hot ends were measured with a calibrated K-type thermocouple. The thermovoltages were recorded with a digital multimeter (Keithley 2000). Electron transport measurements were all carried out at room temperature. Optical transmittance and reflectance in the ultraviolet to near-infrared region (in a wavelength range of 190–3200 nm) were measured using a spectrometer (Shimadzu UV-3150). We also measured infrared transmittance at normal incidence and reflectance at near-normal incidence (~5°) in a wavenumber range of 1000–4600 cm^{-1} were measured by using a Fourier transform infrared (FTIR) spectrophotometer (Shimadzu IRAffinity-1). All measurements were performed within a day after the film growth to minimize film oxidation and/or hydroxylation.

5.3 Results for Growth and Characterizations of $ZnSnN_2$ Films

5.3.1 Epitaxial Thin Film Growth

Due to the fact that the composition of our sputter target is fixed ($Zn_{0.5}Sn_{0.5}$), the growth temperature and reactive sputtering gas nitrogen turn into two key factors influencing the epitaxial film growth. Figure 5.1 depicts the phase diagram for $ZnSnN_2$ thin films grown on single-crystal YSZ(111) substrates, as functions of substrate temperature T_s and nitrogen partial pressure $P(N_2)$.

As can be seen in Figure 5.1, epitaxial growth region for the case of $ZnSnN_2$ thin films, *i.e.*, the shadowed orthogonal purple region, is relatively narrow. Hereafter, we refer to the shadowed region in Figure 5.1 as the epitaxial region. Epitaxial growth of $ZnSnN_2$ thin films usually needs suitable temperature and appropriate nitrogen proportion. The proper

growth temperature for our deposition condition is about 300 °C and appropriate nitrogen proportion is nitrogen-rich. Lower temperature or nitrogen-poor bring about either polycrystalline $ZnSnN_2$ thin films or secondary phases such as Zn, Sn metals.

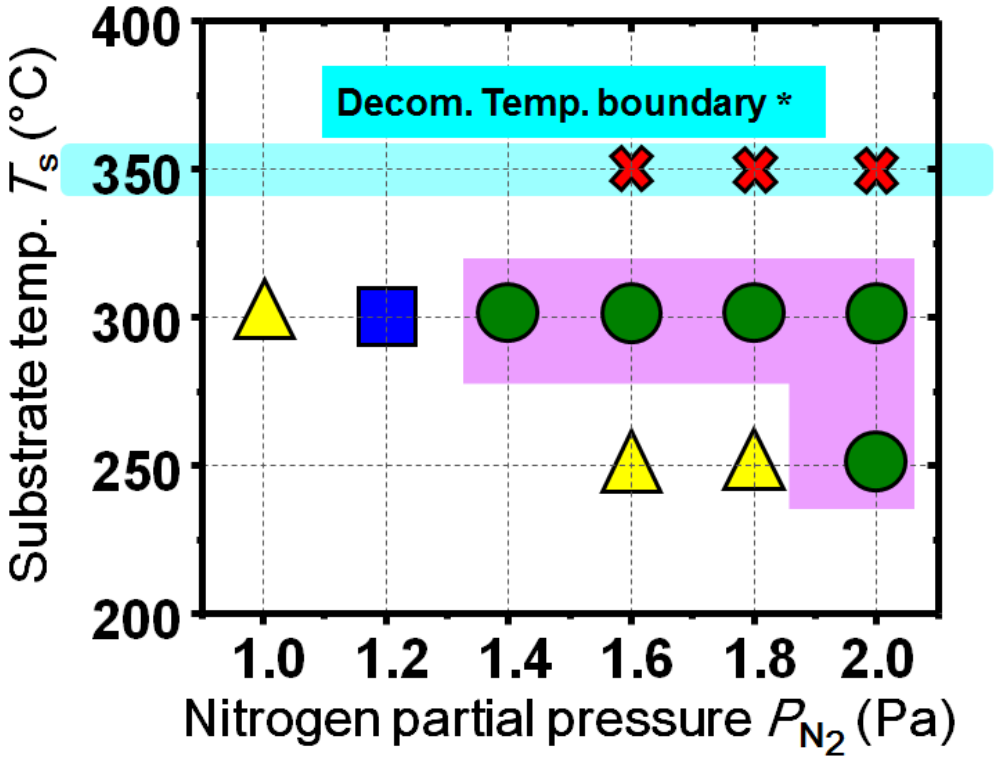

Figure 5.1. Phase diagram of $ZnSnN_2$ thin films on single-crystal yttria-stabilized zirconia (111) substrates as functions of substrate temperature T_s and nitrogen partial pressure $P(N_2)$ growth parameter: crosses, circles, triangles, and squares denote $ZnSnN_2$ film decomposition, epitaxial $ZnSnN_2$ thin films, polycrystalline $ZnSnN_2$ thin films, and unstable $ZnSnN_2$ thin films (reproducibility is difficult to control), respectively. The shadowed orthogonal purple region represents the growth condition for $ZnSnN_2$ epitaxial films, while the rectangular light blue area donates $ZnSnN_2$ film decomposition temperature boundary.

What's intriguing, when the experiment condition was T_s = 300 °C and $P(N_2)$ = 1.2, this grown $ZnSnN_2$ thin film exhibited rather unstable character, namely epitaxial growth or polycrystalline growth after we deposited for at lease six times in contrast with the other

epitaxial films or polycrystalline films, which grew stable film-form character. We can not deny that this special experimental point is truly recognized as either epitaxial one or polycrystalline one, because even though we have already tried at least six times the trial times was still rare. On the other hand, when we looked at the both sides (left side and right side) of this point, polycrystalline and epitaxial films were respectively grown, which may give us an indication that this very experimental point maybe a threshold of epitaxial growth at T_s = 300°C. Even though, because the material parameter is much more important, we also took advantage of this very point as to explain our following results and discussions. It should be noted here that, the film decomposition temperature boundary is consistent with our previous bulk study [10], indicating the decomposition temperature of grown $ZnSnN_2$ thin film is not high.

As we illustrated above, structure determination for $ZnSnN_2$ material is under controversial: cation ordered orthorhombic and cation disordered wurtzite-like structures. From the calculated X-ray powder diffraction data, the distinct differential between these two structures lies in whether the two weak peaks (110) and (011) at *ca.* 22° appear or not. The peaks at 22° is a characteristic for the orthorhombic structure. In all of our sputter-grown $ZnSnN_2$ thin films, this kind of characteristic was absent within XRD measurement limit, indicating that all of $ZnSnN_2$ samples showed cation disordered wurtzite-like structure. Our finding is in good agreement with that given in Ref. [11], where the absence of characteristic peak reflections in the pole figure. We detected all the epitaxial $ZnSnN_2$ thin films, and found that all the samples showed the similar XRD patterns.

Here we just selected one typical $ZnSnN_2$ thin film to reveal the epitaxial relationship between the grown film and substrate. Figure 5.2(a) shows the out-of-plane nature of the epitaxial film: the (002), (004) and (006) planes matched with the calculated X-ray powder diffraction data of $ZnSnN_2$ (see Figure 5.2(d), (006) plane was not simulated here); and (111), (222) and (333) lattice plane reflections of YSZ single-crystal substrate.

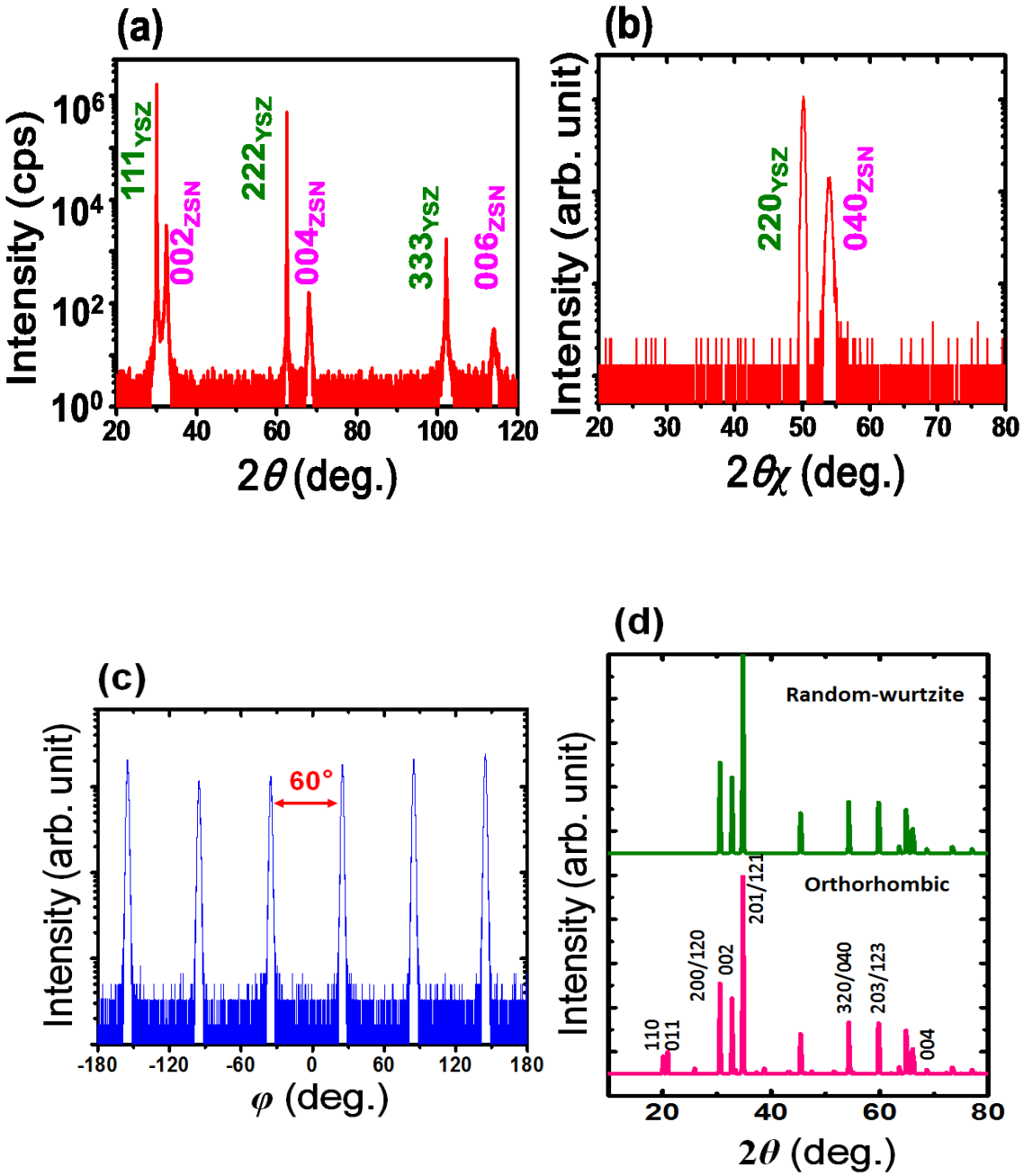

Figure 5.2. (a). θ–2θ mode scan measurements show only 002, 004, and 006 lattice plane reflections of $ZnSnN_2$ and 111, 222, and 333 lattice plane reflections of YSZ single-crystal substrate. (b) $2\theta\chi$-φ–scan mode shows the 040 lattice plane reflection of $ZnSnN_2$ and 220 lattice plane reflection of YSZ substrate. (c) A wide range 040 rocking cure reveals 6-fold rotational symmetry. (d) Simulated powder XRD patterns for random-wurtzite and orthorhombic structures of $ZnSnN_2$.

From Figure 5.2(a), the out-of-plane diffraction pattern indicates that the $ZnSnN_2$ thin film was completely (001) oriented; while the in-plane one [Figure 5.2(b)] indicates that the $ZnSnN_2$ thin film and substrate were aligned with respect to the (010) plane. A wide range 040 rocking cure revealed 6-fold rotational symmetry [Figure 5.2(c)]. Taken above-mentioned together, therefore, the $ZnSnN_2$ film was epitaxially grown on YSZ(111) with the relationship of $(001)[010]ZnSnN_2//(111)[110]_{YSZ(111)}$.

5.3.2 Surface Morphology of $ZnSnN_2$ Thin Films

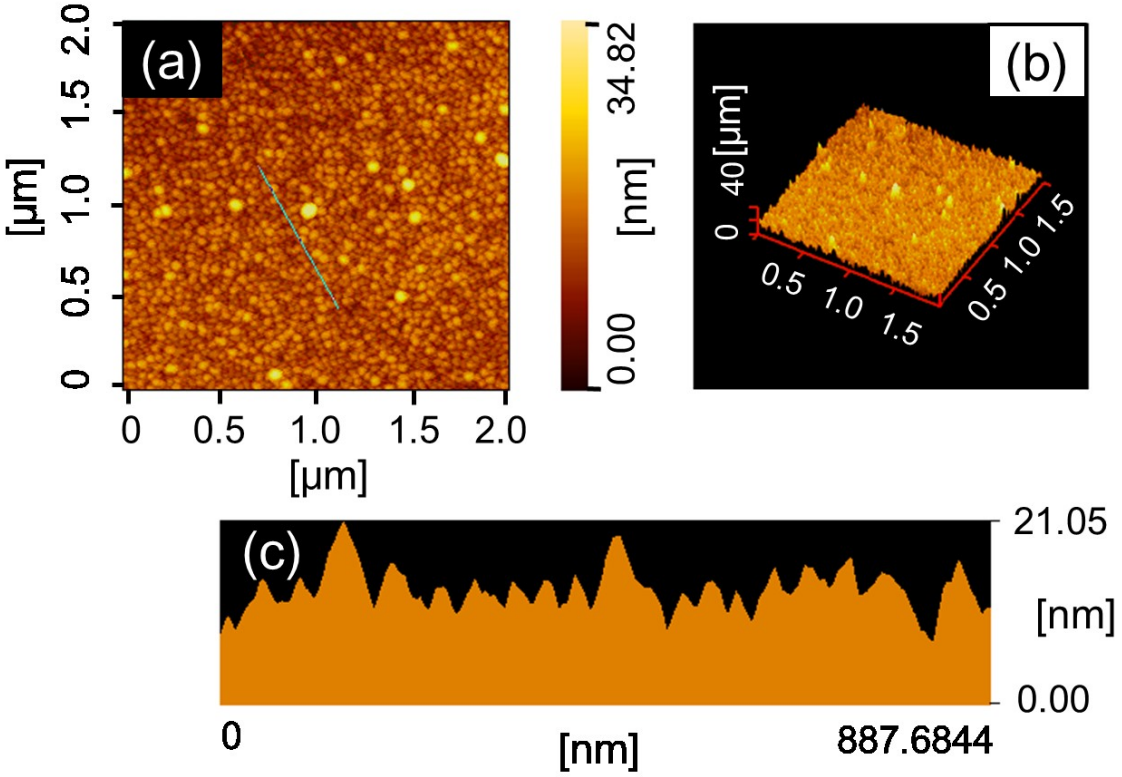

Figure 5.3. (a).A large-scale top-view AFM image of one typical epitaxial $ZnSnN_2$ thin film fabricated with nitrogen partial pressure 2.0 Pa. (b) A three-dimensional [3D] surface topology of AFM image of the same film sample (on a scale bar of 2×2 μm^2) compared to part a. (c) Cross-sectional view along the measurement line shown in part a.

In our work, AFM technique was applied to be used for quantitative determination of the surface roughnesses of all of the grown epitaxial $ZnSnN_2$ thin films. In this work, we just

selected one typical epitaxial $ZnSnN_2$ thin film to make an illustration for surface morphology of $ZnSnN_2$ thin films, which is shown in Figure 5.3.

The surface roughness of grown $ZnSnN_2$ thin films was quantitatively examined by taking advantage of AFM technique. To combine Figure 5.3(a) and 5.3(b), for a typical epitaxial $ZnSnN_2$ thin film which was grown under the experimental condition of nitrogen partial pressure of 2.0 Pa, the root-mean-square (RMS) roughness of the 2×2 μm^2 scanned area was 1.6 nm. For all of the measured epitaxial $ZnSnN_2$ thin films, the RMS roughnesses of the 2×2 μm^2 scanned area were determined to be in a range of 0.9–3.2 nm. These RMS roughnesses were relatively a little high, indicating that improved-quality of $ZnSnN_2$ thin films should be grown in the near future by using ultrahigh vacuum system matched sputtering instrument or other advanced techniques. From the cross-section profile shown in Figure 5.3(c), the lateral grain diameter was estimated to *ca.* 300 nm, which is typical for a sputtered thin film.

5.3.3 Electrical Properties of $ZnSnN_2$ Thin Films

In this part of our work, we will focus on the epitaxial $ZnSnN_2$ thin film grown at 300 °C with various nitrogen partial pressure ranging from 1.2 to 2.0 Pa. All the Hall coefficients R_H of the $ZnSnN_2$ films were always negative ($R_H < 0$), indicating that the $ZnSnN_2$ films show *n*-type conductivity. Figure 5.4(a) shows the nitrogen partial pressure P_{N_2} dependence of electron density n_e. All the films had n_e values larger than 10^{20} cm^{-3}, which were also showed in Refs. [8, 9, 12].

As seen in Figure 5.4(a), the n_e decreased with P_{N_2} increased, which gave us an indication that making the nitrogen sufficient, *i.e.*, nitrogen-rich atmosphere, could partly lower the electron density in $ZnSnN_2$ films. Such a phenomenon can also be seen in the famous semiconductor case of InN. The factor that impacted this tendency could be glanced from

Figure 5.4(b). Similar with the case of binary zinc nitride material, oxygen contamination can be easily introduced into $ZnSnN_2$ film host, hereafter inferred to as "$ZnSnN_{2-x}O_x$".

Here, we also took advantage of the RSF method to establish the ratios of X_{Zn}/X_{Sn} given by (I_{Zn}/S_{Zn}) times (S_{Sn}/I_{Sn}); the x values were given by average of X_O/X_{Zn} and X_O/X_{Sn}. The X_O/X_{Zn} equals (I_O/S_O) times (S_{Zn}/I_{Zn}) and X_O/X_{Sn} equals (I_O/S_O) times (S_{Sn}/I_{Sn}), where I_O, I_{Zn}, I_{Sn}, S_O, S_{Zn}, and S_{Sn} represent the O 1s integral intensity, Zn 2p 3/2 and Sn 3d 5/2 peaks integral intensity, respectively; RSF of O (0.711), Zn (3.354) and Sn (4.095). As a consequence, we calculated the Zn concentration in film, namely Zn/(Zn+Sn) ratio and also x values in $ZnSnN_{2-x}O_x$ films using RSF method described above. In Figure 5.4(b), Zn/(Zn+Sn) ratio kept a nearly constant *ca.* 0.55 (near the target composition value and 0.50 and stoichiometric composition) as the P_{N_2} increased; while the x values in $ZnSnN_{2-x}O_x$ films had a similar tendency with that observed trend of n_e–P_{N_2} dependence. We, therefore, understood it's the factor of oxygen impurity more than Zn/Sn off-stoichiometry that impacted the measured electron density.

Figures 5.5 show electrical properties-temperature of all sputtered epitaxial $ZnSnN_2$ thin films.

Figure 5.5(a) depicts the resistivity ρ–temperature T dependence of all sputtered epitaxial $ZnSnN_2$ thin films. The ρ–T curves exhibit nearly temperature-independent behavior; these curves have very small negative temperature coefficients, which confirmed that all of epitaxial $ZnSnN_2$ thin films served as semiconductors.

Figure 5.5(b) depicts the electron density n_e–temperature T dependence of all sputtered epitaxial $ZnSnN_2$ thin films, from which we can see that n_e are almost independent against T, indicating that all of our sputtered $ZnSnN_2$ thin films having $n_e > 10^{20}$ cm^{-3} can be identified as degenerate semiconductors. Hence, those films had degenerate conduction electrons. Such a finding is similar with that of our binary topic material: Zn_3N_2. What should be mentioned here that, as a matter of fact, for some polycrystalline and epitaxial

$ZnSnN_2$ films with $n_e > 10^{19}$ cm^{-3} also can be identified as degenerate semiconductors. Those samples are not my main focus in this part, although n_e–temperature T dependence for typical samples had been carried out, here we just skipped to show the data we had already measured. All of the experimental data provided us an information that: $ZnSnN_2$ thin films with $n_e > 10^{19}$ cm^{-3} having highly degenerate electron gas can be identified as degenerate semiconductors.

In Figure 5.5(c), Hall mobility behavior show a nearly constant value versus measured temperature, suggesting that ionized impurity scattering have a main contribution to electron transport in $ZnSnN_2$ films because electron mobility limited by the ionized impurity scattering does not depend on temperature in degenerate semiconductors, just as the case of Zn_3N_2 explained earlier in section. 3.3.3. All of the Hall mobilities were found to be *ca.* 20 cm^{2}V^{-1}s^{-1} or lower, these low values probably due in part to the small grain sizes of sputtered grown $ZnSnN_2$ thin films, as shown in Figure 5.3(c).

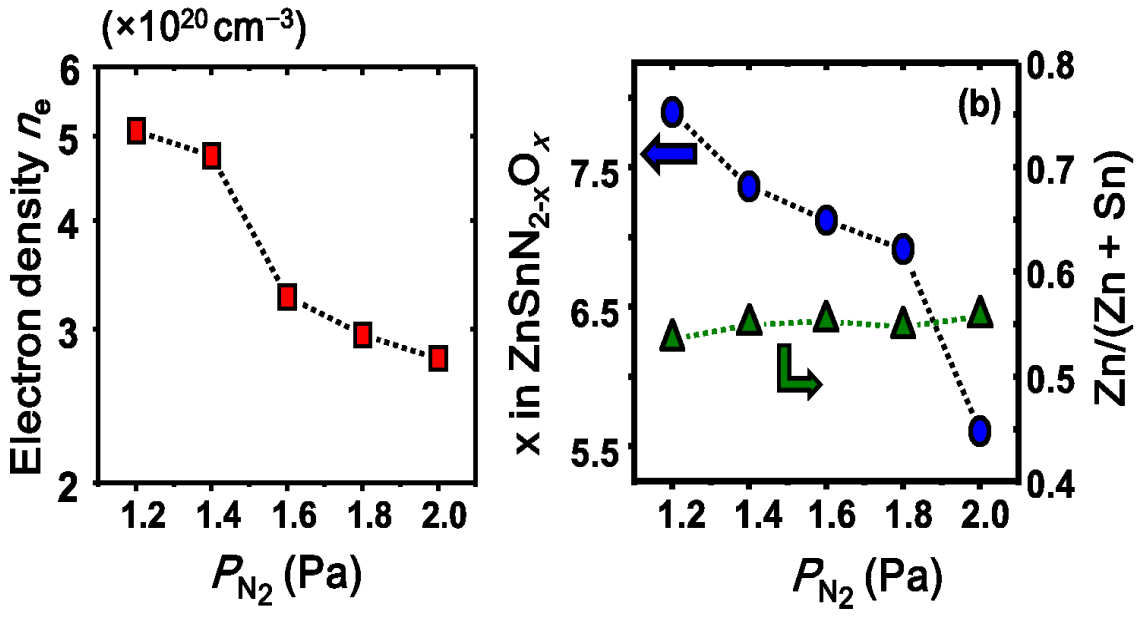

Figure 5.4. (a). Electron density n_e as a function of nitrogen partial pressure P_{N_2}. (b) Zn concentration, *i.e.*, Zn/(Zn+Sn) ratio and x in $ZnSnN_{2-x}O_x$ as functions of nitrogen partial pressure P_{N_2}.

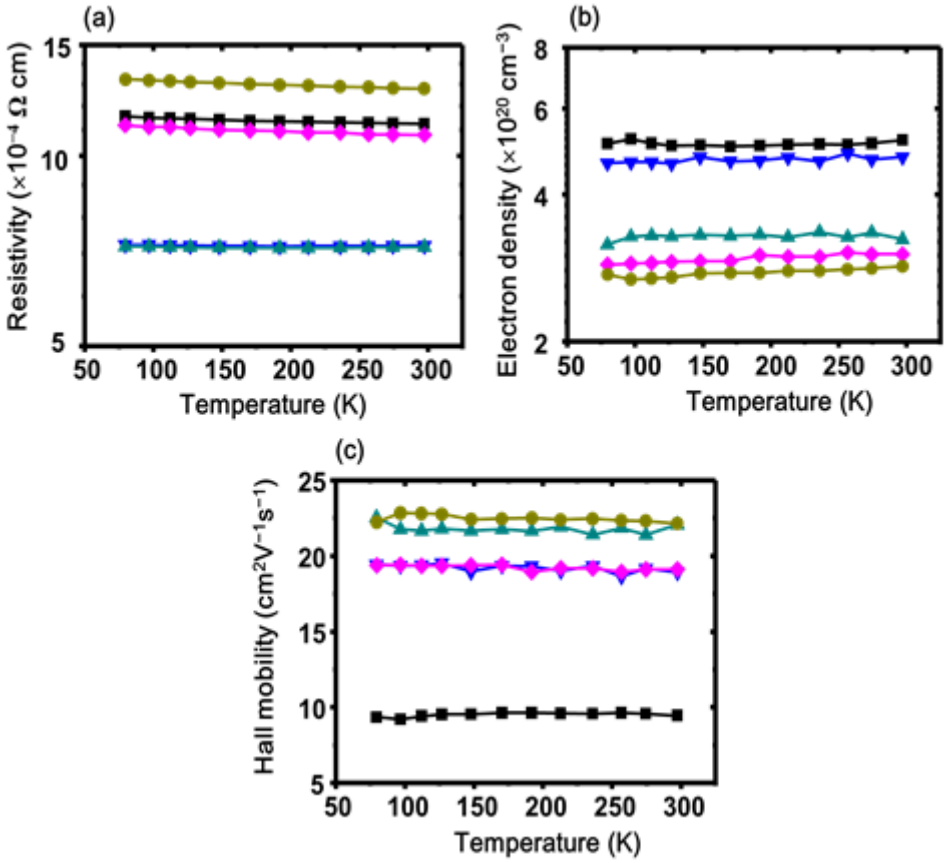

Figure 5.5. (a) Resistivity ρ–temperature T measurement, (b) Electron density n_e–temperature T measurement, (c) Hall mobility μ_H–temperature T measurement for $ZnSnN_2$ epi-films which were measured at temperature ranged from 77 to 300 K. Black square, inverted triangle, triangle, diamond, and circle marks present samples grown at partial nitrogen of 1.2, 1.4, 1.6, 1.8, 2.0 Pa, respectively.

5.3.4 Optical Properties of $ZnSnN_2$ Thin Films

The absorption coefficients α were estimated in order to determine the bandgap of the epitaxial $ZnSnN_2$ thin films. The absorption coefficients were calculated from the optical transmission spectra.

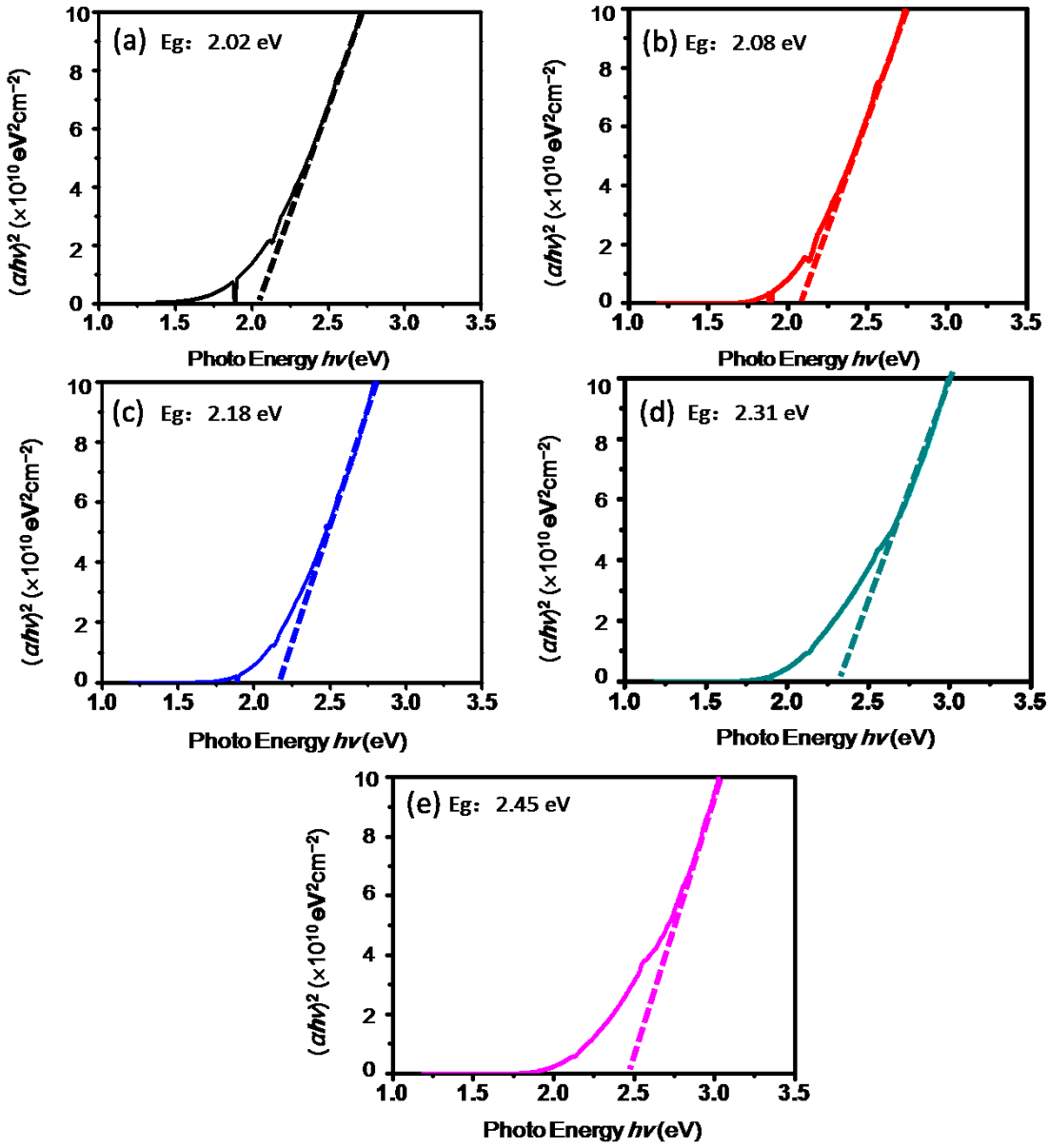

Figure 5.6. $h\nu$ versus $(\alpha h\nu)^2$ plots (Tauc-plot) for $ZnSnN_2$ epi. films with (a) $n_e = 2.8 \times 10^{20}$ cm^{-3}, (b) $n_e = 3.0 \times 10^{20}$ cm^{-3}, (c) $n_e = 3.3 \times 10^{20}$ cm^{-3}, (d) $n_e = 4.8 \times 10^{20}$ cm^{-3}, and $n_e = 5.1 \times 10^{20}$ cm^{-3}. The dashed lines are extrapolating the linear portion to $h\nu\alpha = 0$ to deduce bandgap energy for each $ZnSnN_2$ thin film.

Since $ZnSnN_2$ has been reported to be a semiconductor with a direct gap [4, 9, 13-14], we estimated E_g using the following fundamental equation: $(h\nu\alpha)^2 = A(h\nu - E_g)$, where $h\nu$ denotes photon energy and A is a constant. The absorption coefficients α of $ZnSnN_2$ films

were determined from transmittance measurements. The calculation of α was given using the following expression: $\alpha = (1/d)\ln[(1-R)/T]$, from whence α can be obtained if R and T are measured (d is the thickness of film sample). We determined E_g by extrapolating the linear portion to $h\nu\alpha = 0$ and obtained Figure 5.6. As seen in Figure 5.6, with the n_e increased from 2.8×10^{20} to 5.1×10^{20} cm^{-3}, the deduced bandgap values also increased from 2.0 to 2.5 eV. The estimated optical bandgaps increased with electron density increasing, suggesting a blue shift of bandgap. Such a blue shift can be interpreted as a result of Burstein-Moss effect. The Burstein-Moss effect results from the Pauli Exclusion Principle and is usually seen in degenerated semiconductors. Usually for an undoped semiconductor, the top of the valence band is full of occupied electrons; while the bottom of the conduction band is empty. When heavy n-type doping occurs, the electron density exceeds the conduction band edge density of state, then the exceeding electrons start to occupy the energy state at the bottom of conduction band and push Fermi level upper. With electron density increasing more, more and more exceeding electrons are inclined to occupy the energy state within conduction band. In such cases, when measured optical bandgap using optical transmittance and reflectance spectra, only we can get is the apparent optical bandgap, because an electron can only be excited from the top of the valence band (at k_F) to the conduction band just below the Fermi level. This case is often happened, for example as a case of InN, its now-accepted gap of approximately 0.69 eV is much smaller than that of its initially reported bandgap about 1.9−2.1 eV, which has largely been attributed to this effect. With regard to the factor of cation disorder degree, we will discuss it below in Figure 5.7.

Recent new interest in heterovalent $ZnSnN_2$ partly due to the fact that its unique properties are both similar to and complementary to the well-known III-N semiconductors. Structurally, from the binary III-N nitrides to the ternary II-IV-N nitrides (here, $ZnSnN_2$), it can be thought to derive by replacing the group III element by, alternatingly, Zn (group II) and Sn (group IV) elements. Hence, new questions and additional complexity will come

into being owing to the additional degree of freedom of having two different valence cations. Most notable is the question of the ordering of the cations.

This notable question can affect the band structure property which has been confirmed in lots of materials both from theoretical predictions [15-22] and experimental findings [23-26]. Such a phenomenon of tunable disorder is well known for semiconductor alloys [27]. In our case of $ZnSnN_2$ material, there was a recent theoretical prediction proposed by Feldberg *et al.* [11], who had found that for the ideal ordered structure (ordered orthorhombic $Pna2_1$ structure) having a bandgap energy of 2.09 eV at zero K, in contrast to the "fully" disordered structure ("fully" disordered monoclinic structure), its bandgap energy was calculated to be 1.12 eV. What it should be mentioned here is that, however, what constitutes "full disordered" was not identified, and statistics on the number of each type of tetrahedron in the structure was not provided.

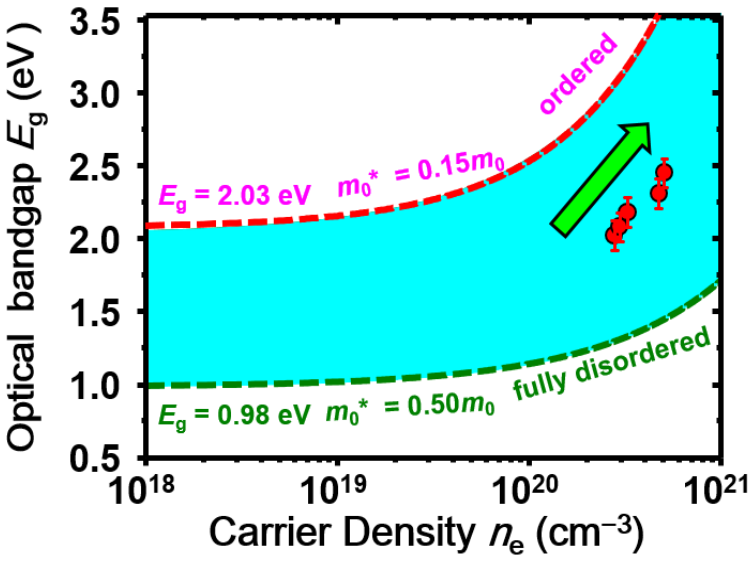

Figure 5.7. The relationship of the Tauc-plot-extracted optical bandgaps (red square marks) for $ZnSnN_2$ epi. films *vs.* electron density n_e.The curve area is formed by calculating two extreme cases: ordered structure and "fully" disordered structure, red dashed line and green dashed line, respectively, taking both a theoretical and experimental effective electron masses for ordered and "fully" disordered structures into consideration, 0.15m_0 and 0.50m_0, respectively.

In Veal's work [8], they theoretically derived the effective electron masses of both orthorhombic and disordered wurtzite-like structure of $0.147m_0$ and $0.12m_0$. On the other hand, in Fioretti's work [4], they experimentally extracted the effective electron mass of ordered $Pna2_1$ structure $ZnSnN_2$ from the relationship of absorption edge data and electron density, and yielded $0.5m_0$. However, the experimental value of effective electron mass for "fully" disordered structure has not been reported till now. According to the Burstein-Moss model, for a *n*-type semiconductor material, its bandgap shift (widening, ΔE_g) can be expressed in a relation to electron density n_e

$$\Delta E_g = \frac{\hbar^2}{2m^*}(3\pi^2 n_e)^{2/3} \tag{6.1}$$

Where, m^* is the effective electron mass, n_e is the electron density, $\hbar$ is the reduced Planck constant (= $h/2\pi$). Taken above-mentioned theoretical and experimental results (*i.e.*, Veal's work and Fioretti's work,respectively), we plotted the optical bandgap shifts ΔE_g, using Eq. 6.1, for each $ZnSnN_2$ films as a function of electron density n_e, which is shown in Figure 5.7. In this case, the optical bandgaps of epitaxial $ZnSnN_2$ films is the sum of "intrinsic" bandgap and the Burstein-Moss shifted bandgap ΔE_g, which is expressed like

$$E_g^{opt} = E_g + \Delta E_g^{BM} \tag{6.2}$$

Thus, the so-called "intrinsic" bandgap of $ZnSnN_2$ material can be obtained using the least-square fitting method from the variation of optical bandgaps as a function of the 2/3 power of electron density n_e, which is depicted in the following Figure 5.8. From which, the so-called "intrinsic" bandgap was determined to be around 1.67 eV. What should be mentioned here is that, one is in the lower $(n_e)^{2/13}$ range, *ca.* 0.3×10^{13} cm^{-3}, there existed a relatively low optical bandgap, this very point came from my following student's data which was obtained under different substrate temperature and the same target; the other due to material parameter is much more important for studying a new material, hence, in order to more correctly deduced the so-called "intrinsic" bandgap of $ZnSnN_2$ material, we added additional extracted values which were from the reproducibility experiments (under

the same conditions). The good fitting using the lease-square fitting method indicated that a good reproducibility and systematical data were extracted.

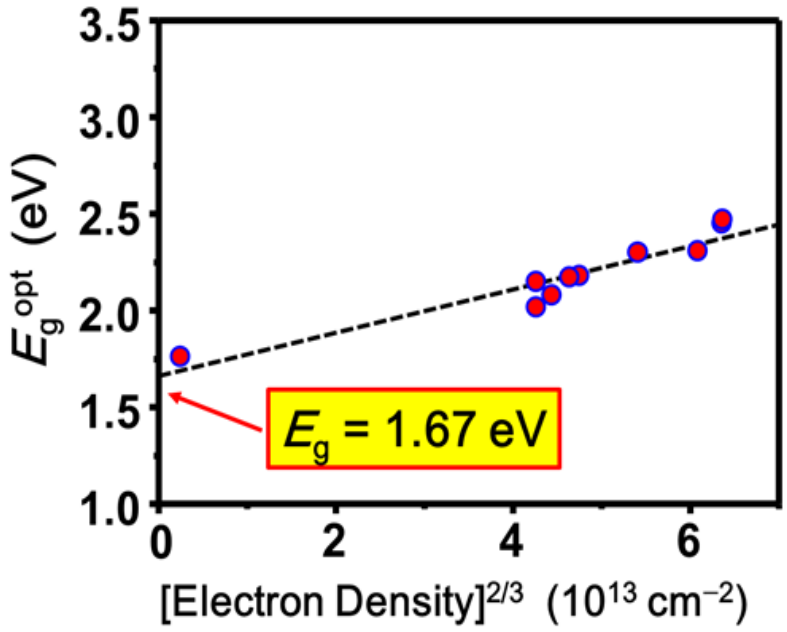

Figure 5.8. The variation of optical bandgaps as a function of the 2/3 power of electron density n_e for all of our sputtered grown epitaxial $ZnSnN_2$ thin films.

From Figures 5.7 and Figure 5.8, it can be clearly seen that the Tauc-plot-extracted optical bandgaps for $ZnSnN_2$ epi. films had a distinct increase tendency with n_e increasing, confirming the Burstein-Moss effect as a result of conduction band filling. The extracted bandgap values located in the middle of the formed curve area and the determined "intrinsic" bandgap of 1.67 eV, indicating two possible situations: one is that all the $ZnSnN_2$ films show partially ordered structure; the other is that our extracted bandgaps for $ZnSnN_2$ epi. films were underestimated. The former situation can be confirmed from our XRD processing (our theoretical calculation (Figure 5.9(a)); our experimental result, see Figure 5.9(b)): a distinguish difference between the ordered and disorder structure exists in the appearance of 011 and 110 peak or not. A wide range 110 rocking cure in Figure 5.9(b) shows no reflection peak, suggesting $ZnSnN_2$ structure is not ordered structure. Notably,

XRD characterization alone is not enough to identify evidently the variation of the cation disorder degree within the grown $ZnSnN_2$ thin films.

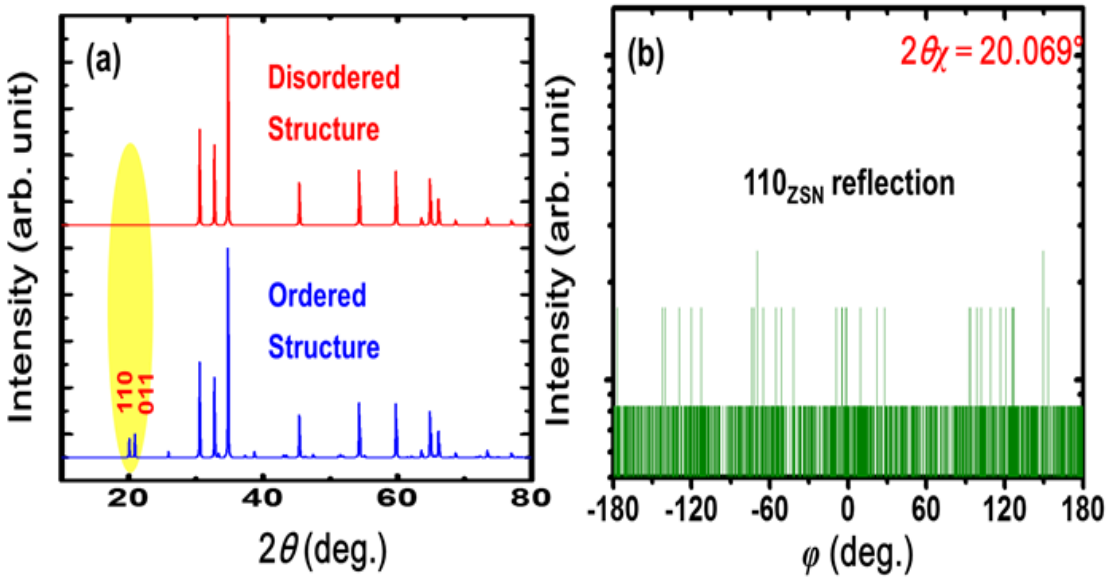

Figure 5.9. (a) The distinguish between disordered structure and ordered structure from the simulated XRD patterns. (b) A wide range 110 ($2\theta\chi$) rocking cure of a typical epitaxial $ZnSnN_2$ thin film.

5.3.5 Electron Effective Mass of $ZnSnN_2$ Thin Films

Similar with our another study object, binary Zn_3N_2 material, we also derived the effective electron mass of $ZnSnN_2$ material. Because all the processing method and calculation method was the same to that of Zn_3N_2 which have already been given in Part 4.4.1 in detail, in the following discussion we will present our calculated results. The optical property of electron effective mass of $ZnSnN_2$ thin film on YSZ(111) single crystal substrates was derived by a series of transmittance and reflectance measurements. What's different in this part is that we took advantage of double Tauc–Lorentz (TL) dispersion function combined with classical Drude dielectric function model to deduce the electron effective masses of $ZnSnN_2$ thin films. Many reported articles have proved that using thus TL-Drude model

can provide reasonable and excellent experimental data, such as the cases of Ga:ZnO and ITO thin films [28]. The TL-Drude model can be expressed by combing the TL term [29] and Drude term. The TL term and the Drude term are used to model the band-to-band energy absorption and the free-electron absorption, respectively. The imaginary part (ε_2) of dielectric function of the TL-Drude model is described by

$$\varepsilon_2(E)=\begin{cases}\dfrac{1}{E}\dfrac{A_{TL}E_0C_\gamma(E-E_g)^2}{(E^2-E_0^2)^2+C_\gamma{}^2E^2}+\dfrac{A_D\Gamma_D}{E^3+\Gamma_D^2E}, & \text{for } E>E_g \\ \dfrac{A_D\Gamma_D}{E^3+\Gamma_D^2E}, & \text{for } E\le E_g\end{cases} \tag{6.3}$$

$$\varepsilon_1(E)=\varepsilon_\infty+\frac{2}{\pi}P\int_{E_g}^{\infty}\frac{\xi\cdot\varepsilon_2(\xi)}{\xi^2-E^2}d\xi \tag{6.4}$$

where A_{TL}, C_γ, A_D, and Γ_D, present the oscillator strength (amplitude) of TL term, the broadening parameter of TL term, amplitude of Drude term, and the broadening parameter of Drude term, respectively. E_0 is the transition energy of the Lorentz component in the TL model, and E_g is the bandgap energy.

For our spectra fitting, note that the expression for $E > E_g$ in Eq. 6.3 is the product of the Tauc law combined with the imaginary part of the Lorentz oscillator. The real part (ε_1) of the dielectric function can be derived from the expression of the imaginary part (ε_2) using the Kramers−Kronig integration [30], which is shown as Eq. 6.4. We utilized SCOUT software for spectrum simulation and made use of a three-phase model to carry out fitting processing, which is YSZ(111) substrate/epi. $ZnSnN_2$ film/surface rough layer. The spectrum simulations by using double TL-Drude model were shown in Figure 5.10.

From these simulations of experimental spectra, we have derived the electron effective masses of $ZnSnN_2$ thin films to be $m_{opt}^* = (0.37 \pm 0.05)m_0$. These values are greater than the previously calculated value of $0.1m_0$ [9, 31] or $0.147m_0$ [8] for ordered, $Pna2_1$

orthorhombic $ZnSnN_2$. Even though this discrepancy exists, yet the previous theoretical calculations [11] predicted that $ZnSnN_2$ with a wurtzite crystal structure may have a larger

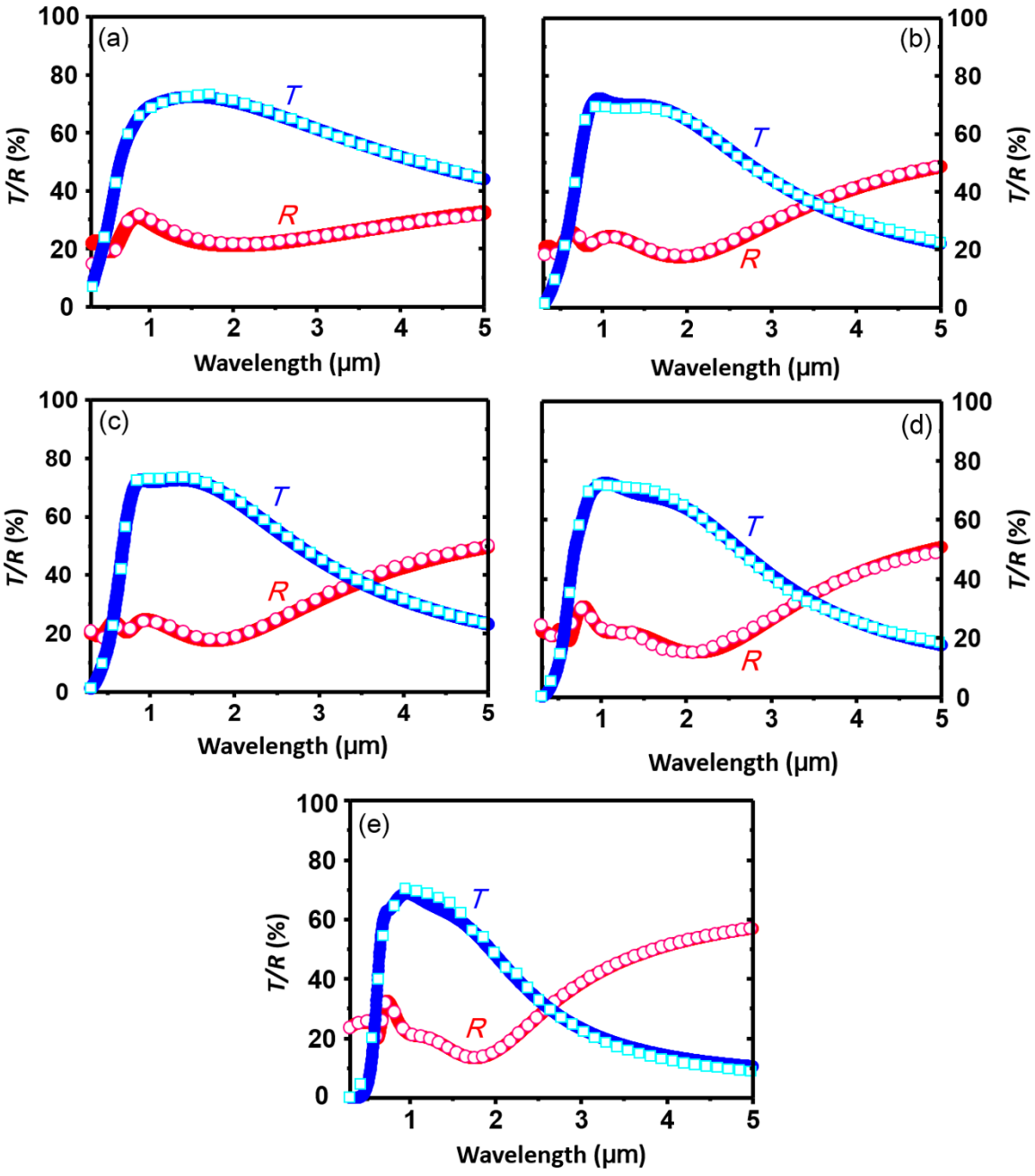

Figure 5.10. (a) Optical reflectance and transmittance for a typical epitaxial $ZnSnN_2$ film with $n_e = 4.0 \times 10^{20}$ cm^{-3}. The results of least-squares fitting using the Drude dielectric function are shown as solid lines. (b) Using the Eq. 4.5 to extract the effective electron mass (density of states effective mass m_d^*).

electron effective mass. However, the electron effective mass we have already extracted from this double TL-Drude model is of the appropriate order of magnitude and is < 1m_e, which is qualitatively consistent with previous calculations [8, 9, 31]. The good fitting make us believe that our derived electron effective mass has a relatively high accuracy than those already reported values, and probably those values are underestimated due to the approximate nature of their analysis.

5.4 Trial on Decreasing Electron Density of $ZnSnN_2$ Films

5.4.1 Issues and Trials

In the above-discussed work of Figure 5.4(a), all the films grown via a target $Zn_{0.5}Sn_{0.5}$ had n_e values larger than 10^{20} cm^{-3}, in good agreement with Refs. [8, 9, 12], which is a main challenge affecting $ZnSnN_2$ usage for a possible absorber material for PVs (usually free-carrier concentration is on the order of $\leq 10^{17}$ cm^{-3}). This challenge triggered us to find a way to lower this high electron density, such as a different target material, or an effective electron-killer to compensate the heavily-doping oxygen effect arose from oxygen contaminations.

In a combinatorial work [4] did by Fioretti's group, they observed the grown $ZnSnN_2$ films with 0.60 Zn/(Zn+Sn) having lower even lowest electron density, as shown in Figure. 5.11. This experimental finding had opened our mind to change our target material from $Zn_{0.5}Sn_{0.5}$ to $Zn_{0.6}Sn_{0.4}$. On the other hand, for the case of CIGS, efficient *n*-type doping presents a difficulty due to the formation energy of electron-killer Cu vacancies pinning the Fermi energy below the conduction band minimum, compensating further *n*-type doping. From the positions of Cu, Zn and Sn in periodic table of elements, Cu(I) is inferred to serve as a possible electron-killer in $ZnSnN_2$ material.

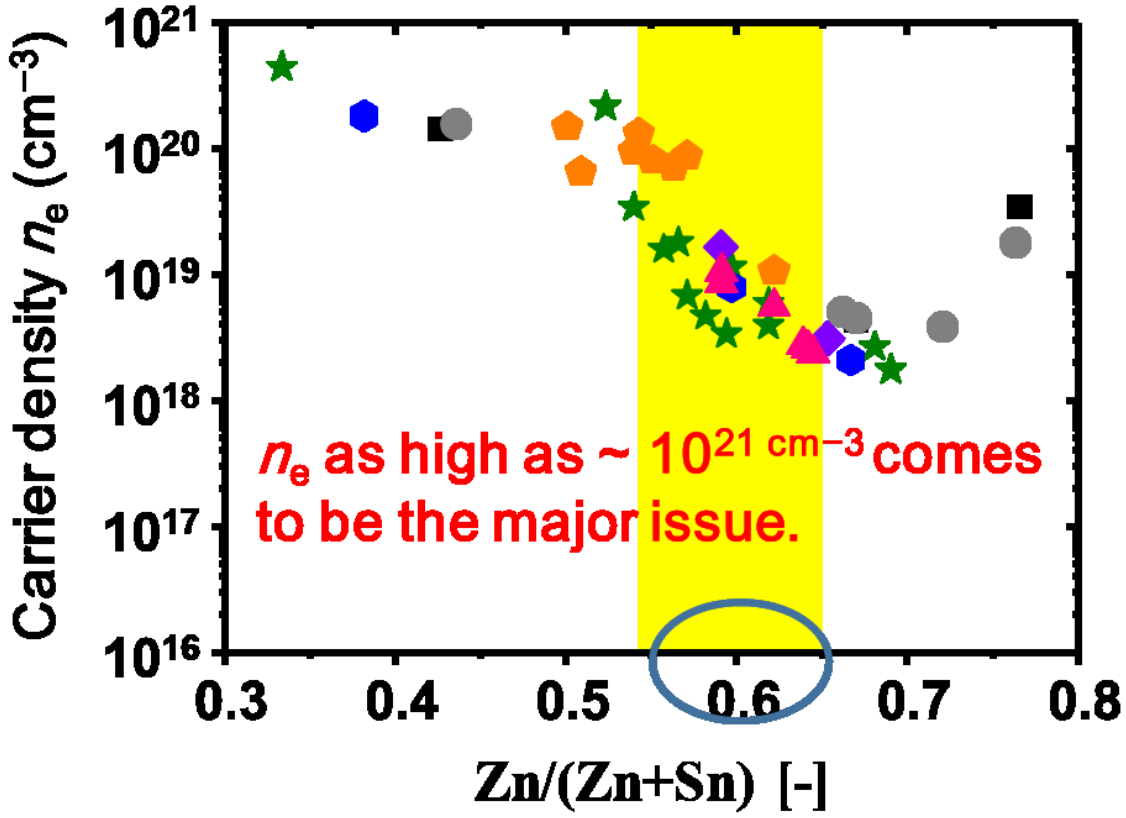

Figure 5.11. Electron density in $ZnSnN_2$ films as a function of zinc concentration, Zn/(Zn+Sn) (Adapted from [4]).

5.4.2 Growth of $ZnSnN_2$ Thin Films

The reactive RF magnetron sputtering technique was applied to grow $ZnSnN_2$ thin films on YSZ(111) single-crystal substrates at substrate temperatures of 300 °C. We used a metal $Zn_{0.6}Sn_{0.4}$ target (a diameter of 10 cm and purity of 99.9%) and N_2 concentrations were fixed at 80% during the film growth. Copper(Cu)-doing experiments were done by placing 4N purity Cu chips (0, 2, 3, 4, 5 pieces for this part of work) on the magnetron racetrack of the target, as is shown schematically in Figure 5.12). An RF power of 70 W was applied to the Zn target. A base pressure lower than 2×10^{-4} Pa was established in the growth chamber before the film growth. Sputtering was conducted in a gas mixture consisting of

Ar (99.999% pure) and N_2 (99.9995% pure) at a total pressure of 2 Pa. Prior to the growth, the target surface was sputter-etched with pure Ar for 30 min and was subsequently pre-sputtered for 10 min under the same condition with the film growth. The growth time was adjusted to obtain a thin film with a thickness of 100–300 nm. After the film growth, the films were immediately stored in another vacuum chamber (the pressure was about 1 Pa) for subsequent measurements.

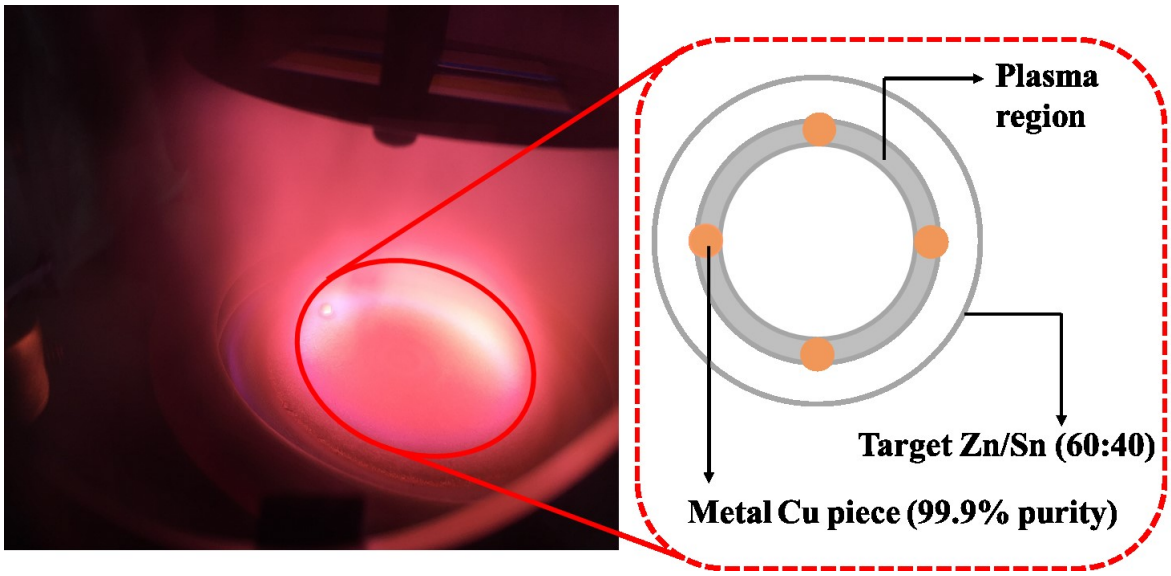

Figure 5.12. Schematic depiction for Cu(I)-doping into $ZnSnN_2$ films grown by using reactive radio-frequency magnetron sputtering technique with a $Zn_{0.6}Sn_{0.4}$ target (a diameter of 10 cm and purity of 99.9%). The Cu thin chip pieces have a diameter of 1 cm and purity of 99.99%.

5.4.3 Chemical State and Composition

XPS analyses were performed to determine the chemical states of Cu and O. Herein, we present spectra for the films deposited at piece number of Cu = 4 in Figure 5.13. As can be seen in Figure 5.13 (a), weak satellite peaks appear in the region of *BE* ranging from 940 to 950 eV, indicating Cu shows chemical valence state of +1 in $ZnSnN_2$ films due to the fact that the distinct differential between Cu(I) and Cu(II) is whether strong satellite peaks between *BE* = 940 to 950 eV appear or not. In order to confirm this information, we also

measured the Cu LMM auger peak which is shown in Figure 5.13(d) to compare to the Cu auger peaks among Cu_2O, CuO and metal Cu, which is shown in Figure 5.13(c). A similar peak appeared kinetic energy around 916.9 eV, which confirmed that Cu shows chemical valence state of +1 in $ZnSnN_2$ films. The positive result from Figure 5.13(a) told us the successful Cu(I)-doping growth of $ZnSnN_2$ thin films was achieved by this easy way.

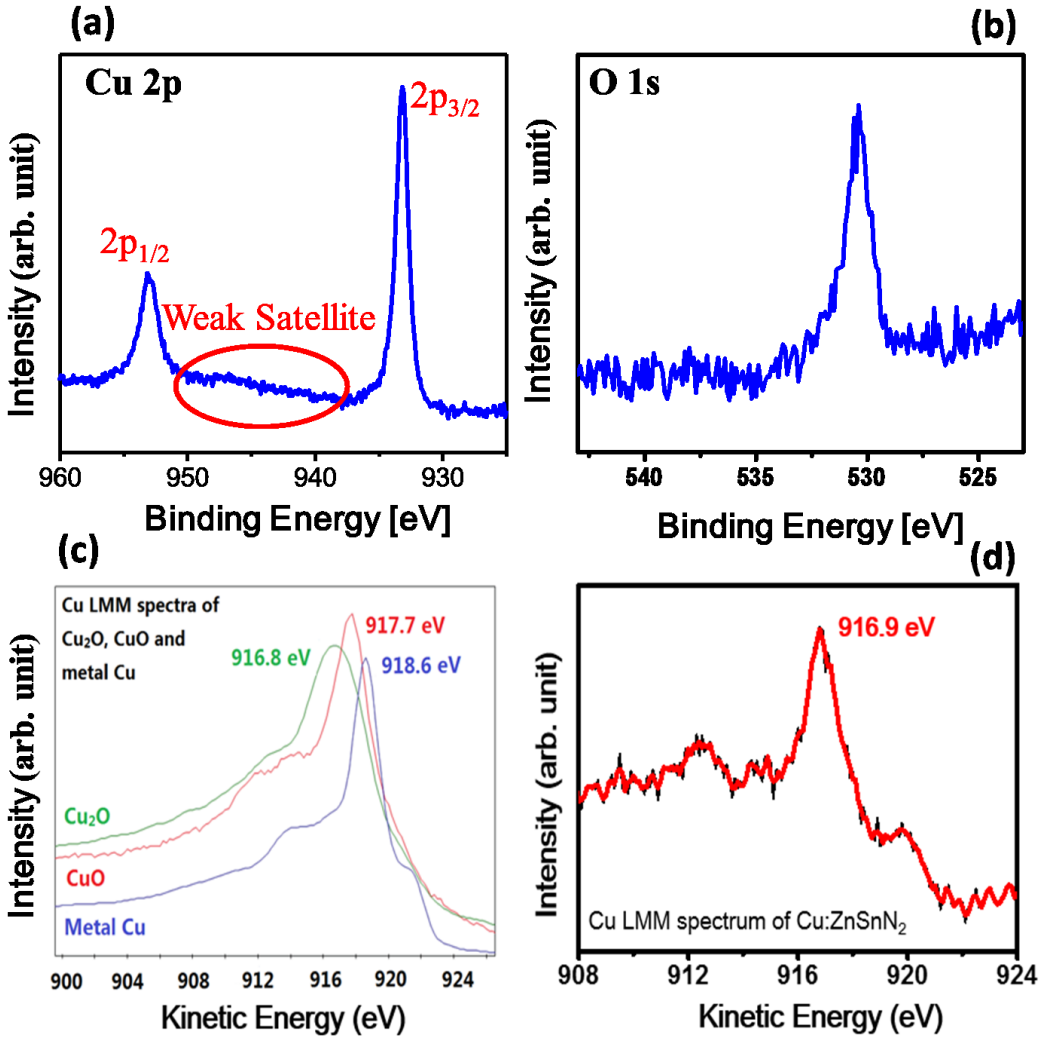

Figure 5.13. (a) X-ray excited Cu 2p and (b) O 1s XPS core spectra for a typical $ZnSnN_2$ film deposited under the condition of Cu piece number of 4 . (c) Cu LMM Auger XPS spectra of Cu_2O, CuO and metal Cu. (d) Cu LMM Auger XPS spectra of for the same typical $ZnSnN_2$ film (Cu piece number equals 4).

The appearance of O 1s peak (Figure 5.13(b)) in the measurement results also stated that

oxygen impurities existed within our $ZnSnN_2$ thin film host, similar to the case of Zn_3N_2, which confirmed our expectation that the heavily-doping effect originated from oxygen contaminations as mentioned above.

We took advantage of the RSF method to establish both the oxygen concentrations, *i.e.*, x values in Cu:$ZnSnN_{2-x}O_x$ films and Cu concentrations in Cu:$ZnSnN_{2-x}O_x$ films. The processing method of the former is given in Part 5.3.3, while the Cu concentrations, represented by Cu ratios Cu/(Cu+Zn+Sn), were given by average of X_{Cu}/X_{Zn} and X_{Cu}/X_{Sn}. The X_{Cu}/X_{Zn} given by (I_{Cu}/S_{Cu}) times (S_{Zn}/I_{Zn}) and the X_{Cu}/X_{Sn} given by (I_{Cu}/S_{Cu}) times (S_{Sn}/I_{Sn}), where I_{Cu}, I_{Zn}, I_{Sn}, S_{Cu}, S_{Zn}, and S_{Sn} represent the Cu 2p 3/2 integral intensity, Zn 2p 3/2 and Sn 3d 5/2 peaks integral intensity, respectively; RSF of Cu (4.798), Zn (3.354) and Sn (4.095).

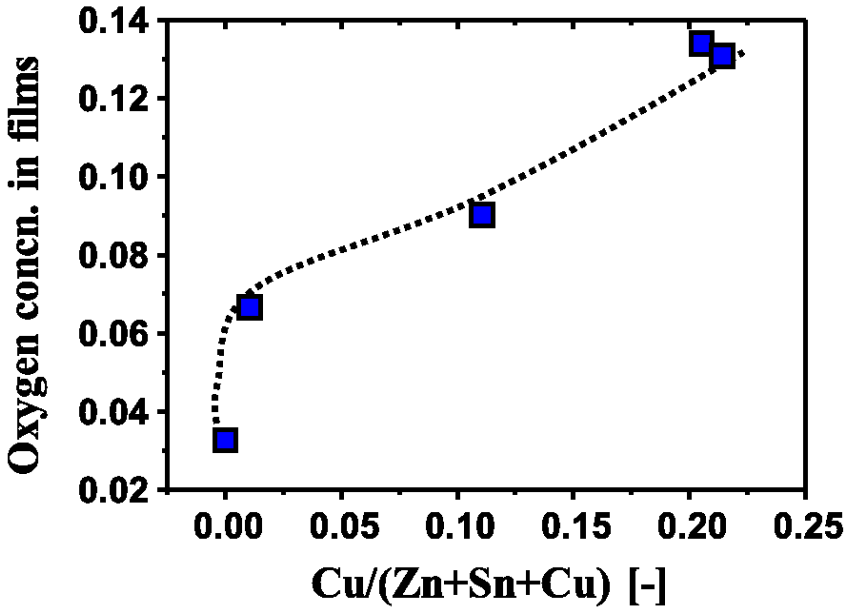

Figure 5.14. Oxygen concentration, x values in Cu:$ZnSnN_{2-x}O_x$ films as a function of copper concentration in Cu:$ZnSnN_{2-x}O_x$ films.

The oxygen concentration as a function of Cu concentration is plotted is Figure 5.14 as above. From this figure, a clear trend of oxygen concentration increased with increasing in Cu concentration maybe due to the so-called "gettering" effect [32], which is commonly

happened in a vacuum chamber like sputtering technique. Such an interesting finding indicated that copper used in $ZnSnN_2$ thin film deposition process could be a oxygen-getter resulting in this increasing tendency.

5.4.4 Comparison of Carrier Densities of n_e^{oxygen} and n_e^{Hall}

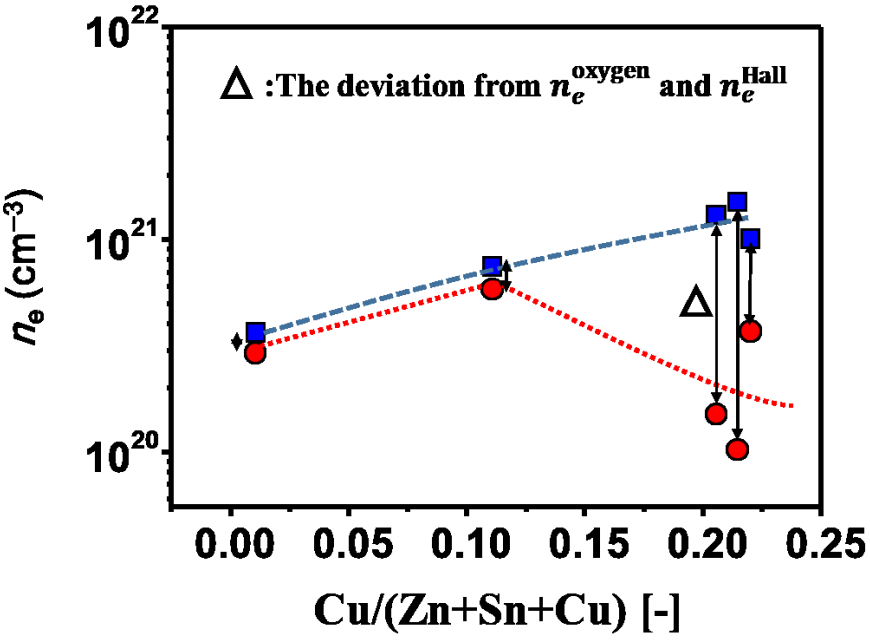

Figure 5.15. Comparison of the electron density obtained from two different kinds of methods: one is the calculation data from the XPS results and the other is from the Hall measurements. n_e^{oxygen} (square marks) presents the electron density from the calculation data from the XPS results, while n_e^{Hall} (circle marks) originates from Hall measurements. The dashed lines are a guide for the eyes.

As we illustrated earlier, oxygen impurity and copper dopant affect the electrical properties in two different ways, which oxygen impurity can be considered as an electron donor while the copper impurity can be served as an electron-killer. The practical relationship between these two "contradictory" parts is more sophisticated given that the abovementioned possible "gettering" effect. We, therefore, investigated the relationship between them from the effect on electron density perspective, as seen in Figure 5.15. The n_e^{oxygen} presents the

electron density from the calculation data from the XPS results, while n_e^{Hall} originates from Hall measurements. It should be pointed out that we assumed that oxygen substitutes in nitrogen site can be considered as an electron donor, which is similar with the case of Zn_3N_2 and another important assumption that the substitutional oxygen in nitrogen site has a *n*-type doping efficient of 30% given not all substitutional oxygen releases an electron. With calculations of volume of one $ZnSnN_2$ unit cell, we can calculate the substitutional oxygen concentrations and then the free electron density originates from the electron release from the Köger–Vink notation as $O_N^x \rightarrow O_N^{\cdot} + e'$. From the Figure 5.15, it can be

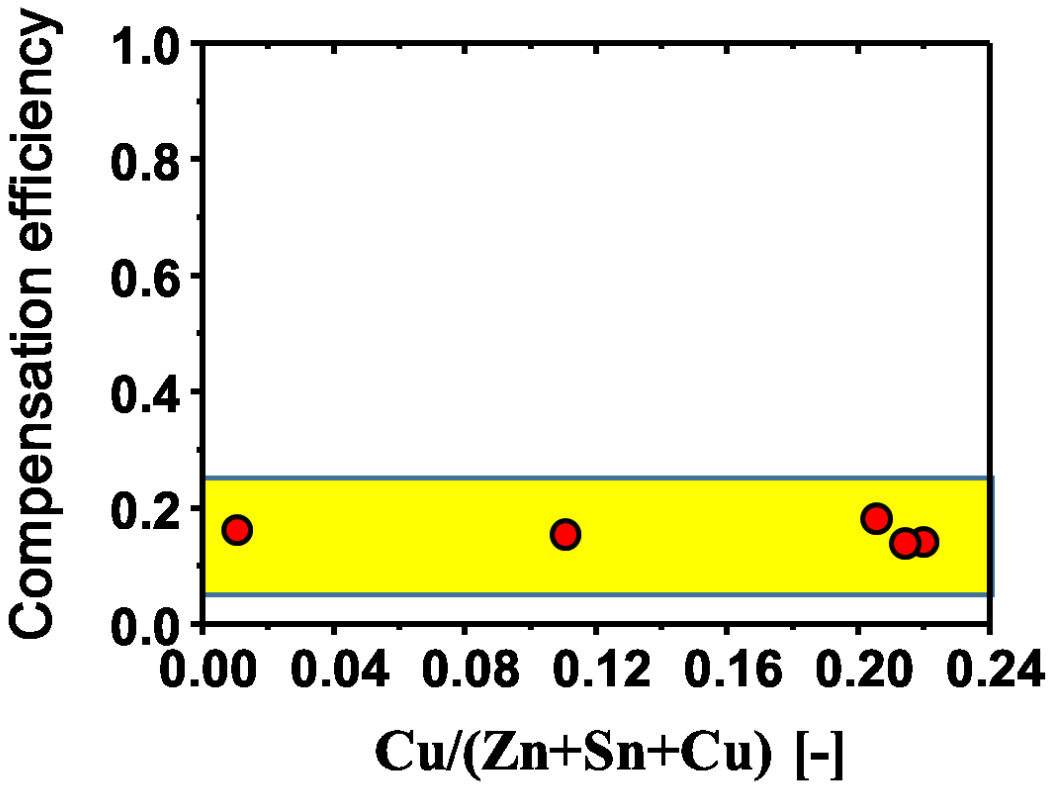

Figure 5.16. Compensation efficiency of electron-killer copper confronting the electron-release oxygen.

seen that the discrepancy between these two kinds of carrier density enlarged with the discrepancy with copper concentration increasing, namely the carrier density became lower with Cu concentration increased. The dopant copper as a electron-killer confronts the

electron-release dopant oxygen, which is shown in Figure 5.16. We calculated the compensation efficiency combined n_e^{oxygen} with n_e^{Hall} and derived it to be a near constant 18%, indirectly confirming the assumptions we made above was reasonable. Such a not high compensation efficiency indicated that copper could be considered as electron-killer to some extent while another more effective electron-killer needs to be exploited in future to further decrease electron density in $ZnSnN_2$ material used as a PV absorber.

5.5 Summary

In this Chapter, we investigated another zinc-based nitride semiconductor, ternary $ZnSnN_2$, which is analogue to GaN. Reactive radio-frequency magnetron sputtering technique is applied to grow $ZnSnN_2$ thin films on single-crystal YSZ(111) substrates and conducted preliminary characteristics for $ZnSnN_2$. The structural analyses inferred $ZnSnN_2$ probably has a random-wurtzite type disordered structure. Being similar with the case of Zn_3N_2, oxygen defects in $ZnSnN_2$ films were responsible for unintentional degenerate *n*-type doping. In copper Cu(I)-doped $ZnSnN_2$ films, Cu served as an effective electron killer compensating further *n*-type doping to a certain extent. The estimated "scattered" bandgaps in the range 2.0–2.6 eV were due in part to high degenerate electron density and disorder degree in the cation sublattice. Electron effective mass of $ZnSnN_2$ material is derived to be around $(0.37\pm0.05)m_0$ from double Drude model fitting. The discoveries made suggest that high-quality (nearly intrinsic, optimal-cation disorder) $ZnSnN_2$, comprised of earth-abundant elements, can be an alternative to InGaAlN materials system and has the potential to be applied to photovoltaics and solid-state lighting both from economic and environmental perspectives.

5.6 Bibliography

[1] T. M. Razykov, C. S. Ferekides, D. Morel, E. Stefanakos, H. S. Ullal, and H. M. Upadhyaya, Solar photovoltaic electricity: Current status and future prospects, *Sol. Energy* **85**, p. 1580 (2011).

[2] A. Goetzberger, C. Hebling, and H. W. Schock, Photovoltaic materials, history, status and outlook, *Mater. Sci. Eng. R* **40**, p. 1 (2003).

[3] B. Parida, S. Iniyan, and R. Goic, A review of solar photovoltaic technologies, *Renewable Sustainable Energy Rev.* **15**, p. 1625 (2011).

[4] A. N. Fioretti, A. Zakutayev, H. Moutinho, C. Melamed, J. D. Perkins, A. G. Norman, M. Al-Jassim, E. S. Toberer, and A. C. Tamboli, Combinatorial insights into doping control and transport properties of zinc tin nitride, *J. Mater. Chem. C* **3**, p. 11017 (2015).

[5] N. Asim, K. Sopian, S. Ahmadi, K. Saeedfar, M. A. Alghoul, O. Saadatian, and S. H. Zaidi, A review on the role of materials science in solar cells, *Renewable Sustainable Energy Rev.* **16**, p. 5834 (2012).

[6] M. Edoff, Thin Film Solar Cells: Research in an Industrial Perspective, *Ambio* **41**, p. 112 (2012).

[7] B. W. Jaskula, *Mineral Commodity Summaries*, U.S. Geological Survey, Reston, Virginia, 2013.

[8] T. D. Veal, N. Feldberg, N. F. Quackenbush, W. M. Linhart, D. O. Scanlon, L. F. J. Piper, and S. M. Durbin, Band gap dependence on cation disorder in $ZnSnN_2$ solar absorber, *Anv. Energy Mater.* **5**, p. 1501462 (2015).

[9] L. Lahourcade, N. C. Coronel, K. T. Delaney, S. K. Shukla, N. A. Spaldin, and H. A. Atwater, Structural and optoelectronic characterization of RF sputtered $ZnSnN_2$, *Adv. Mater.* **25**, p. 2562 (2013).

[10] F. Kawamura, N. Yamada, M . Imai, and T. Taniguchi, Synthesis of $ZnSnN_2$ crystals via a high-pressure metathesis reaction, *Cryst. Res. Technol.* **51**, p. 220 (2016).

[11] N. Feldberg, J. D. Aldous, W. M. Linhart, L. J. Phillips, K. Durose, P. A. Stampe, R. J. Kennedy, D. O. Scanlon, G. Vardar, R. L. Field III, T. Y. Jen, R. S. Goldman, T. D. Veal,

and S. M. Durbin, Growth, disorder, and physical properties of $ZnSnN_2$, *Appl. Phys. Lett.* **103**, p. 042109 (2013).

[12] A. N. Fioretti, E. S. Toberer, A. Zakutayev, and A. C. Tamboli, Effects of low temperature annealing on the transport properties of zinc tin nitride, *Photovoltaic Specialist Conference (PVSC), IEEE 42nd*, p. 1 (2015).

[13] P. C. Quayle, K. L. He, J. Shan, and K. Kash, Synthesis, lattice structure, and band gap of $ZnSnN_2$, *MRS Commun.* **3**, p. 135 (2013).

[14] R. F. Qin, H. T. Cao, L. Y. Liang, Y. F. Xie, F. Zhuge, H. L. Zhang, J. H. Gao, K. Javaid, C. C. Liu, and W. Z. Sun, Semiconducting $ZnSnN_2$ thin films for Si/$ZnSnN_2$ *p-n* junctions, *Appl. Phys. Lett.* **108**, p. 142104 (2016).

[15] D. Skachkov, P. C. Quayle, K. Kash, and W. R. L. Lambrecht, Disorder effects on the band structure of $ZnGeN_2$: Role of exchange defects, *Phys. Rev. B* **94**, p. 205201 (2016).

[16] D. O. Scanlon and A. Walsh, Bandgap engineering of $ZnSnP_2$ for high-efficiency solar cells, *Appl. Phys. Lett.* **100**, p. 251911 (2012).

[17] C. Rincón, Order-disorder transition in ternary chalcopyrite compounds and pseudobinary alloys, *Phys. Rev. B* **45**, p. 12716 (1992).

[18] C. Rincón, On the order-disorder phase transition in ternary compounds, *Solid State Commun.* **64**, p. 663 (1987).

[19] A. V. Krukau, O. A. Vydrov, A. F. Izmaylov, and G. E. Scuseria, Influence of the exchange screening parameter on the performance of screened hybrid functionals. *J. Chem. Phys.* **125**, p. 224106 (2006).

[20] A. Roy, S. Mukherjee, S. Sarkar, S. Auluck, R. Prasad, R. Gupta, and A. Garg, Effects of site disorder, off-stoichiometry and epitaxial strain on the optical properties of magnetoelectric gallium ferrite, *J. Phys.: Condens. Matter* **24**, p. 435501 (2012).

[21] S. Chen, X. G. Gong, A. Walsh, and S. Wei, Electronic structure and stability of quaternary chalcogenide semiconductors derived from cation cross-substitution of II-VI and I-III-VI_2 compounds, *Phys. Rev. B* **79**, p. 165211 (2009)

[22] K. E. Newman and J. D. Dow, Zinc-blende-diamond order-disorder transition in metastable crystalline $(GaAs)_{1-x}Ge_{2x}$ alloys, *Phys. Rev. B* **27**, p. 7495 (1983).

[23] J. J. S. Scragg, L. Choubrac, A. Lafond, T. Ericson, and C. PlatzerBjorkman, A low-temperature order−disorder transition in Cu_2ZnSnS_4 thin films. *Appl. Phys. Lett.* **104**, p. 041911 (2014).

[24] S. Shang, Y. Wang, G. Lindwall, N. R. Kelly, T. J. Anderson, and Z. Liu, Cation disorder regulation by microstate configurational entropy in photovoltaic absorber materials $Cu_2ZnSn(S,Se)_4$, *J. Phys. Chem. C* **118**, p. 24884 (2014).

[25] A. Amat, E. Mosconi, E. Ronca, C. Quarti, P. Umari, M. K. Nazeeruddin, M. Grätzel, and F. D. Angelis, Cation-induced band-gap tuning in organohalide perovskites: Interplay of spin−orbit coupling and octahedra tilting, *Nano Lett.* **14**, p. 3608 (2014).

[26] M. J. Seong, H. Alawadhi, I. Miotkowski, A. K. Ramdas, S. Miotkowska, The anomalous variation of band gap with alloy composition: cation vs anion substitution in ZnTe, *Solid State Commun.* **112**, p. 329 (1999).

[27] A. Mascarenhas, *Spontaneous Ordering in Semiconductor Alloys*, Plenum Pub Corp, 2002.

[28] H. Fujiwara and M. Kondo, Effects of carrier concentration on the dielectric function of ZnO:Ga and In_2O_3:Sn studied by spectroscopic ellipsometry: Analysis of free-carrier and band-edge absorption, *Phy. Rev. B*, **71**, p. 075109 (2005).

[29] J. G. E. Jellison and F. A. Modine, Parameterization of the optical functions of amorphous materials in the interband region, *Appl. Phy. Lett.*, **69**, p. 371 (1996).

[30] J. S. Toll, Causality and the dispersion relation: logical foundations, *Phys. Rev.* **104**, p. 1760 (1956).

[31] S. Y. Chen, P. Narang, H. A. Atwater, and L. W. Wang, Phase stability and defect physics of a ternary $ZnSnN_2$ semiconductor: First principles insights, *Adv. Mater.* **26**, p. 311 (2014).

[32] *Gettering*, Retrieved from http://dunham.ee.washington.edu/ee539/notes/getter.pdf

Chapter 6

Conclusions and Perspectives

However difficult life may seem, there is always something you can do and succeed at.

—Stephen Hawking

In this final Chapter, what we have already done and ever expected to achieve for our work will be concluded and contextualized. We concentrated our attention on zinc nitride (Zn_3N_2) and zinc tin nitride ($ZnSnN_2$) thin film materials, both are relatively "young" materials with the tangible industry benefits of being solely composed of Earth-abundant, environmentally-benign, economy-efficiency elements. It is because their "less-discovery" of property that makes them remain unclear from both the perspectives of materials science and materials applications, which also triggered us to deploy our researches. The residual knotty problems, possible directions of these problems, together with future development in our work and related work will be given in a brief organization in the following "Perspectives for Future Work" Part.

Our group work, we believe and hope, is more than a fundamental research that fills in some gaps for these two study objects, also can have positive and enlightening significancy for the newcomers follow-up in materials science.

6.1 Conclusions of Our Work

The deployment of our research work was intrigued by a guiding thought of "expanding Transparent Conducting Oxides (TCOs) to Transparent Conducting Nitrides (TCNs)". The overall goals of this work lie in three standpoints: i) illustration of the influence of the observed oxygen impurities within Zn_3N_2 thin film host on material properties; ii) clarification of the origin of high electron mobilities in Zn_3N_2 material; iii) determination of effective electron mass of $ZnSnN_2$ material and trial to lower the relatively-high electron density. High electron density in polycrystalline Zn_3N_2 films makes it attractive in solar cells, high mobility thin film transistors, and other optoelectronic devices; while $ZnSnN_2$ material with a theoretical bandgap value of 1.4 eV have a potential appliance in photovoltaic systems, moreover its related alloy $ZnSn_xGe_{1-x}N_2$ system (not our focus) can be considered as promising candidate alternatives to $In_xGa_{1-x}N$ alloys used for photovoltaic systems and solid-state lighting. For the illustrations above, deployment of our research work on Zn_3N_2 and $ZnSnN_2$ thin films can pave a path to reach our goals.

The dissertation presented here provided growth details, characterization techniques and related experimental results, analyses of properties, potential applications of study objects, *i.e.*, Zn_3N_2 and $ZnSnN_2$ thin films synthesized by reactive radio-frequency magnetron sputtering technique with high purity of Argon, nitrogen, with/without intentional oxygen gases as working gas and metal targets (high purity of Zn and Zn:Sn, respectively) as sputtering materials.

6.1.1 Illustration of the Influence of Oxygen Impurities

Because oxygen can be easily introduced into Zn_3N_2 film host no matter what deposition methods used. Neither the detail qualitative nor quantitative analyses of effect of unintentional oxygen impurity on properties of Zn_3N_2 film has been reported so far, we intentionally introduced oxygen into the film-growth chamber and investigated the

properties of oxygen-doped Zn_3N_2 as a potential zinc-based nitride transparent semiconductor. Phase-pure films were grown but XPS results indicated that a small amount of oxygen exists within all $Zn_3N_{2-x}O_x$ films. The electron transport properties of zinc nitride thin films were demonstrated to be controlled by varying oxygen concentration, *i.e.*, x in $Zn_3N_{2-x}O_x$. Heavily doped $Zn_3N_{2-x}O_x$ films can be considered as *n*-type degenerate semiconductors. The free electron density (n_e) in $Zn_3N_{2-x}O_x$ films increased was found increased from the magnitude order of 10^{19} to 10^{20} cm^{-3} as x increased, indicating that substitutional oxygen on nitrogen site behaves as an electron donor, which is consistent with the theoretical predictions. As a result, a highly conductive $Zn_3N_{2-x}O_x$ film with a resistivity of 6.2×10^{-4} Ω cm was obtained in a $Zn_3N_{1.81}O_{0.19}$ film. It is notable that $Zn_3N_{2-x}O_x$ films exhibited electron mobility (μ) above 70 cm^2 V^{-1} s^{-1} even in polycrystalline form. The μ values were approximately 100-fold those in degenerately doped GaN polycrystalline films and two-fold those in polycrystalline TCOs. Therefore, $Zn_3N_{2-x}O_x$ can be regarded as a high-mobility nitride-based semiconductor. Bandgap widening due to the Burstein–Moss effect was observed, supporting the notion that $Zn_3N_{2-x}O_x$ was degenerately doped. The optical gap (E_g^{opt}) was estimated to range from 2.3 to 2.6 eV, which was smaller than the previously reported value of 3.2 eV. We postulate that the small E_g^{opt} originates from the optical absorption by electron transition between the interstitial N 2p in-gap state and conduction/valence band. Further research is required for achieving truly transparent $Zn_3N_{2-x}O_x$ films with low resistivity reduction of the N_I density.

6.1.2 Clarification of the Origin of High Electron Mobilities in Zn_3N_2

Zinc nitride polycrystalline films and epitaxial films were deposited on non-alkali glass and YSZ(100) single crystal substrates, respectively, by reactive rf-magnetron sputtering technique. Small amounts of oxygen were detected along the thickness of Zn_3N_2 films both in polycrystalline and in epitaxial form. The electrical properties and optical bandgap can be tuned by varying the oxygen concentration, namely x in $Zn_3N_{2-x}O_x$. Electron density tends to increase as the value of x increases, indicating that substitutional O in the N site

can be considered to be electron donor. From the analyses of electron mobility, we understood that ionized impurity (probably $O_N^{\bullet}$) scattering governed the electron transport in epitaxial films, while both ionized impurity scattering and grain boundary scattering have main contributions to the electron transport in polycrystalline films. Moreover, neutral impurity scattering has negligible impact on the electron transport in Zn_3N_2. Despite the effect of grain boundary scattering, the electron mobilities attained were mostly above 65 $cm^2V^{-1}s^{-1}$ in both polycrystalline and epitaxial Zn_3N_2 films; this similarity between the mobilities makes Zn_3N_2 a potential choice for large-area cost-effective polycrystalline semiconductor devices. The effective masses at the bottom of the conduction band were derived to be $(0.08 \pm 0.03)m_0$, using the good agreement of the measured n_e–$m^*(n_e)$ dependence with the Pisarkiewicz model simulation. Such small effective mass was responsible for achievable high mobilities in zinc nitride. As for the optical properties, bandgaps were determined to be in the range of 2.2 to 2.7 eV, which were smaller than the previously reported value 3.2 eV. If we effectively reduce the concentration of interstitial in-gap state defects, Zn_3N_2 films with good transparency could be attained for electronic and optoelectronic applications such as LED devices and solar cells.

6.1.3 System Work of $ZnSnN_2$ Material

$ZnSnN_2$ thin films were grown on single-crystalline YSZ(111) substrates under various growth conditions. By adjusting the growth condition, we successfully grew polycrystalline and epitaxial films of $ZnSnN_2$ on YSZ(111). From analyses of its structure properties, we demonstrated that $ZnSnN_2$ material probably has a random-wurtzite type disordered structure. Similar to the case of binary Zn_3N_2 material, all the films were confirmed to be unintentionally doped with oxygen. As a result, the films had degenerate conduction electron gas with n_e in a range of 10^{19}~10^{21} cm^{-3}. The Hall mobility varied from < 1 to 30 $cm^2\ V^{-1}\ s^{-1}$. We believe that such relatively low Hall mobility maybe due in

part to the small grain size of grown $ZnSnN_2$ thin films. While high electron density mainly originated from heavy donor doping which attributed to the unintentional oxygen doping, somehow restricts its appliance for photovoltaic systems. In our work, we chose and examined the Cu(I)-doping to compensate the heavily oxygen-doping effect and found that the electron densities were still in level of 10^{20} cm^{-3}, the decreasing degree was not that obvious. Hence the further decreasing in electron density is needed and better option of dopant is necessary. On the other hand, to our best knowledge, we are the first to derive the effective electron mass m^* to be $(0.37 \pm 0.05)m_0$ by using double Drude-Lorentz model. The small effective electron mass is comparable with that of ZnO. The bandgap energy of $ZnSnN_2$ material remains debatable, due in large measure to both impurity doping and cation disorder degree. In our work, we derived the bandgap values for $ZnSnN_2$ thin films to be ~2.6 eV, much higher than the theoretical prediction value. Nevertheless, further decrease in electron density, high-quality film deposition, more effective electron-killer, and cation disorder coordination are still needed for its promising usage in photovoltaic systems and solid-state lighting in the near future.

6.2 Perspectives for Future Work

Several problems were encountered during this work. There is still space to improve the reactive radio-frequency magnetron sputtering technology although it is widely used to grow nitride-based thin films and better than the other depositions. A study of the deposition parameters was made but further optimization is still necessary. The influence of the subsequent thermal annealing under certain atmosphere may also be exploited to increase the film uniformity. If these two study objects would be used in electronic, optoelectronic and photovoltaic systems, there are still some constraints up in the air awaiting surmounted in the follow-up research and development.

6.2.1 Oxygen Impurity Removal

One of the major aspects with the production of Zinc Nitride is the presence of oxygen at film surface and within film host. This problem has been extensively studied by the literature but still no solution has been accomplished. One possible solution would be to passivate the film surface *in-situ*, that is, before the film is taken out from vacuum, using an inert cover layer on top.

6.2.2 Determination of Intrinsic Bandgaps of Zn_3N_2 and $ZnSnN_2$ Materials

The difficulty in synthesis of electronic quality samples in part hinders their progress in materials science and device applications, which makes the determination of intrinsic bandgap energy values seem to be "impossible" till date. More advanced technique and ideal experimental conditions should be developed.

6.2.3 Meliorative Durability of Zn_3N_2 and $ZnSnN_2$ Materials

Due to the chemical activity, oxygen is higher than that of nitrogen, making Zn preferentially combine with oxygen rather than with nitrogen when preparing Zn_3N_2 and $ZnSnN_2$ materials. For now, preserving zinc nitride thin film in a vacuum chamber is an impermanent treatment. In an argon atmosphere, Zn_3N_2 powder is stable up to its decomposition point at around 700 °C, which gives us an indication that preserving Zn_3N_2 with Ar may be a good way to prevent nitride oxidation/hydrolysis. Or, just like the preventive defence of oxygen contamination, another possible solution would be to passivate the film surface before the film is taken out from vacuum, using an inert cover layer atop film surface.

6.2.4 Further Decrease in Electron Density of $ZnSnN_2$ Material

Even though we have tried to take advantage of Cu(I), as electron killer, to compensate the heavily oxygen-doping effect, not so positive results we obtained. We still have hope and expectation that more effective dopants exist. On the other hand, there are at least two routs to lower the carrier density in $ZnSnN_2$: post-growth annealing or off-stoichiometry, which are a new start in other group and ongoing. Annealing is performed under an activated nitrogen atmosphere in the same vacuum chamber in which films are grown, without breaking vacuum between film-growth and anneal process. Zinc-rich-grown $ZnSnN_2$ films as an off-stoichiometrical material can exhibit lower electron density. But a trade-off between off-stoichiometry and cation-disorder degree has not been found yet.

Appendix

List of Publications

論　文　目　録

氏　名　曹 祥（Xiang CAO）　（発表した論文）

論　文　題　目	公表の方法及び時期	著　者　名
(査読論文)		
1. Zinc nitride as a potential high mobility transparent conductor	*Physica Status Solidi (a)* DOI: 10.1002/pssa.201600472	X. CAO Y. NINOMIYA N. YAMADA
2. Comparative study of electron transport mechanisms in epitaxial and polycrystalline zinc nitride films	*Journal of Applied Physics* 2016, **119**: 025104 (1-10)	X. CAO Y. YAMAGUCHI Y. NINOMIYA N. YAMADA
3. Oxygen-doped zinc nitride as a high-mobility nitride-based semiconductor	*The Journal of Physical Chemistry C* 2015, **119**: 5327–5333	X. CAO A. SATO Y. NINOMIYA N. YAMADA

論　　文　　題　　目	公表の方法及び時期	著　　者　　名
4. *p*- to *n*-type conversion and nonmetal–metal transition of lithium-inserted Cu_3N films	*Chemistry of Materials* 2015, **27**: 8076–8083	N. YAMADA K. MARUYA Y. YAMAGUCHI X. CAO Y. NINOMIYA
5. Mineralogy study of the effect of iron-bearing minerals on coal ash slagging during a high-temperature reducing atmosphere	*Energy & Fuels* 2015, **29**: 6948–6955	H. X. LI J. Y. XIONG Y. X. TANG X. CAO
6. Study on mineral factor of ternary-component blended coal on coal ash fusibility and its fusion mechanism	*Journal of China Coal Society* 2013, **38**: 314–319	X. CAO H. X. LI Q. LIU Z. L. ZHANG B. Y. ZHU Q. L. ZHAO
7. Study of effect of ternary-component blended coal on coal gasification reaction at high temperature	*Applied Mechanics and Materials* 2013, **295–298**: 3104–3109	H. X. LI X. CAO Y. X. TANG
8. Influence of sewage sludge on the slurrying properties and co-gasification kinetics of coal-sludge slurries	*Advanced Materials Research* 2013, **634–638**: 239–244	B. Y. ZHU H. X. LI J. YAO Q. LIU Z. L. ZHANG X. CAO

論　　文　　題　　目	公表の方法及び時期	著　　者　　名
(投稿中の論文)		
1. High-throughput optimization of near-infrared-transparent Mo-doped In_2O_3 thin films with high conductivity by combined use of atmospheric-pressure mist chemical-vapor deposition and sputtering	*Thin Solid Films* In Press	N. YAMADA M. YAMADA H. TOYAMA R. INO X. CAO Y. YAMAGUCHI Y. NINOMIYA
(国際会議論文)		
1. Zinc nitride as a potential high-mobility transparent conductor	*The 2016 European Materials Research Society (E-MRS) Spring Meeting* 2016, Lille, France	X. CAO Y. NINOMIYA N. YAMADA
2. Zn_3N_2 as a potential high-mobility transparent semiconductor	*The 9th International Symposium on Transparent Oxide and Related Materials for Electronics and Optics (TOEO-9)* 2015, Tsukuba, Japan	X. CAO Y. NINOMIYA A. SATO N. YAMADA
3. Oxygen-doped zinc nitride thin film: a nitride-based transparent conductor	*The 5th International Symposium on Transparent Conductive Materials (TCM2014)* 2014, Crete, Greece	X. CAO N. YAMADA K. WATARAI A. SATO Y. NINOMIYA

論　　文　　題　　目	公表の方法及び時期	著　　者　　名
(国内会議論文)		
1. Cu-doping into $ZnSnN_2$ film: structural, electrical and optical properties	*The 77th JSAP (Japan Society of Applied Physics) Autumn Meeting* 2016, Niigata, Japan	X. CAO Y. SUGIYAMA F. KAWAMURA Y. NINOMIYA T. TANIGUCHI N. YAMADA
2. Growth and characterizations of a pseudo-III-nitride $ZnSnN_2$	*The 63rd JSAP (Japan Society of Applied Physics) Spring Meeting* 2016, Tokyo, Japan	X. CAO K. UMEZOME F. KAWAMURA Y. NINOMIYA T. TANIGUCHI N. YAMADA
3. Effective mass in zinc nitride thin films	*The 76th JSAP (Japan Society of Applied Physics) Autumn Meeting* 2015, Nagoya, Japan	X. CAO A. SATO Y. NINOMIYA N. YAMADA
4. Electron transport mechanism of oxygen-doped zinc nitride thin films	*The 62nd JSAP (Japan Society of Applied Physics) Spring Meeting* 2015, Tokyo, Japan	X. CAO A. SATO Y. NINOMIYA N. YAMAD
5. Electronic conductivity of impurity-doped Zn_3N_2 thin films	*The 75th JSAP (Japan Society of Applied Physics) Autumn Meeting* 2014, Hokkaido, Japan	X. CAO K. WATARAI Y. NINOMIYA A. SATO N. YAMADA